2018

# Microstructural Characterization of LENS$^{TM}$ Ti-6Al-4V: Investigating the Effects of Process Variables Across Multiple Deposit Geometries

Laura Christine Davidson
*Wright State University*

# MICROSTRUCTURAL CHARACTERIZATION OF LENS™ DEPOSITED Ti-6Al-4V: INVESTIGATING THE EFFECTS OF PROCESS VARIABLES ACROSS MULTIPLE DEPOSIT GEOMETRIES

A thesis submitted in partial fulfillment

of the requirements for the degree of

Master of Science in Materials Science and Engineering

By

LAURA CHRISTINE DAVIDSON

B.S.M.S.E., Wright State University, 2015

2018

Wright State University

WRIGHT STATE UNIVERSITY
GRADUATE SCHOOL

November 29, 2018

I HEREBY RECOMMEND THAT THE THESIS PREPARED UNDER MY SUPERVISION BY Laura Christine Davidson ENTITLED Microstructural Characterization of LENS™ Deposited Ti-6Al-4V: Investigating the Effects of Process Variables Across Multiple Deposit Geometries BE ACCEPTED IN PARTIAL FULLFILLMENT OF THE REQUIRMENT FOR DEGREE OF Master of Science of Materials Science and Engineering

_____

Nathan Klingbeil, Ph.D.

Thesis Director

_____

Joseph C. Slater, Ph.D., P.E.

Chair, Department of Mechanical and

Materials Engineering

Committee on final examination:

_____

Nathan Klingbeil, Ph.D.

_____

Joy Gockel, Ph.D.

_____

Raghavan Srinivasan, Ph.D., P.E.

_____

Barry Milligan, Ph.D.

Interim Dean of the Graduate School

ABSTRACT

Davidson, Laura Christine. M.S.M.S.E., Department of Mechanical and Materials Engineering, Wright State University, 2018. *Microstructural Characterization of LENS™ Deposited Ti-6Al-4V: Investigating the Effects of Process Variables Across Multiple Deposit Geometries*.

Laser based additive manufacturing of Ti-6Al-4V components is under consideration for aerospace applications. The mechanical properties of the finished components depend on their microstructure. Process mapping compares process variables such as heat source power, heat source travel speed, material feed rate, part preheat temperature and feature geometry to process outcomes such as microstructure, melt pool geometry and residual stresses. In this work, the microstructure of two-dimensional pads, multilayer pads, thin walls, and structural components at the steady state location was observed. A method for measuring β grain widths that allows for the calculation of standard deviations, confidence intervals, and variances in grain size was developed. This represents an improvement over the commonly used line-intercept method. The method was used to compare variability of β grain widths across different part geometries. It was found that thin wall parts have the highest β width variability and that the width of the β grains varies more towards the top of multi-layered samples than towards the bottom. Experimental results for α and β grain size across multiple deposit geometries are presented that offer new insight into the effect of process variables on microstructure. β grain widths are also compared for different deposit geometries with the same power, velocity, and feed rate. Single layer pad geometries were found to have the smallest β grain widths, multi-layer pads had larger β grain widths, and thin wall samples had the largest β grain widths. Trends in α width with Vickers hardness were also considered in the context of thermal gradient measurements.

Hardness maps were created for the structural component samples. Optical microscopy was used to observe a layering effect in structural component samples. It was found that light and dark bands had different Vickers microhardness values.

# Table of Contents

# List of Figures

# List of Tables

# Acknowledgements

The completion of this thesis would not have been possible without help and support. I would like to thank my advisor, Dr. Nathan Klingbeil, for his guidance during my time at Wright State. I would also like to thank the other members of my committee, Dr. Raghu Srinivasan and Dr. Joy Gockel. Their input and support have helped greatly. I would also like to thank the other professors of the mechanical and materials engineering department.

I wish to express my gratitude to the organizations that funded this research. Financial support was provided by the National Science Foundation and America Makes (The National Additive Manufacturing Innovation Institute).

I would like to thank the other members of Dr. Klingbeil and Dr. Gockel's research groups who have helped me along the way: Greg Loughnane, Luke Sheridan, Sarah Kuntz, Megann Robinaugh, Sonya Sokhey, and Nathan Levkulich.

Collaborators in other organizations also provided invaluable insight and assistance. Ted Reutzel of Penn State ARL helped organize experiments that were vital for the data collected in this thesis. Zachary Francis of Carnegie Mellon University assisted with the single layer pad analysis. The staff of the welding engineering program at Ohio State generously offered the use of their hardness testing equipment. John Sosa provided assistance with his MIPAR™ software at CEMAS.

I would like to thank the Air Force Research Lab for the use of their facilities for characterizing my samples. Mike Velez, Bob Lewis and Brian Turner taught me the best way to prepare and polish my samples. Jared Shank taught me how to use an electron microscope and Kathleen Cissel taught me about different spectroscopy methods and helped with the collection of EBSD data. Dr. Jaimie Tiley offered his insight and knowledge both as my professor for

nonferrous metallurgy and on base. I also want to thank Dr. John Porter for his support and for all the times he discussed my research with me.

I am grateful to my siblings, Kevin and Kim for encouraging me. They have always pushed me to be my best. Finally, I would like to thank my husband, James, for his love and support through this process.

# 1 Introduction and Literature Review

## 1.1 Motivation

Additive manufacturing is used for many applications that require parts with complex geometries. For those parts to have consistent mechanical properties, it is necessary to be able to predict and control their solid-state microstructures. Solid-state microstructure depends on the thermal conditions at the time of manufacturing.

This thesis examines the microstructures in single layer pads, multi-layer pads, and thin wall specimens of Ti-6Al-4V manufactured via the LENS$^{TM}$ process. β grain widths and how they vary with height from the substrate were observed. Vickers microhardness measurements were collected and correlated to α-lath thicknesses. Vickers hardness is known to be correlated to other mechanical properties such as tensile strength [1]. Through these investigations, this work aims to contribute new potential target outcomes for use in solidification microstructure process mapping approaches.

## 1.2 Additive Manufacturing in general

Additive manufacturing is any manufacturing process where parts are built up from materials rather than being chipped down. For comparison, the latter process could be called “subtractive manufacturing” and includes processes such as machining, or an artist making a sculpture from a block of stone. The simplest additive manufacturing method then would be building with blocks. When used in an engineering context however, most people take additive manufacturing to mean something similar to three-dimensional printing, where a machine builds a part layer by layer using a computer model. Additive manufacturing is forecast to continue growing very rapidly [2].

Additive manufacturing has several important advantages over traditional manufacturing methods. First of all, additive manufacturing can be used to create parts with complex geometries that could not be created using traditional methods [3]. The ability to design parts with complex geometries can also allow for designs that reduce the weight of a part. An example of that principle is that General Electric held a design competition to reduce the weight of an aircraft engine bracket by changing the geometry. GE encouraged participants to look at additive manufacturing to make the part. Some of the designs were able to reduce the weight by up to 80% [4].

Not only can additive manufactured parts take advantage of designs that use less material than conventional methods- additive manufactured parts generate less waste material than conventionally manufactured parts [5]. Some transportation related additively manufactured parts also have a reduced life-cycle energy usage compared to similar conventionally manufactured parts [6].

There are multiple different types of additive manufacturing processes, as well as different material systems. Metals, polymers and even ceramics can be used to additively manufacture parts. Metal additive manufacturing processes can be classified in many ways. This review will outline four different types. Some additive manufacturing processes melt material using a laser beam and others use an electron beam. Some processes add material as the beam travels along and others use a powder bed. Figure 1.1 summarizes the methods discussed in this section.

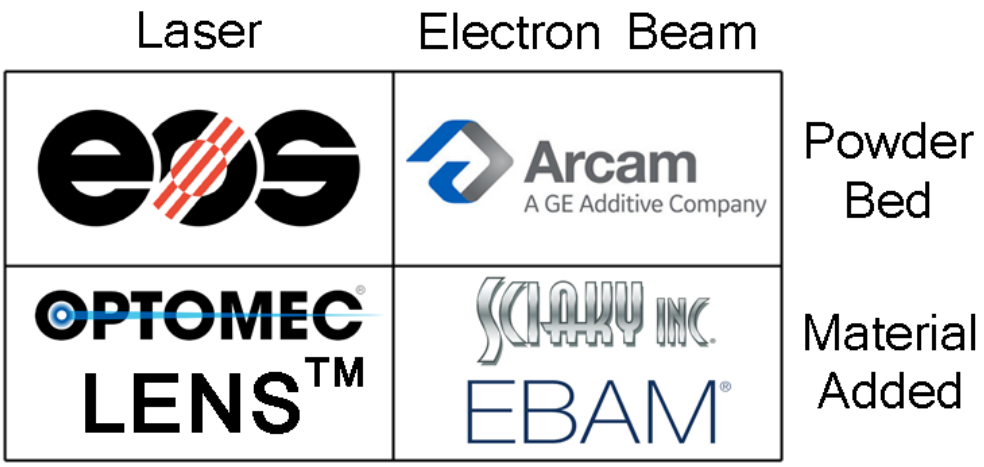


**Figure 1.1: The additive manufacturing methods discussed [7, 8, 9, 10]**

The Sciaky Electron Beam Additive Manufacturing (EBAM®) process is an example of a wire feed electron beam process. An electron beam is used to melt wire feedstock and build parts layer by layer [11].

An example of a powder bed electron beam process is Arcam. In powder bed additive manufacturing, powder is spread before sintering each layer. Then an energy source such as an electron beam or laser travels across the area to be melted. More powder is spread, and the process is repeated layer by layer until the part is complete [12]. The Arcam electron beam melting process occurs at an elevated temperature in a vacuum. Pre-heating parts can help to prevent residual stresses and the formation of martensitic microstructures. Once the melting process has begun, the inert gas, helium is added to prevent oxidation [13]. Machines made by EOS also use a power bed, however they utilize a laser as the energy source rather than an electron beam [8].

An example of a powder stream laser beam process is the Laser Engineered Net Shaping (LENS$^{TM}$) process. It was developed in 1996 by Sandia National Laboratories [14]. It sprays powder that is melted by a laser. $CO_2$ lasers, Nd:YAG lasers, and Yb fiber lasers have all been

used in LENS™ machines [15]. Figure 1.2 shows a schematic of the LENS™ process. Figure 1.3 shows the powder nozzles and laser for the LENS™ process.

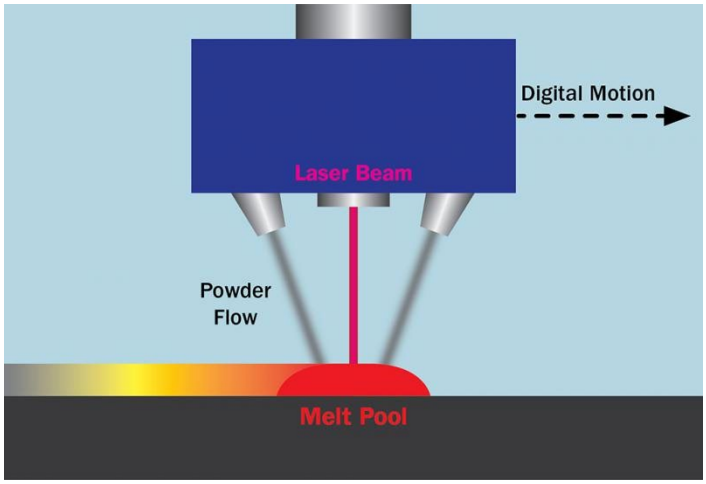


Figure 1.2: A schematic of the LENS™ process [16]

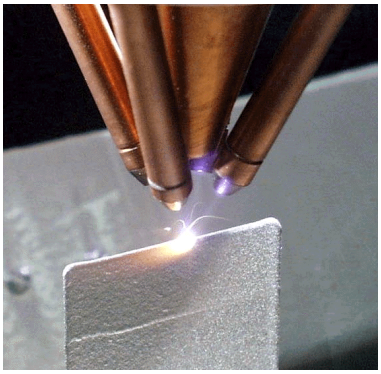

Figure 1.3: The LENS™ process performing a single-line build [17]

The LENS™ process is conducted in an inert-gas chamber, typically argon, to ensure that titanium does not oxidize during the build [18].

## 1.3 Process mapping

Process mapping is the mapping of process outcomes such as microstructure, melt pool geometry and residual stress in terms of process variables, such as heat source power, heat source travel speed, material feed rate, part preheat temperature and feature geometry [19].

In 1999, Vasinonta, et al developed process maps from numerical models of laser-based material deposition of thin-walled structures. The effects of changes in laser power, deposition speed, and part preheating on process parameters were mapped [20].

In 2000, Vasinonta, et al used simulations to develop process maps that quantified the effects of changes in wall height, laser power, deposition speed and part preheating on melt pool size (for consistent build conditions) and thermal gradients (for limiting residual stresses) [21]. The geometry was thin-walled structures. Models were applied to the LENS$^{TM}$ process.

In 2002, Klingbeil, et al compared 2-D continuum finite element model and 3-D cellular automaton model predictions to observed microstructures in thin wall LENS$^{TM}$ deposited Ti-6Al-4V [22]. The laser deposition process was modeled as a moving point heat source. The 2-D models suggested that increasing laser power for a constant velocity would also increase grain size, but the 3-D model predictions and samples themselves did not confirm that suggestion.

In 2003, Kobryn and Semiatin published a map of thermal gradient vs. solidification rate for LENS$^{TM}$ deposited Ti-6Al-4V that included qualitative descriptions of microstructures [23]. That same year, Bontha and Klingbeil considered thin-wall (2-D) and bulky (3-D) geometries of LENS$^{TM}$ deposited Ti-6Al-4V. They numerically extracted cooling rates and thermal gradients from the Rosenthal solution for a moving point heat source traversing an infinite substrate. Dimensionless process maps were presented and results for both small-scale (LENS$^{TM}$) and large scale (higher power) processes were plotted on solidification maps for predicting grain morphology in Ti-6Al-4V [24].

In 2004, Klingbeil, et al discussed analytical approaches based off Rosenthal solution and numerical modeling approaches to look at process variables and size scale on solidification microstructure in LENS$^{TM}$ deposited Ti-6Al-4V [25].

In 2006, Bontha developed thermal process maps for dimensionless thermal gradient and solidification rate for two-dimensional thin wall and bulky three-dimensional structures made from Ti-6Al-4V using the LENS$^{TM}$ process [26]. That same year, Bontha, et al plotted dimensionless process maps for predicting solidification microstructure in thin-walled LENS$^{TM}$ Ti-6Al-4V samples. Cooling rates and thermal gradients at the onset of solidification were extracted using the two-dimensional Rosenthal solution. Their results indicated that changes in laser power and velocity can have a substantial effect on solidification cooling rate and thermal gradient [27].

In 2009, Bontha, et al looked at solidification microstructure in beam-based fabrication of bulky 3-D structures. The paper suggests "that changes in process variables (beam power and velocity) can result in a grading of the microstructure throughout the depth of the deposit, with a transition from columnar to mixed or equiaxed microstructure at higher powers." [28]

That same year, Davis, et al examined the effect of free-edges on melt pool geometry and solidification microstructure for 2-D thin wall geometries. They used the 2-D Rosenthal solution for a moving point heat source to numerically extract cooling rates and thermal gradients at the onset of solidification throughout the depth of the melt pool. They plotted solidification maps for predicting trends in grain size and morphology for Ti-6Al-4V. The geometry that was observed was thin-wall structures [29]. In 2010, the authors extended that same work to bulky 3-D geometries [30].

Davis modified the Rosenthal solution to include the effects of free edges. MATLAB was used to determine dimensionless results for melt pool geometry, solidification cooling rate and thermal gradient. Those results were plotted as a function of distance from the free-edge [31].

In 2013, Doak investigated the effects of process variables on solid-state phase transformations below the solidification temperature through Finite Element Modeling, the 3-D Rosenthal Solution and experimental results. The results suggested that constant melt pool area leads to constant solid-state α-lath morphology [18].

Gockel and Beuth predicted solidification microstructure using a solidification map for Ti-6Al-4V and the cooling rates and thermal gradients from finite element material added models. They focused on single bead deposits made using an electron beam wire feed additive manufacturing process [32].

Beuth, et al published an overview of their work capturing the dependence of melt pool geometry and microstructure on primary processing variables under steady-state and transient conditions. They included a chart showing the regions of P-V space occupied by commercial direct metal additive manufacturing processes, as shown in Figure 1.4 [19].

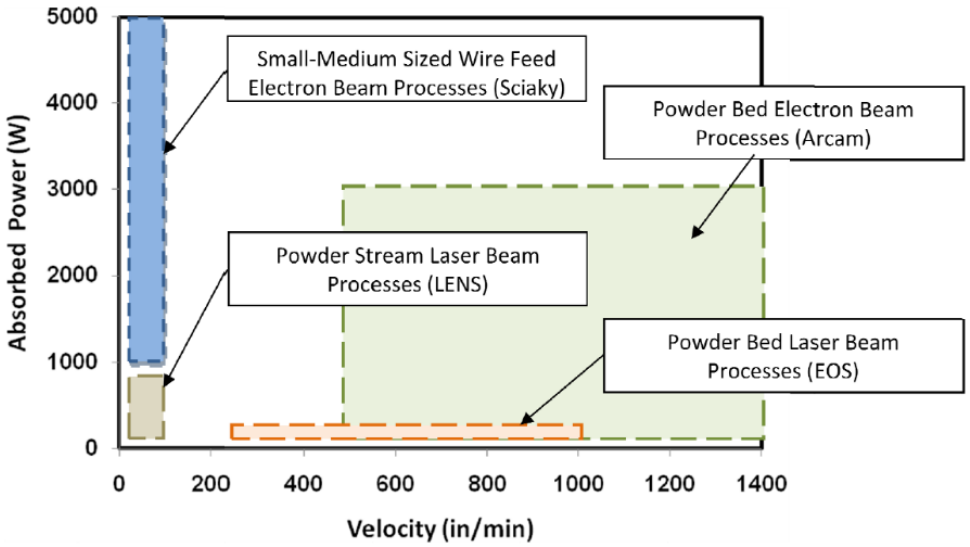


**Figure 1.4: A process map showing the regions of P-V space occupied by direct metal additive manufacturing processes [19]**

In 2014, Gockel developed solidification microstructure process maps for single bead and thin wall deposits of Ti-6Al-4V via an electron beam wire feed and electron beam powder bed

additive manufacturing process. It was shown that indirect microstructure (prior β grain size and morphology) control is possible through direct melt pool dimension control in single bead deposits of Ti-6Al-4V [33].

In 2015, Montgomery, Beuth, Sheridan, and Klingbeil compared models to experimental results for Inconel 625 made using laser powder bed additive manufacturing. Single and multi-layer pad geometries manufactured using different combinations of power and velocity were examined. Finite element modeling was used to simulate the thermal effects of added powder. A process map was constructed with curves of constant melt pool width and cross-sectional area plotted against power and velocity [34].

In 2016, Kuntz utilized a process mapping approach to look at four different additive manufacturing processes for Ti-6Al-4V. The Optomec LENS$^{TM}$, Sciaky, EOS and Arcam processes were evaluated. An analytical model was introduced that focused on the bottom of the melt pool [35].

That same year, Sheridan constructed process maps for Ti-6Al-4V, Inconel 718 and Inconel 625. Both geometric and microstructural process maps were constructed. A geometric process map compares melt pool geometry to process variables such as beam power and velocity. A microstructural process map compares part microstructure to process variables such as power and velocity. A correction factor for the Rosenthal solution was introduced, reducing the error between it and non-linear simulation results. This reduces computation time for creating process maps [36].

In 2017, Francis created microstructural process maps for Ti-6Al-4V parts manufactured using electron beam wire feed and laser powder feed processes. Spot size was considered as a

process variable. Models were developed and tested through experiments across processes and alloys [37].

## 1.4 Ti-6Al-4V Material System

In certain titanium alloys, as the alloy cools, a stable hexagonal closed packed phase and a stable body centered cubic phase form [38, 39, 40]. The hexagonal close packed phase is known as the α phase and the body centered cubic phase is known as the β phase [38]. Figure 1.5 shows unit cells for α and β titanium.

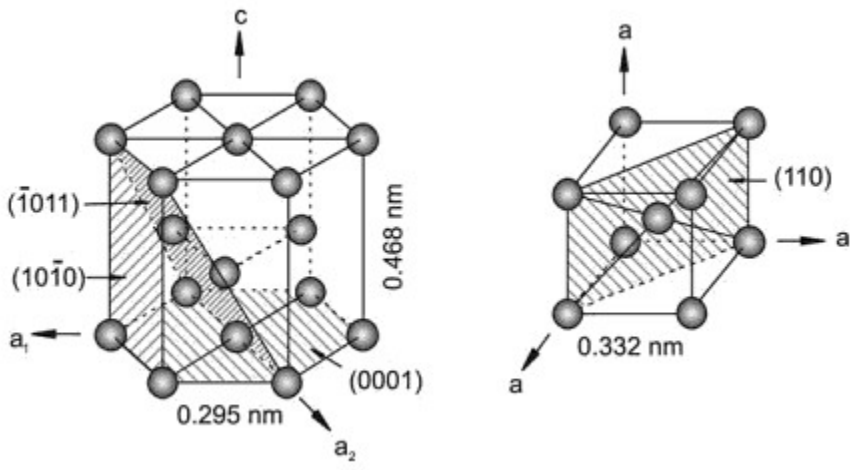


**Figure 1.5: Unit cells for α and β titanium [41]. α titanium has a hexagonal close packed (HCP) crystal structure and β titanium has a body centered cubic (BCC) crystal structure.**

A Widmanstätten microstructure, also known as a "basketweave" structure occurs when parallel plates of these phases "have formed with a crystallographic relationship to the phase from which they formed" [42, 43]. Figure 1.6*a* shows titanium that solidified with a Widmanstätten microstructure. Figure 1.6*b* shows titanium that has what is known as a "colony α" microstructure.

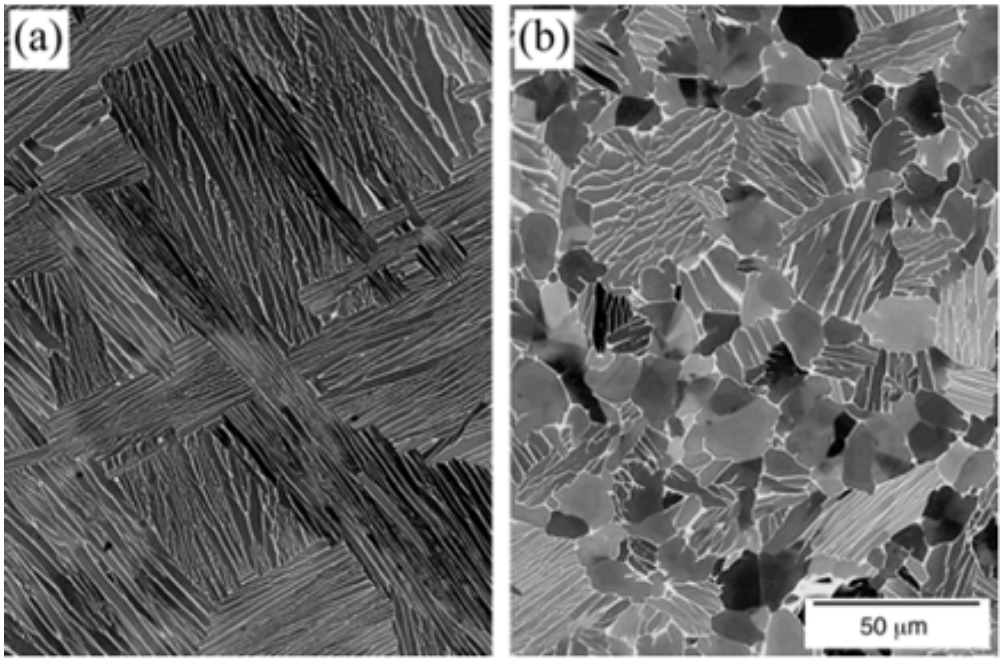


**Figure 1.6: (a) shows titanium with a Widmanstätten microstructure and (b) shows titanium with a "colony α" microstructure [44]**

The focus of this research is titanium alloy Ti-6Al-4V. This alloy is 90% titanium, 6% aluminum, and 4% vanadium by weight [38]. By weight, this alloy is the most commonly used titanium alloy in the world [38, 42, 45].

In pure titanium, when the alloy is above what is called the "β transus" temperature, the microstructure consists entirely of large β grains [42]. As pure titanium cools below that point, all of the material undergoes solid-state phase transformations and becomes the hexagonal close packed phase known as α [42, 43]. Adding alloying elements allows for more control over titanium microstructure.

In titanium, there are two main types of alloying elements: α stabilizers and β stabilizers [38]. In Ti-6Al-4V, aluminum serves as an α stabilizer and vanadium serves as a β stabilizer. Figure 1.7 shows α plus β titanium (Ti-6Al-4V). The red lines are where the large β grain boundaries were at temperatures above the β transus. Even after titanium cools and undergoes the solid-state phase transformations, the prior β grain boundaries remain and can be seen if a sample is etched.

Figure 1.7: Ti-6Al-4V microstructure at 100x magnification. The red lines indicate prior β grain boundaries.

As-manufactured β grain morphologies in Ti-6Al-4V are important because Widmanstätten microstructures cannot be converted to equiaxed microstructures by heat treatment alone [38]. After one transformation from β to α plus β, the basic crystallographic texture cannot be changed by heat treatment.

## 1.5 Existing techniques for characterizing Ti-6Al-4V microstructures

In 2004, Tiley, et al used Fovea Pro 3.0 to characterize Ti-6Al-V [46]. Fovea is a set of plug-ins for use within Adobe's Photoshop software that is available commercially. They developed stereological procedures for quantifying the thickness of Widmanstätten α-laths, colony scale factor, prior β grain size and volume fraction of Widmanstätten α-laths.

Later that year, Searles, et al used Fovea Pro 3.0 to characterize Ti-6Al-4V [47]. They looked at microstructural characteristics that are most likely to influence mechanical properties. They developed procedures to quantify mean equiaxed α size, volume fraction of equiaxed α, volume fraction of total α and the thickness of Widmanstätten α-laths in transformed β.

In 2009, Collins et al use Fovea to characterize Widmanstätten microstructures in titanium [44]. That work continued to look at the microstructural characteristics most likely to influence mechanical properties.

In 2014, Sosa, et al developed MIPAR$^{TM}$, or Materials Image Processing and Automated Reconstruction [48]. MIPAR$^{TM}$ is MATLAB based. The software allows a user to develop a procedure for stereological analysis, then save the steps as a "recipe" to apply to a series of micrographs.

In 2015, Loughnane, et al performed microstructural characterization of LENS$^{TM}$ manufactured Ti-6Al-4V α-laths using MIPAR$^{TM}$ [49]. Mean α-lath thickness was quantified at several heights for tall thin walled components. Discrete probability distributions were compared using a modified version of the Bhattacharyya coefficient. α-lath thicknesses were then compared to thermal data that had been gathered when the samples were manufactured.

That same year, Leicht and Wennberg used Digital Image Correlation analysis to compare strain fields in tensile tested samples. The samples observed were made from selective laser melted (SLM) Ti-6Al-4V and EBM Ti-6Al-4V. Digital image correlation involves taking multiple images. The first is used as a reference, and subsequent images are measured to determine the displacement of features. This allows for the collection of finer details about strains than can be acquired by the use of an extensometer alone [50].

## 1.6 Microstructure and Mechanical Properties

Mechanical properties are an indication of how materials will perform when a load is applied [1]. This is in contrast to physical properties, which are inherent qualities of the material and do not depend on having a load applied. Examples of physical properties include density and color.

This thesis will not discuss all mechanical properties of materials but will offer a short overview. Mechanical properties include tensile strength, ductility, hardness, stiffness, yield strength and Young's modulus; however, that list is far from exhaustive.

In order to find the tensile strength of a material, a sample is gripped in a machine and pulled apart [51]. Figure 1.8 shows a sample of Al-6061 that underwent tensile testing.

**Figure 1.8: a sample of Al-6061 that underwent tensile testing.**

The tensile strength is the maximum load applied to the sample divided by its original cross-sectional area [52]. In metals, the maximum load is typically applied to the sample when necking initiates [39]. Finding the compressive strength of a material is similar; the material is compressed until it breaks and the maximum load is divided by the original cross-sectional area [1].

Multiple factors affect the tensile strength of metals. Alloys have higher tensile strengths than their pure metal counterparts [39]. Strain hardening increases the strength of a part by introducing dislocations which impede the movement of other dislocations [53]. Decreasing the grain size increases tensile strength. In Ti-6Al-4V, not only is the thickness of α lamellae a factor in determining strength, but also the diameter of the α colonies [54].

Solid solution strengthening increases the strength of metals by introducing atoms of different elements in order to create lattice distortions which impede dislocation motion. In titanium specifically, hydrogen, nitrogen, and oxygen have a very high solubility [42].

It is important to note that in titanium alloys, the addition of interstitial elements such as hydrogen, oxygen and nitrogen can greatly increase strength but it also decreases ductility and makes components quite brittle [38]. Ductility is a mechanical property that describes how much plastic deformation a material can undergo before it breaks [1]. Even adding too much aluminum to a titanium alloy can make it too brittle; the practical upper limit is around 7% [38].

Adding precipitates to a metal makes it stronger [53]. Precipitates are formed when so much solute is added to a metal that it forms a secondary phase. For example, in titanium, carbon has a low solubility but can dramatically increase strength. When carbon is added beyond the solubility limit, it forms a titanium carbide precipitate, TiC [42].

For additively manufactured Ti-6Al-4V, the orientation of the build can affect the ultimate tensile strength and the ductility. Epitaxial growth of columnar β grains can create an anisotropic crystallographic texture in additively manufactured parts. In 2014, Simonelli, et al found that tensile testing SLM Ti-6Al-4V samples led to fracture along the grain boundaries [55].

The type of additive process also matters. Interlayer porosity can occur when building parts using powder bed processes, leading to differences in yield strength and ultimate tensile strength across build orientations.

In 2015, Leicht and Wennberg found that Ti-6Al-4V manufactured using both SLM and EBM methods showed differences in tensile strength with respect to the build orientation [50]. Samples that were built perpendicular to the direction of the tensile test were found to have higher tensile strengths.

Powder stream processes can also show differences depending on build orientation. In 2001, Kobryn and Semiatin performed tensile tests for LENS$^{TM}$ deposited Ti-6Al-4V and found that

yield strengths were lowest for samples tested in a longitudinal orientation with respect to the build layers [56].

Carroll, et al performed uniaxial tensile testing on LENS$^{TM}$ deposited Ti-6Al-4V and found that tensile strengths were similar for both longitudinal and transverse orientations of the build layers. However, elongations were found to be different. For samples tested in a longitudinal orientation with respect to the build layers, elongation was 11% and for samples tested in a transverse orientation with respect to the build layers, elongation was 14%. A lack of porosity in the components could contribute to the observed mechanical properties [57].

In addition to determining tensile strength, a tensile test can allow for the determination of a sample's yield strength, toughness, Poisson's ratio, and modulus of elasticity, also known as the Young's modulus [53, 51]. The ability to determine multiple mechanical properties from a single test makes tensile tests very useful. The disadvantages are that the sample must be machined to the proper specifications for the tensile testing equipment to be used, and tensile testing destroys the sample.

A material's yield strength is its "maximum resistance to elastic deformation" [52]. The yield strength of a material typically increases as the material's grain size decreases [58]. Specifically, the relationship between yield strength and grain size can be approximated using the Hall-Petch equation:

$$\boldsymbol{\sigma_y = \sigma_0 + k_y d^{-\frac{1}{2}}}; \quad (1)$$

where $\sigma_y$ is the yield strength, $d$ is the average grain diameter, and $\sigma_0$ and $k_y$ are constants that depend on the material in question [1]. In 2017, Zhang, et al tested the mechanical properties of commercially pure (CP) titanium and extra-low interstitial (ELI) Ti-6Al-4V that underwent a multidirectional isothermal forging (MDF) process. Figure 1.9 shows their experimental data

illustrating the Hall-Petch relationship. Note that the x-axis of the plot is the grain diameter to the -1/2 power.

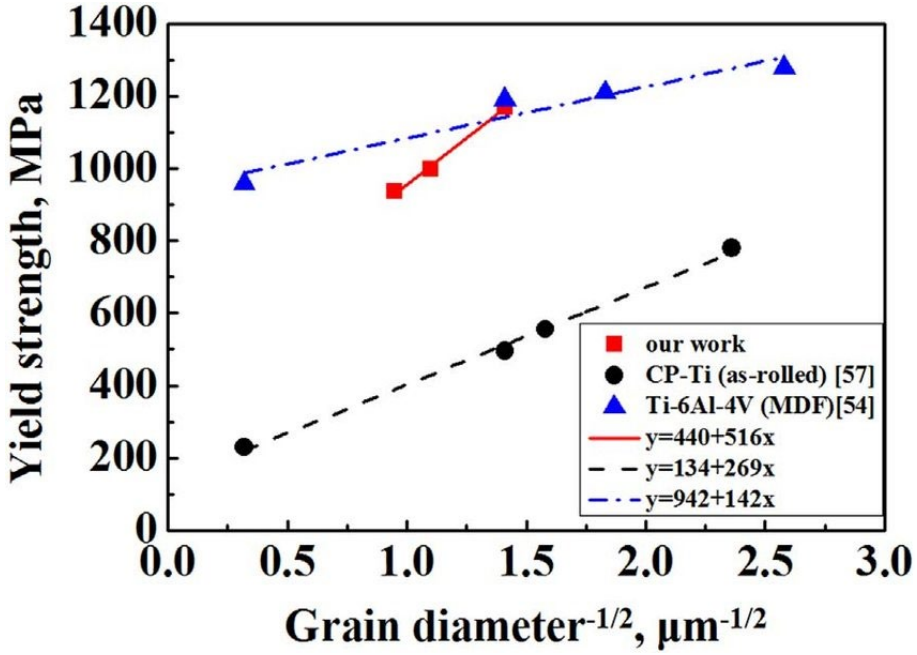


Figure 1.9: A plot illustrating the Hall-Petch relationship for pure titanium and Ti-6Al-4V [59]

Smaller grains increase the yield strength by two mechanisms. Dislocations have to change direction as they pass through grains with different orientations, and more grains per unit volume means that the dislocations have to change direction more as they pass through the sample [1]. Grain boundaries have disorder on an atomic level. That means that slip planes cannot be continuous from grain to grain. Slip planes can be defined as "the crystallographic plane along which [a] dislocation line traverses" [1]. In other words, anything that impedes dislocation motion will make a part stronger. It is important, however, to view the extrapolation of the Hall-Petch equation to extremely small grain sizes with caution. The equation can predict yield strength levels that are unrealistic for real world materials [53].

Grain morphology can also affect yield strength in titanium alloys. Samples that have equiaxed, or globular grains have higher yield strengths than samples with acicular, or needlelike grains [38].

In 2017, Hayes, et al investigated the yield strength of additively manufactured Ti-6Al-4V. The Sciaky EBAM process was used to create samples and three different heat treat conditions were used. Tensile coupons were created at 6 different orientations and tested. Equations were developed to predict the yield strength of additively manufactured Ti-6Al-4V [60].

Not all mechanical properties are dependent on a material's microstructure. If two materials are tested that have different microstructures but the same chemical composition, then the Young's modulus should be the same [39]. Young's modulus is "the ratio of stress to strain within the elastic region" [61]. In titanium, heat treatment does not drastically change modulus of elasticity either [38]. The orientation of prior β grains for SLM Ti-6Al-4V specifically has also been shown to have little effect on modulus of elasticity [55].

Modulus of elasticity is dependent on the bond strength of the atoms making up the material rather than grain size and morphology [39]. It is a measure of the stiffness of a material [62]. A material's stiffness is its "resistance to elastic deformation" [1]. Stiffness is sometimes also called "rigidity" [52].

Hardness is the ability of a material to resist plastic deformation by an indenter [1, 61, 63]. Hardness tests are not as destructive as other tests for mechanical properties, such as tensile testing. It is also possible to estimate other mechanical properties such as tensile strength based on the hardness of the material. The specific relationship depends on the material being tested [1].

There are different types of hardness tests; the geometry of the indenter varies depending on the test used, and the method for determining the material's resistance to indentation vary. Rockwell hardness tests use a diamond cone shaped indenter and the hardness of the material is determined by the depth of the indentation [64]. The Vickers, Knoop and Brinell tests determine the hardness of the material by the size of the indent. The Vickers and Knoop tests use diamond pyramid shaped indenters and the Brinell test uses a spherical indenter.

The choice of hardness test depends on factors such as how hard the material is estimated to be, how thick the sample is, the size and shape of the sample, how flat the sample is, and its surface condition [65]. If the material being tested is very hard, it is possible for the hardness indenter to deform rather than the material being tested. Problems can also arise when testing a material that is not hard enough for a given hardness test. For example, the Rockwell hardness test should not be considered accurate if a hardness lower than 20 is calculated. This is because ball indenters can penetrate the sample so deeply that the indenter cap contacts the sample [66]. Diamond indentation tests become less sensitive "as the diamond indenter penetrates further down the conical portion of the diamond."

For tests that use a diamond shaped indenter, the thickness of the material being tested should be at least ten times the depth of the indentation. For tests that use a ball shaped indenter the material should be at least fifteen times as thick as the indentation [65].

It is also important to not make indentations too close to the edge of the sample. A distance of three indentation diameters should be left between the edge of the specimen and an indentation, otherwise the measurement will not be accurate [1]. If two indentations are too close together, then the results will not be accurate. At least 3 indentation diameters should be left between indentations.

For samples that do not have a flat surface, a correction factor must be applied. A hardness testing machine will register a lower hardness than the true value for a convex surface and a higher hardness than the true value for a concave surface [65].

Hardness tests can be conducted on different size scales. The terms macrohardness, microhardness and nanohardness do not refer to how hard a material is, but rather the size of the indenter being used to perform the test [67]. Larger indenters, such as the ones used for macrohardness testing, do not require a finely polished material surface [64]. Macrohardness is useful for large parts; sometimes so large that the hardness tester needs to be brought to the sample rather than the other way around [68]. It is also useful for determining the bulk hardness of parts that do not have a homogeneous microstructure.

Microhardness testing requires that a sample be polished to the same level that would be required for microstructural observation under an optical microscope. Microhardness testing can be used to observe differences in hardness across a sample [69].

Nanohardness testing makes indentations so small that they cannot be easily measured using optical microscopy techniques [70]. Nanohardness testing is very sensitive to vibration and differences in temperature. Even just handling a sample can require waiting for the sample and the indenter to reach thermal equilibrium before testing.

This work utilized the Vickers microhardness test. Figure 1.10 shows the indenter for the Vickers hardness test.

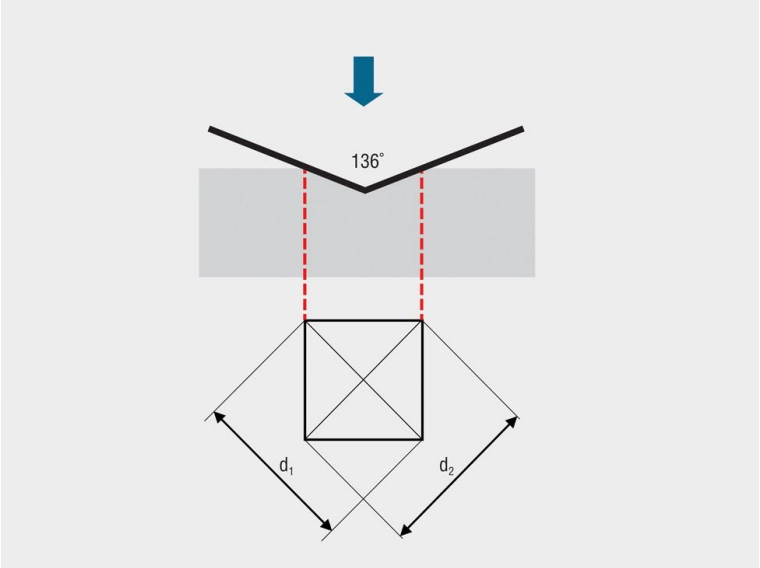


Figure 1.10: The indenter and an indent for Vickers microhardness testing [64]

In order to get a hardness value from the indent, the following formula is used:

$$HV = \frac{2000Psin\left(\frac{\alpha}{2}\right)}{d^2} = \frac{1854.4P}{d^2} \quad (2)$$

$HV$ is the Vickers hardness, $P$ is the applied load in gf, $d$ is the mean diagonal length of the indent in µm and α is the face angle (136°) [67]. A gf is a "gram-force". It is calculated by multiplying one gram times the standard acceleration due to gravity [71]. 1 gf is equal to approximately 0.0098 N. It is not the preferred SI unit- Newtons are. However, it is the unit that was displayed on the hardness testers at both the Air Force Research Laboratory and The Ohio State University. It was also the unit reported in the literature.

The Vickers Microhardness test can utilize loads between 1 and 1000 gf, but loads between 100 and 500 gf are most common [63] [67]. In general, for metals, microstructure and Vickers microhardness are correlated. Smaller grain sizes lead to higher hardness values [72].

## 1.7 LENS™ Additive Manufacturing with Ti-6Al-4V

This section briefly highlights research involving Ti-6Al-4V manufactured using the LENS™ process that has not already been discussed in previous sections. For more information about process mapping involving LENS™ manufactured Ti-6Al-4V, see section 1.3.

In 2001, Kobryn and Semiatin compared laser forming methods for Ti-6Al-4V powder. Two systems that utilize a low power Nd-YAG laser, including the Optomec LENS™ system, were compared to a system that utilized a high-power $CO_2$ laser. Optical microscopy was used to compare the microstructures of finished parts. All of the finished parts exhibited columnar grains, with the highest power laser producing grains with the largest average width [73].

In 2003, Kobryn published a map of thermal gradient vs. solidification rate for LENS™ titanium that included qualitative descriptions of microstructures against thermal gradient and solidification rate [23]. Figure 1.11 shows the solidification map.

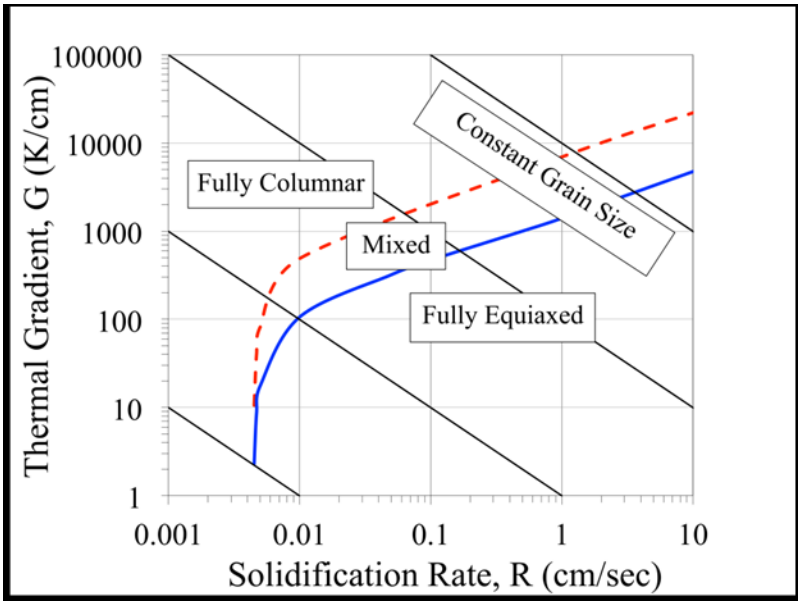


**Figure 1.11: a microstructural solidification map for LENS™ manufactured Ti-6Al-4V [23]**

In 2007, Mudge and Wald discussed the usage of LENS™ for repairing aircraft, gas turbine and drive shaft parts. A Ti-6Al-4V component for a gas turbine engine was repaired for half the

cost of buying a new part. Using LENS$^{TM}$ to repair the part also saved time compared to acquiring a new part [74].

In 2013, Das, et al discussed the use of LENS$^{TM}$ manufactured Ti-6Al-4V for biomedical implants. Porous structures are desired for hip implants. It was found that increasing powder feed rate or decreasing laser power increased porosity of finished parts. Increasing hatch distance was also found to increase porosity [75].

In that same year, Zhai and Lados conducted microstructural characterization and tensile testing of LENS$^{TM}$ deposited Ti-6Al-4V samples. Microstructures were characterized using optical microscopy and Elements-D software. LENS$^{TM}$ deposited Ti-6Al-4V was found to have higher strength and lower ductility than the mill-annealed Ti-6Al-4V substrate [76].

In 2015, Sterling, et al investigated the fatigue behavior of LENS$^{TM}$ Ti-6Al-4V. Wrought Ti-6Al-4V samples were compared to the additively manufactured samples. The fracture surfaces of the samples were observed using scanning electron microscopy. The wrought Ti-6Al-4V samples were found to have longer fatigue lives than the additively manufactured samples due to porosity and sample microstructure [77].

In 2018, Harun, et al reviewed different additive manufacturing processes that use Ti-6Al-4V. Selective Laser Sintering Direct Metal Laser Sintering, SLM, EBM and LENS$^{TM}$ were compared for biomedical applications. Microstructures across manufacturing processes were also compared [78].

## 1.8 Approach

In this work, the microstructure of LENS$^{TM}$ additively manufactured Ti-6Al-4V samples is observed. Sample preparation is discussed. Optical microscopy is used to observe β grain morphologies in single layer pad geometries, thin wall geometries and multi-layer pad

geometries. Mean β grain widths, standard deviations, and 95% confidence intervals are calculated and compared to powers and velocities. Structural component geometries are observed using electron microscopy. α-lath widths are quantified using Adobe Photoshop CS5 and the Fovea plug-in suite. Vickers microhardness values are mapped using Igor Pro software. The α-lath widths and Vickers microhardness data are compared to thermal data taken when the samples were manufactured.

## 1.9 Overview and Contributions

This thesis is organized into four total chapters. The first chapter contains the background information necessary to understand this work. Chapter 2 discusses the metallographic procedure used to prepare the samples for imaging. It also discusses the approach for α-lath and β grain analysis. Optical microscopy is used to observe β grain morphologies. Adobe Photoshop Elements is used to stitch micrographs together and trace β grains. Image J is used to measure β grains. Mean β grain widths, standard deviations and 95% confidence intervals are calculated and compared to powers and velocities.

Scanning electron microscopy is used to image α-laths. α-lath widths are calculated using Adobe Photoshop and the Fovea plug-in suite. Vickers microhardness measurements are mapped using Igor Pro. The α-lath widths and Vickers microhardness measurements are then compared to thermal data obtained when the samples were manufactured. Chapter 3 discusses the experimental results. Chapter 4 offers a summary and conclusions from this work. Suggestions for future work are offered as well.

The contributions of this thesis are as follows:

1. This thesis outlines a method for measuring β grain widths that allows for the calculation of standard deviations, confidence intervals, and variances in grain size. This represents an improvement over the commonly used line-intercept method.

2. This thesis offers new insight into the effect of deposit geometry on the variability of β grain size in additive manufacturing. β grain widths are also compared for different deposit geometries with the same power, velocity, and feed rate.

3. Experimental results for α and β grain size across multiple deposit geometries are presented that offer new insight into the effect of process variables on microstructure. Trends in α width with Vickers hardness were also considered in the context of thermal gradient measurements.

4. This thesis offers new insight into the layering effect in additive manufacturing and its relation to hardness.

# 2 Approach and Methods

This section discusses the procedure used to prepare the samples for imaging and analysis.

## 2.1 Metallographic Procedure

The first step in preparing the samples was to cut them out of the plate on which they were fabricated. Figure 2.1 shows an example of a plate with samples on it. The samples are Ti-6Al-4V and were produced in an Optomec LENS$^{TM}$ MR-7 system. Figure 2.2 shows an Optomec LENS$^{TM}$ MR-7 system.

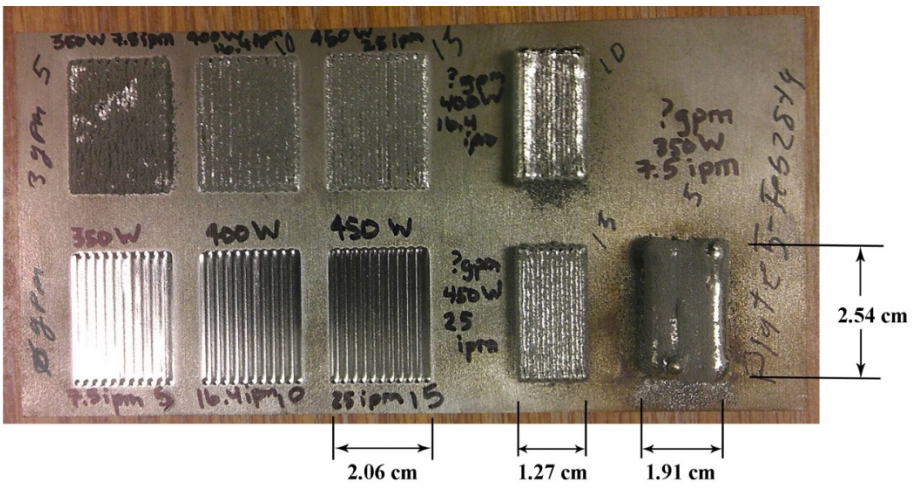


Figure 2.1: An example of a plate with samples on it

Figure 2.2: An Optomec LENS$^{TM}$ MR-7 system [79]

There are two methods available to cut the samples from the plate. The first is to use EDM, which stands for Electrical Discharge Machining [80]. This method makes very precise cuts, but it is expensive, and it takes time waiting for availability of the equipment and a technician to assist with it. Samples that are cut using EDM experience less deformation from the cutting and are faster and easier to grind and polish. Samples that undergo EDM also do not have any sharp burrs that need to be filed off.

The other method is to use a large oscillating abrasive saw. This method is faster and cheaper, but it deforms the samples as it cuts them. The saw also strain hardens the samples, making the grinding and polishing process take longer. The samples that were observed in this work were cut from their plates using an oscillating abrasive saw. After the samples were cut, any sharp spurs were ground off with sandpaper or a file.

The samples were then hot mounted in Polyfast mounting media [81]. Polyfast was used because it is a conductive media, so the samples could be observed using an electron microscope.

The mount size used was 3.18 cm because that size mount can hold a slightly larger sample, but also fits well into the autopolisher. Using a 2.54 cm mount size would require taking more time to cut smaller pieces of sample from the starting plates. Using a 3.81 cm mount size would mean that fewer samples can fit into the autopolisher. A vibrating Dremel tool was used to label the mounted samples after they came out of the press.

For hand polishing samples, some metallographers will bevel the top side of a sample using a sander so that the sample can be held more comfortably. For autopolishing samples, it is recommended that a 2-4 mm bevel be applied to the underside (the side with the metal) of the sample to avoid damaging the polishing cloths [82].

The autopolisher used was a Buehler EcoMet 250 with a Buehler AutMet 250 attachment. Figure 2.3 shows the autopolisher setup.


Figure 2.3: The autopolisher setup that was used [83].

It is important to note that an autopolisher wheel must contain a minimum of at least 3 samples in order to keep the weight balanced. The maximum number of samples is 10. If an autopolisher must be used, but a metallographer has fewer than 3 samples, he or she can always mount a piece of scrap metal from the substrate and put it into the autopolisher along with the samples in order to keep the machine balanced. It is recommended that an autopolisher be used rather than hand polishing in order to maximize the ability to reproduce results and to ensure that the polished surface is as flat as possible [84].

### 2.1.1 Coarse Polishing

The samples were first ground using 120 grit sandpaper. Coarser paper is typically reserved for ceramics and would damage most metal samples [85]. The samples were run in the

auto-polisher for 4 minutes at a time. After 4 minutes, the sandpaper was observed to see if the grit had been worn off and the samples were visually inspected.

At the 120 grit stage, a stream of water was used on the autopolisher to sweep metal shavings away from the samples and down the drain. It is recommended that the machine be set to 44.5 N or less [85]. The force should divide up to no more than 4.45 N per sample for coarse grinding. Coarse grinding paper needs to be replaced after every 8 to 10 minutes when used with titanium samples. 120 grit paper was used until all of the samples were completely uncovered.

After the samples were uncovered, the samples were washed with soap and water. 240 grit paper was then put on the autopolisher wheel. The samples and paper were checked every 4 to 5 minutes and the paper was replaced every 8 to 10 minutes. The samples did not need to be run for very long at the 240 grit stage.

At this point, there were two possible approaches to take. The first approach is cheaper, but takes more time, and involves moving onto 320 grit silicon carbide paper, then 400 grit silicon carbide paper, then 600 grit silicon carbide paper. The second approach is more expensive, but faster and involves switching to diamond slurry and more expensive polishing cloths. Most of the samples in this work were polished using the second method.

45 µm diamond slurry is the equivalent of about 250 grit sandpaper, so it is not very different from the 240 grit stage. This is also why the samples did not spend very long in the 240 grit stage. Samples can be run using Gold Cloth, 45 µm diamond slurry, a drop of Dawn dish soap and no water if the slurry is water-based. Gold Cloth is a woven nylon polishing cloth with an adhesive back [86].

If the slurry is oil based, then the samples should be run using Gold Cloth, the diamond slurry and no soap and no water. With water-based polishes, a drop of soap is used to keep

everything lubricated. With oil-based slurries, dish soap breaks oil down, so it would be counterproductive.

At this polishing stage, the polishing cloth and slurry were inspected every 5 minutes. If there did not appear to be enough slurry, then more was added along with more soap. The polishing cloth did not need to be swapped out as long as the same grit of polish was being used.

After every 10 minutes, the whole wheel was taken from the auto-polisher and washed with soap and water. It was then dried with a hot hand drier, similar to those used to dry hands in public restrooms. After that, the samples were squirted with isopropanol. Isopropanol, ethanol or methanol could be used. The samples were then blasted with compressed air. The samples were then observed under an optical microscope while still in the polishing wheel.

The magnification of the microscope does not matter and the direction of the scratches do not matter at this point. It is simply important to make sure that no scratches are much bigger than the rest. The size of the scratches should be uniform before moving onto the next step. Figure 2.4 shows an example of a sample with a few large scratches.

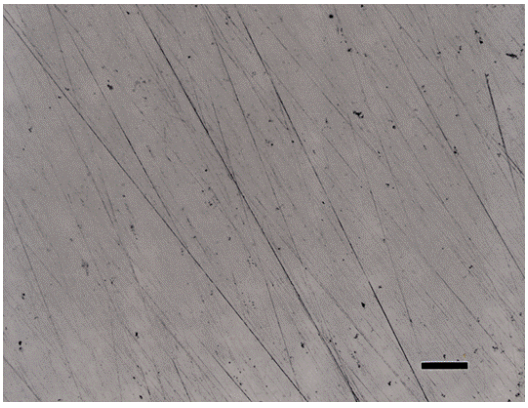

**Figure 2.4: A sample with a few large scratches [87]**

Once the scratches are all of a uniform size, it is possible to move on to the 15 µm stage. At that point, a 15 µm diamond slurry was used with Gold Cloth. While grit sizes between 15

μm and 45 μm do exist, they were not necessary. 15 μm diamond slurry was used with the same pressure, same time intervals, and no water on Gold Cloth. The samples were observed under the microscope and the polishing cloth was visually inspected the same as for the 45 μm stage.

After the 15 μm stage, 9 μm water-based diamond slurry was used with a drop of soap on Gold Cloth. The procedure used was the same as for the 15 μm diamond slurry.

### 2.1.2 Fine Polishing

After polishing with 15 μm diamond slurry, 6 μm water-based diamond slurry with a drop of dish soap on TexMet C cloth was used. TexMet C is a polishing cloth manufactured by Buehler that is used for polishing with diamond slurry [88]. The auto-polisher was set to apply 4.45 N of force per sample. The samples were washed with soap and water, dried with a hand dryer, squirted with isopropanol, and inspected with an optical microscope after every 10 minutes. When the 6 μm polishing stage was complete, the samples looked like a mirror to the naked eye.

Next was the 3 μm stage. 3 μm diamond slurry with a drop of soap on TexMet C cloth was used. When done with 3 μm, there should be no scratches visible to the naked eye.

Beyond the 3 μm stage, polishing is impractical on the autopolisher. It does not work as well as doing it by hand on a polishing wheel. The samples need to be polished one at a time rather than all at once when the polishing wheel is used.

It should also be noted that beyond the 3 μm stage, index card lapping no longer works. Index card lapping is when diamond paste is smeared on an index card and a metallography sample is rubbed against the index card to polish it. The reason it is no longer practical beyond that stage is because the paper fibers in the index card are too large for such fine polishing [85].

There are two ways to do the 1 µm stage of polishing. One way is easy and one way is fast. The easy way is to put samples into a Vibromet™ vibratory polisher with 1 µm diamond slurry for at least 4 hours, then into a Vibromet™ with 0.5 µm diamond slurry, then overnight into a Vibromet™ with 0.05 µm diamond slurry and a solution of 10% hydrogen peroxide with colloidal silica. Figure 2.5 shows a Vibromet™ polisher.


**Figure 2.5: Vibromet™ vibratory polisher [89]**

The solution of hydrogen peroxide with colloidal silica is used as a form of chemical mechanical polishing [90]. The hydrogen peroxide reacts with titanium and helps ensure that there is not mechanical deformation on the sample surface. This allows for a sample surface with fewer scratches.

The fast way to do the 1 µm stage of polishing is to put a piece of microcloth onto a polishing wheel and add 1 µm water-based diamond slurry with a drop of soap. Microcloth is a polishing cloth manufactured by Buehler [91]. After polishing the sample on that, the sample can be placed overnight into a Vibromet™ polisher with 0.05 µm diamond slurry and a solution of 10% hydrogen peroxide with colloidal silica.

After the samples were polished in the Vibromet™ polisher, they were cleaned with soap and water. To clean the samples, they were put sideways (so not metal side up or metal side down) into a 100 mL beaker with distilled water and a 2% micro-organic soap solution. The beaker was put into a vibrating cleaner for 10 minutes. After that, the sample was removed using a clean pair of tongs. It was then rinsed with a squirt bottle of distilled water, and dried using compressed air.

Next, the samples were cleaned using alcohol. The samples were placed one at a time into a 100 mL beaker. The sample was then covered with either high purity ethanol or isopropanol. The beaker was put into a vibrating cleaner for at least 5 minutes. After that, the sample was removed and squirted with alcohol from a squirt bottle. The samples were dried with compressed air, then sample caps were put on them.

Several different microscopy methods were attempted. Those methods looked at both etched and unetched samples. The methods tested were scanning electron microscopy with secondary detection, scanning electron microscopy with back scatter detection, optical microscopy, and polarized light optical microscopy. Optical microscopy with unpolarized light looking at an etched sample was found to be the fastest and easiest way to observe β grain morphologies for single layer pads. Optical microscopy with polarized light looking at an etched sample was found to be the fastest and easiest way to observe β grain morphologies for thin walls and multi-layer pads. Scanning electron microscopy with back scatter detection was found to be the method that produces the best micrographs for analyzing α-laths.

### 2.1.3 Etching

The samples which were prepared for β grain analysis were etched. Etching is a technique predominantly used when observing microstructures under optical light microscopy [92]. Background on etching is provided in the article "Contrast Enhancement and Etching" in Volume 9 of the ASM Handbook and is summarized here.

Etching increases the contrast of microstructural features in a sample by preferentially attacking certain features on the surface of the sample. Etching can be accomplished using chemical means such as acid mixtures, or physical means such as ion etching or thermal etching. This work utilized chemical etching.

In two-phase alloys such as Ti-6Al-4V, one phase will have a higher electrochemical potential than the other, and that phase will be preferentially attacked by the etchant. Grain boundaries are also attacked by chemical etchants due to their higher concentration of impurities and structural defects relative to the inside of the grain.

Before the samples were etched, they were placed in a Vibromet$^{TM}$ vibratory polisher overnight to remove any titanium dioxide that formed on the surface. The samples were then etched shortly after being polished and cleaned.

The single layer pad and multilayered pad geometries were etched using Kroll's Reagent. Kroll's Reagent is one of the most commonly used chemical etchants for titanium samples [93]. It is made by combining 92 mL of distilled water, 6 mL of nitric acid and 2 mL of hydrofluoric acid. The hydrofluoric acid in Kroll's reagent preferentially targets the α phase.

It was attempted to use Kroll's reagent to etch the thin wall samples, but it did not reveal the grain structure well enough for analysis. As a result, the thin wall samples were etched using Macro Kroll's Reagent rather than the regular Kroll's reagent. Macro Kroll's reagent is made by

combining 8 mL of hydrofluoric acid, 24 mL of nitric acid and 100 mL of distilled water. For some of the thin wall samples, the top etched at a different rate than the bottom. Because of that, it was necessary to observe the top and bottom of the sample under an optical microscope between etchings.

A standard etching time was not used because samples made with different powers and velocities etch differently due to differences in grain morphology. Rather, the samples were etched for a set time, then observed under an optical microscope to determine how well the β grains could be seen. Etching times for metals can vary greatly, so it is not unusual to judge the sample based on its appearance when a recommended etching time is not provided [92].

Single layer pads were etched for 30 seconds at a time before being observed under an optical microscope. Thin wall samples were etched for 10 seconds at a time before being observed under an optical microscope. Multilayered pad samples were etched for 30 seconds at a time before being observed under an optical microscope.

Figure 2.6 shows the effects of etching on a single layer pad sample. The images were taken using a Keyence VHX-600 series optical microscope with unpolarized light at 100x magnification. Figure 2.6*a* shows a sample that had not been etched long enough. Figure 2.6*b* shows a sample that had been etched too long. The etchant had attacked the grain boundaries for long enough that it left voids in the surface of the sample. An overetched sample needs to go through the fine polishing stages again. Figure 2.6*c* shows a sample that has been properly etched.


Figure 2.6: (a) An underetched single layer pad sample. (b) An overetched single layer pad sample. (c) A properly etched single layer pad sample.

## 2.2 β Grain Analysis Procedure

### 2.2.1 Single Layer Pads

This section considers single layer pad geometries and their analysis. The top view of a single layer pad geometry is shown in Figure 2.7.

Figure 2.7: a top view of a single layer pad geometry

Following the polishing and etching procedures previously described, the samples were viewed at 100x magnification using a Keyence VHX-600 series optical microscope. Figure 2.8 shows an example micrograph for β analysis.

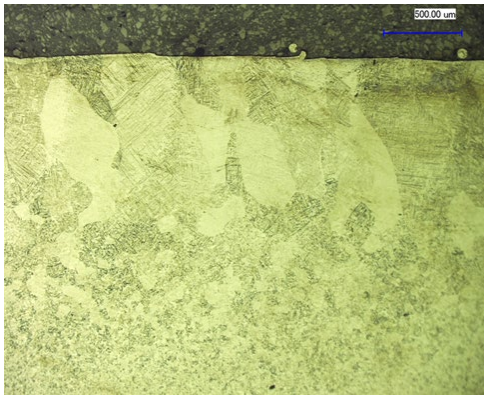


Figure 2.8: an example micrograph for β analysis

Optical microscopy was chosen because it allows for greater visibility of β grains than electron microscopy. The single layer pad samples were examined under non-polarized light. Many micrographs were taken for each sample. The images were then stitched. Rather than using a predetermined offset, the images were stitched by aligning features in Adobe Photoshop Elements. In order to align the features, the ability to alter the transparency of different layers in Photoshop was used. Figure 2.9 illustrates the stitching process.

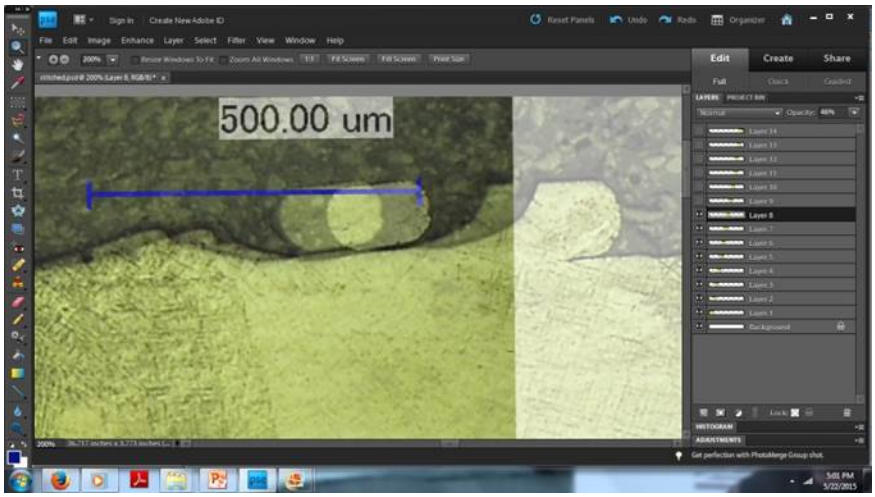


Figure 2.9: the stitching process

The stitching process was repeated with micrographs until the entire length of the sample had been made into a single image. Figure 2.10 shows an example of an entire stitched sample:

Figure 2.10: A stitched single layer pad sample

The β grains were then traced. This was done by creating a new layer in Photoshop, then using the brush tool. Figure 2.11 shows an example of traced β grains for a single layer pad:

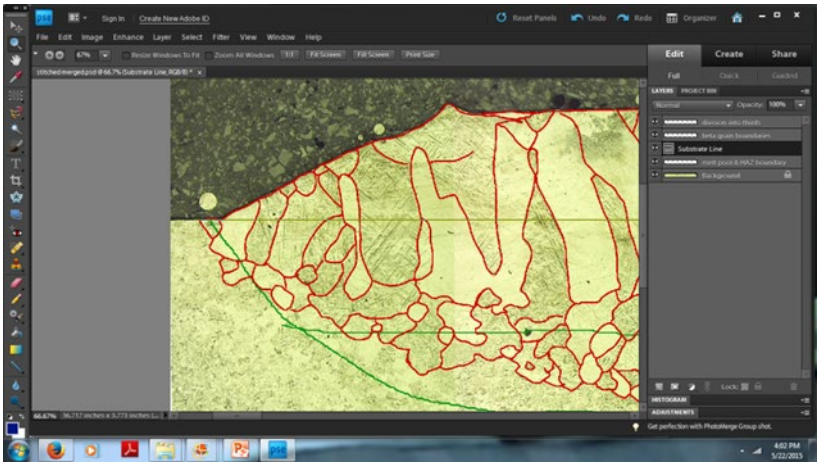

Figure 2.11: Traced β grains for a single layer pad

It is important to note that care must be taken when tracing β grains to determine whether the region being traced is a boundary between prior β grains or rather a boundary between α colonies.

The middle third of the pad was the focus of β grain measurements, because it was assumed that the middle third would be at steady-state conditions. Figure 2.12 shows the middle third of a sample with the β grains traced.


**Figure 2.12: The middle third of a single layer pad sample with the β grains traced**

The next step was to determine at what height the β grain widths should be measured. The determination of the height was made by measuring β grain widths at different heights and analyzing the results. The width of the β grains was measured using the ruler tool in ImageJ [94]. ImageJ is a public domain image processing program developed at the National Institutes of Health [95].

The ruler tool was calibrated to the micron bar in a micrograph. Figure 2.13 shows the ruler tool being calibrated in ImageJ. In order to calibrate the ruler, a set distance was measured and then input into the program. This was accomplished by clicking on the scale bar in each image. Figure 2.14 shows the data table in ImageJ. The measurements were then copied and pasted into Microsoft Excel.


Figure 2.13: The ruler tool being calibrated in ImageJ

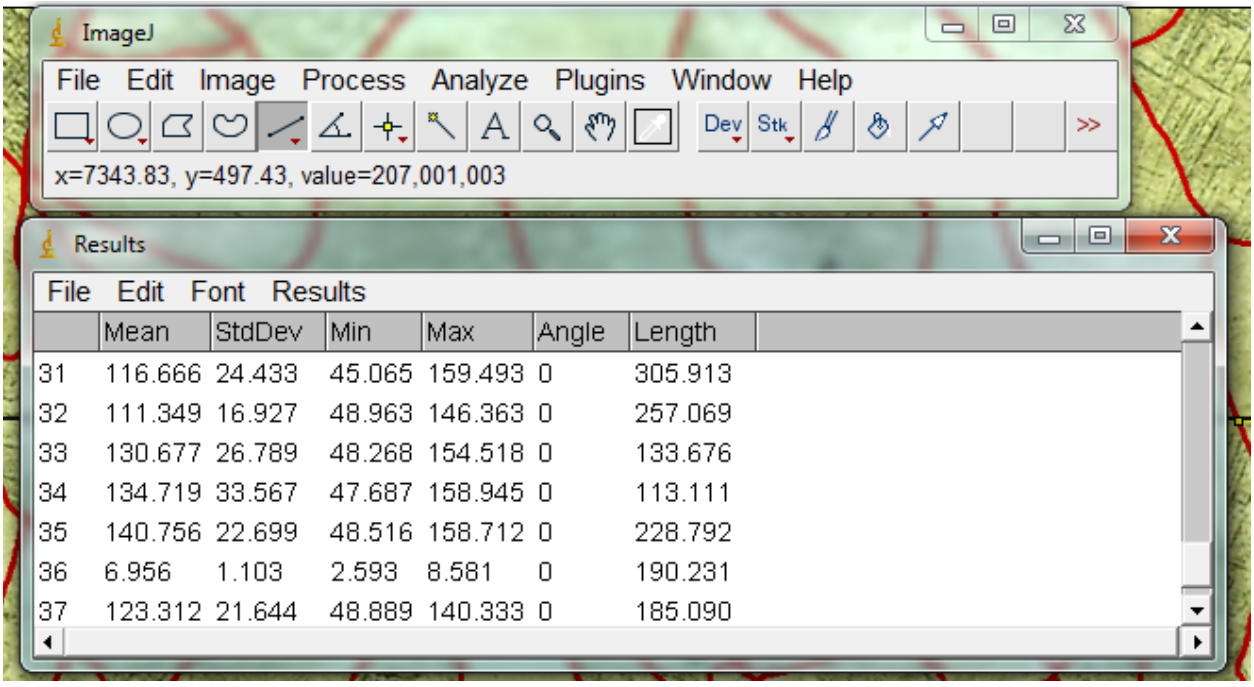


Figure 2.14: The data table in ImageJ

The three potential measurement heights that were tested were: the top of the substrate, at half of the maximum melt pool depth, and at half of the average melt pool depth. All three were examined for a test case: 450 Watts power and 7.5 inches per minute velocity. Figure 2.15 shows the three possible measurement heights superimposed on a section of the sample micrograph with traced β grains:

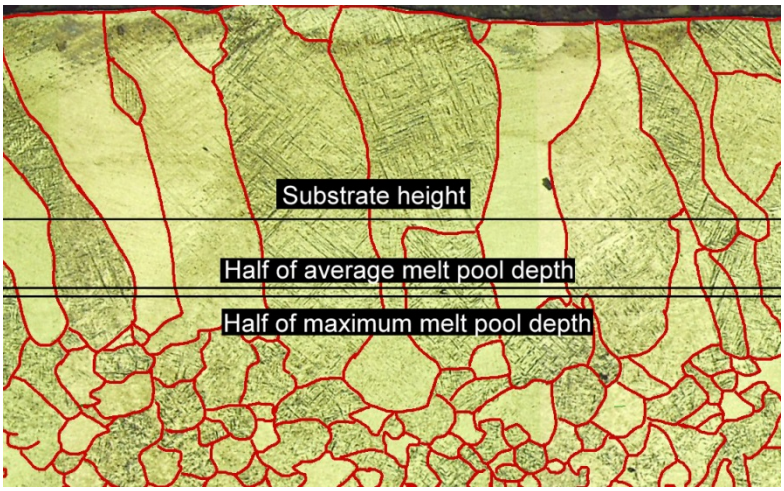


Figure 2.15: possible measurement heights superimposed on a section of the sample micrograph with traced β grains

| Line Placement | Number of β Grains | Average Width (μm) | 95% Confidence Interval (μm) | Standard Deviation (μm) |
|---|---|---|---|---|
| Top of Substrate | 37 | 191.7 | ± 33.3 | 103.4 |
| Half of max melt pool depth | 43 | 162.4 | ± 30.9 | 90.6 |
| Half of average melt pool depth | 40 | 175.1 | ± 32 | 87.7 |

Table 2.1: Measurements from the test case

Table 2.1 shows the results of the test case. The measurements were made at half the maximum melt pool depth, because it has the smallest confidence interval. A 95% confidence interval means that a person can be 95% confident that the true mean falls within a certain range [96]. That range is the sample mean plus or minus the reported confidence interval in the table. Measuring half of the maximum melt pool depth was also found to yield the most consistent results.

### 2.2.2 Thin Wall Geometries

This section will look at β grain analysis for thin wall geometries. Figure 2.16 shows some of the thin wall samples before they were cut and mounted. The samples were made from Ti-6Al-4V using the LENS$^{TM}$ process.

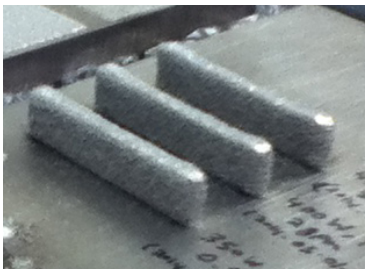

Figure 2.16: Thin wall samples on the substrate

The samples were viewed at 200x magnification using a Keyence VHX-600 series optical microscope. It was the lowest magnification at which grains could be seen well enough to measure.

It was found that regular light microscopy as was used for the single layer pads made it difficult to see the β grain morphology of the thin wall samples. It was found to be easier to see the β grains when the samples were imaged under polarized light. Materials with non-cubic crystal structures, such as α-Ti respond well to polarized light [97].

Figure 2.17(*a*) shows a micrograph under regular light and Figure 2.17(*b*) shows the same micrograph under polarized light. The sample that is pictured is a LENS$^{TM}$ Ti-6Al-4V thin wall that was manufactured at Penn State. The beam power was 400 W, the velocity was 16.4 ipm and the powder feed rate was 2 gpm.

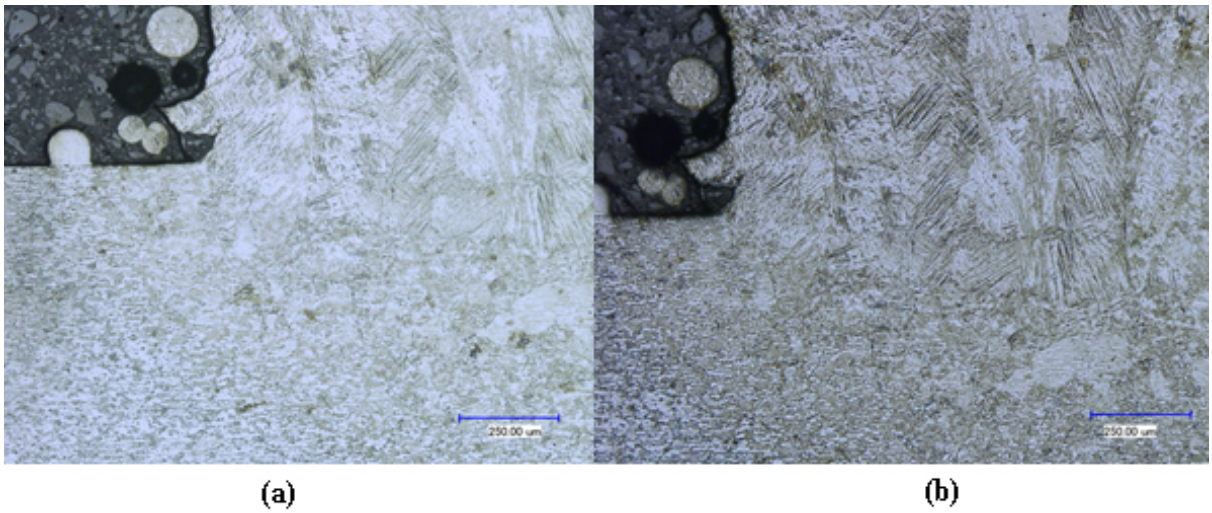


Figure 2.17: (a) an etched thin wall sample under regular light (b) an etched thin wall sample under polarized light

The micrographs were stitched using Adobe Photoshop CS5. Stitching was completed manually via feature alignment rather than using a standard overlap. ImageJ was used to measure from the middle of the substrate level to the top of the sample. The height of the sample was divided into thirds. Figure 2.18 shows a thin wall divided into thirds.

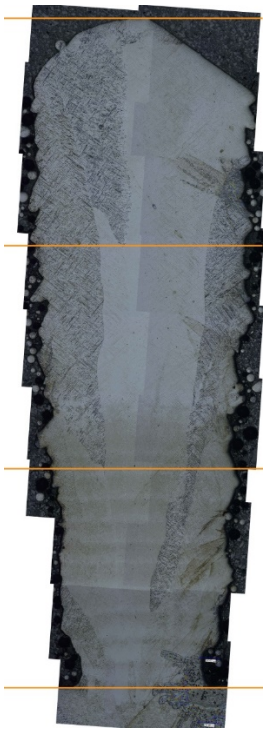

Figure 2.18: a thin wall sample divided into thirds

β grains were traced by creating a new layer in Photoshop and using the brush tool. The procedure was the same as for tracing β grains for the single layer pads. Figure 2.19 shows part of a thin wall sample with the β grains traced.

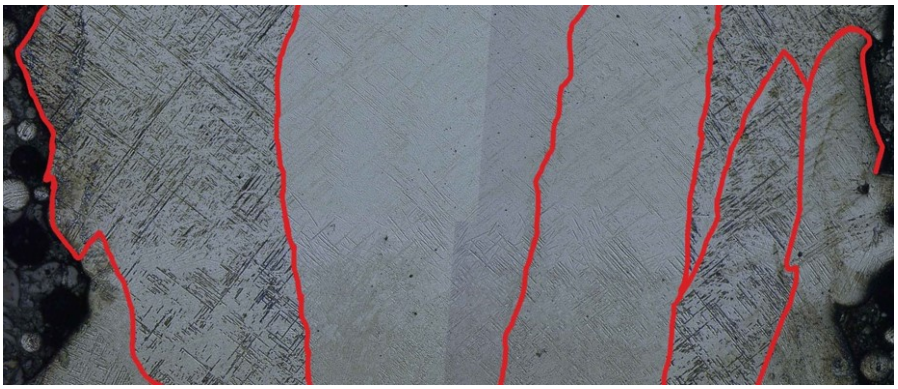

**Figure 2.19: a thin wall sample with traced β grains**

The width of the β grains for each section was measured in the middle of each section. The green lines in Figure 2.20 show where the β grain measurements were made.

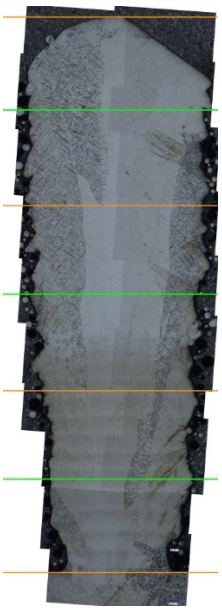

**Figure 2.20: a thin wall sample. β grain measurements were taken along the green lines**

### 2.2.3 Multi-layer Pads

This section considers multi-layer pad geometries and their analysis. Figure 2.21 shows one of the multi-layer pad samples before it was cut and mounted.

Figure 2.21: a multi-layer pad sample

The samples were viewed 200x magnification using a Keyence VHX-600 series optical microscope. It was the lowest magnification at which grains could be seen well enough to measure. The samples were imaged using polarized light.

The micrographs were stitched using Adobe Photoshop CS5. An attempt was made at using Adobe Photoshop Elements, but the images were too high resolution for that software to handle. Stitching was completed manually via feature alignment rather than using a standard overlap. Figure 2.22 shows the stitching process using feature alignment. Figure 2.23 shows multiple images being stitched together in Photoshop.

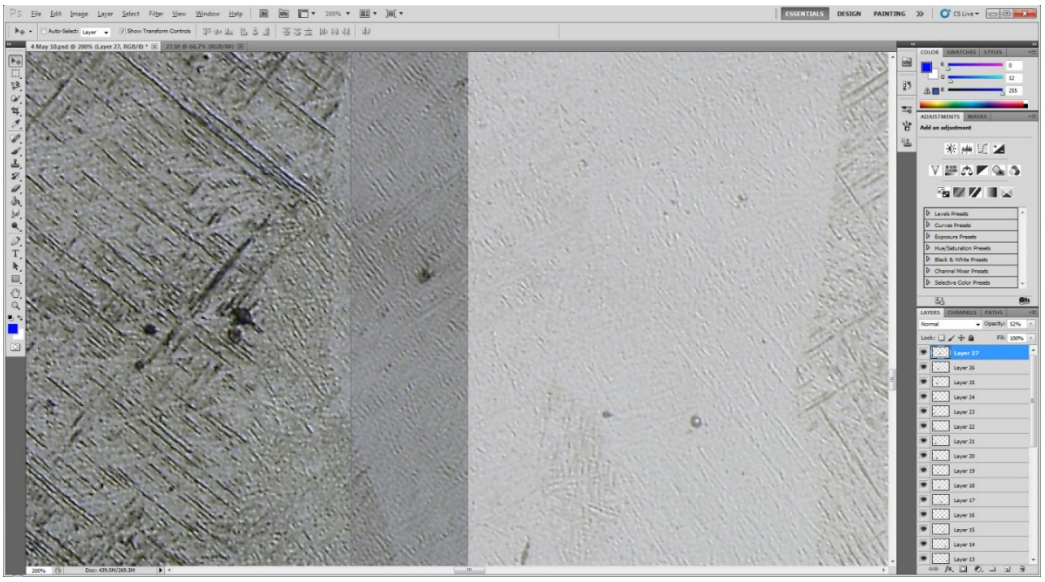

Figure 2.22: Manual feature alignment being used to stitch micrographs for a multi-layer pad in Adobe Photoshop CS5

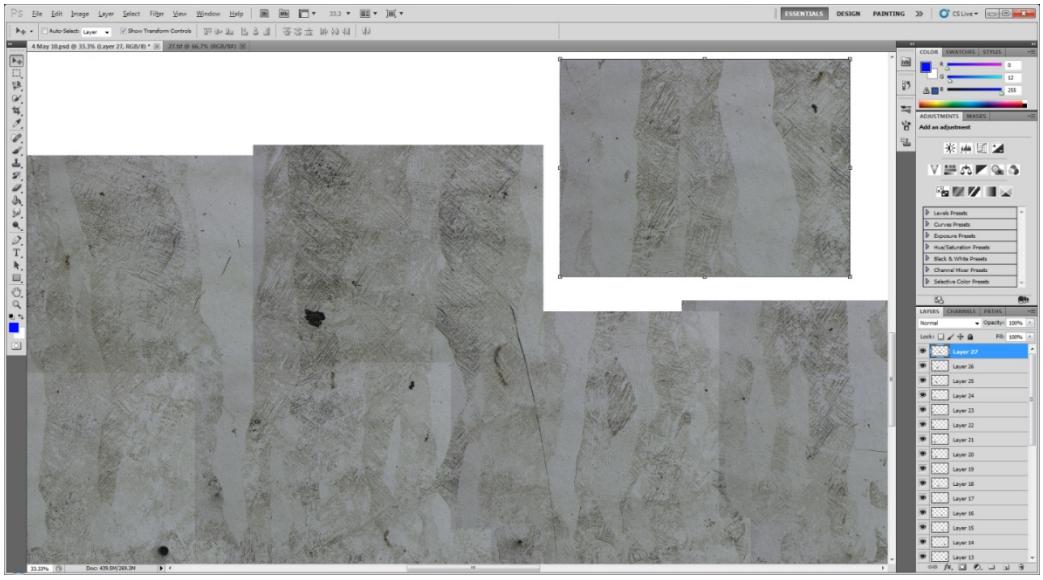

Figure 2.23: Micrographs for a multi-layer pad sample being stitched in Adobe Photoshop CS5

ImageJ was used to measure from the middle of the substrate level to the top of the sample. Both the height and the width of the sample were divided into thirds. Figure 2.24 shows the height of the sample divided into top, middle, and bottom thirds. Figure 2.25 shows the width of the sample being divided into thirds.

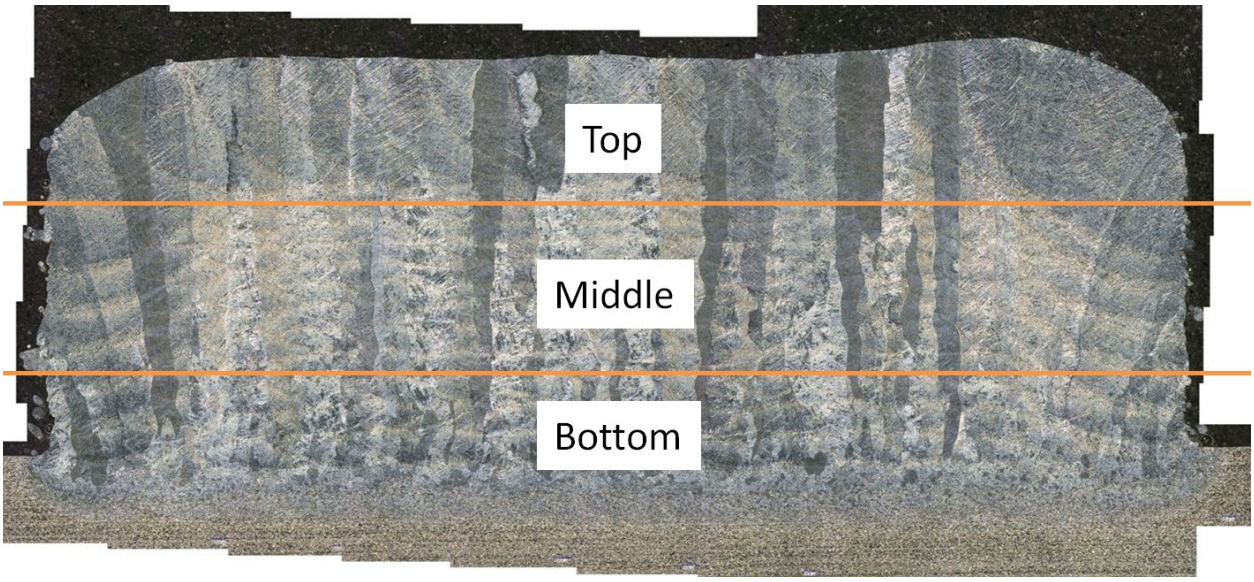


Figure 2.24: a multi-layer pad sample being divided vertically into thirds

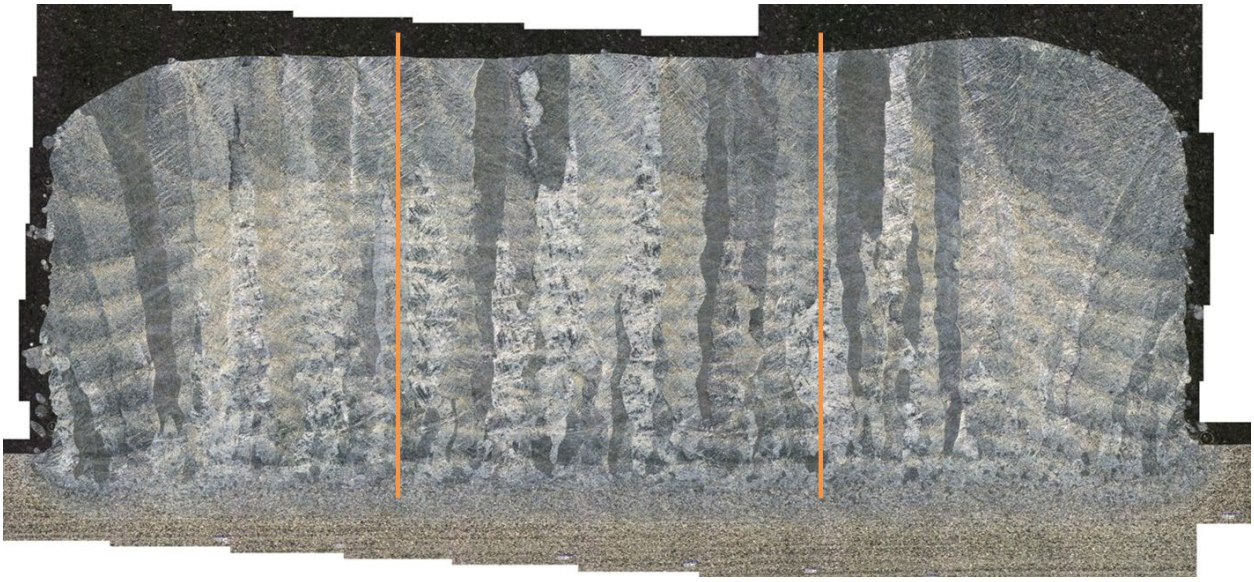

Figure 2.25: a multi-layer pad sample being divided horizontally into thirds

β grains were traced by creating a new layer in Photoshop and using the brush tool. The procedure was the same as for tracing β grains for the single layer pads and thin walls. The widths of the β grains for the multi-layer pads were measured in the middle third of the sample to avoid measuring pinched grains at the edges of the sample.

## 2.3 α-lath Analysis for Single Layer Pads

Five single layer pad samples were prepared for α-lath analysis. After being mounted and polished, they were imaged using a Sirion XL30 scanning electron microscope. Back scatter detection was used, and the images were taken at 2000x magnification [98]. The images were saved using the tagged image file format (*.tiff), so they were not compressed.

The images were then imported into Adobe Photoshop CS2 along with the FoveaPro plugin by Reindeer Graphics. The micron bar was measured and converted to a number in pixels then saved. That allowed the software to properly scale its measurements.

Next the brightness and contrast were increased for the micrographs. A copy of the image was then made and superimposed on the original. A Gaussian Blur was applied to one of the layers, and one layer was subtracted from the other. A Gaussian Blur is a type of filter that eliminates components of an image with large variations in brightness [99]. In other words, it helps to remove speckles and noise.

A threshold filter was then applied using FoveaPro. A threshold filter converts a grayscale image into a binary image that only contains black and white pixels [99]. Finally, a skeletonization filter was used. The skeletonization filter decreases the thickness of all the lines in an image to a single pixel [99].

Figure 2.26 shows the image processing for a Ti-6Al-4V single layer pad laser glazed (no added material) using the LENS$^{TM}$ process. The power was 350 watts and the velocity was 7.5 inches per minute.

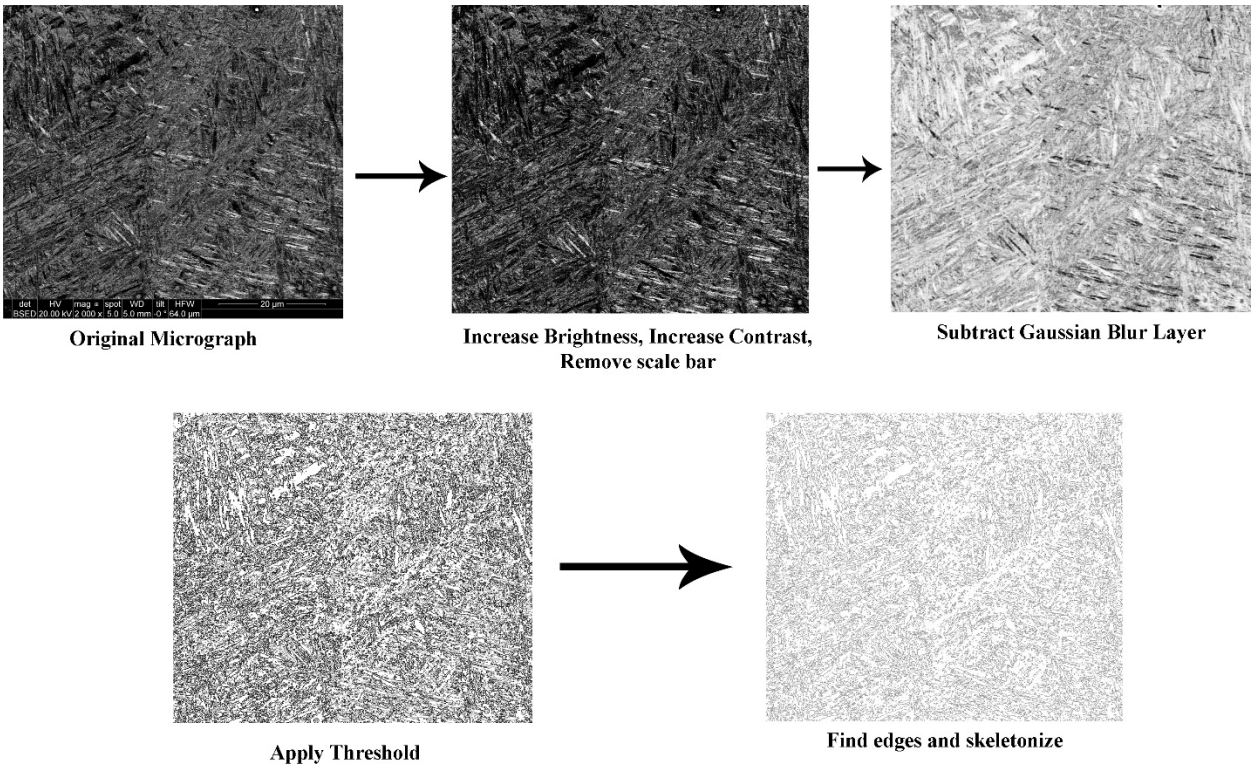


**Figure 2.26: Image processing using FoveaPro for α-lath measurements for a single layer pad**

After the micrograph was converted to a binary image with thin lines, it could be measured. The mean inverse intercept was measured using FoveaPro. In order to find the mean inverse, the software generates a grid of parallel lines and determines the lengths of the intercepts. It then rotates the grid by 10 degrees and repeats the process through a full 360 degree rotation [99]. The software takes the inverse of every intercept value and then calculates the mean [100].

Simply calculating the mean intercept without taking the inverse of the values is suitable for equiaxed grains, but not for Widmanstätten α-laths. The mean inverse intercept is what is used to estimate the "true three-dimensional thickness" of thin structures such as oxide layers and α-laths [44].

## 2.4 Structural component geometries

Two structural component geometry samples were constructed using an Optomec® LENS™ MR-7 system at Penn State [101]. The components were made from Ti-6Al-4V. One sample was built with a 0s dwell and the other was built with a 4s dwell time between layer depositions. Figure 2.27(*a*) shows the 0s dwell component and Figure 2.27(*b*) shows the 4s dwell component.

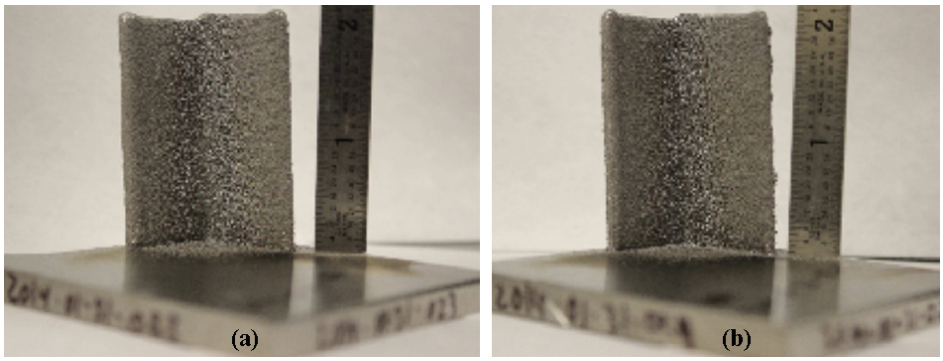


Figure 2.27: The structural component geometries as manufactured [101]

Figure 2.28 shows the deposition path that the laser followed as the samples were constructed. Each layer was constructed using 8 passes of the laser.

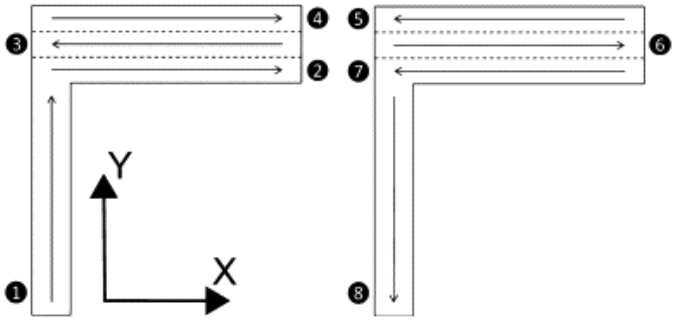


Figure 2.28: the hatch pattern for laser deposition of the structural component geometries [101]

Thermal data for the structural component geometries was collected as they were deposited. A Stratonics, Inc. ThermaViz® optical sensor was used to record thermal images [101]. The images were analyzed to determine temperature and the thermal gradient at the trailing edge of the melt pool.

The samples underwent metallographic preparation. First, the sample was cut vertically using an Allied TechCut 5$^{TM}$ precision high speed saw. Liquid coolant was sprayed on the blade and sample as it was cut. Figure 2.29 shows the saw.

**Figure 2.29: The saw used to make the vertical cut in the structural component samples [102]**

Figure 2.30 shows a 3-D representation of the sample. The striped translucent plane is the cutting plane.

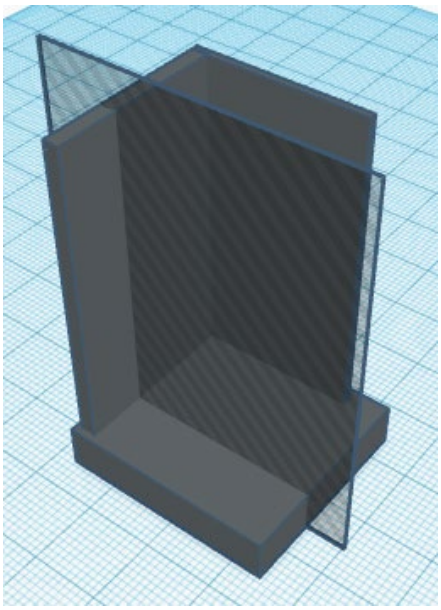

**Figure 2.30: A 3D representation of the vertical cut that was made in the structural component sample**

After that, most of the substrate was removed using the same saw. The sample was still too large to fit into the mounting press, so it was cut into three pieces. Figure 2.31 shows a representation of the sample. The striped translucent plane was where it was cut.

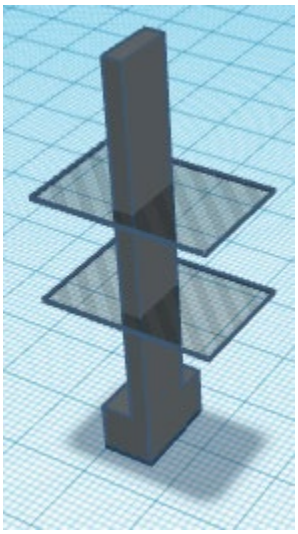

**Figure 2.31: a 3D representation of cuts that were made in the structural component samples**

The saw used to cut the sample was an Allied TechCut 4$^{TM}$ precision low speed saw. Figure 2.32 shows the saw.


**Figure 2.32: The Allied TechCut 4$^{TM}$ precision low speed saw that was used to cut the structural component samples [103]**

The samples were mounted in Polyfast conductive mounting media. Figure 2.33 shows the 3-bead leg of the 4 second dwell component, in its mount.

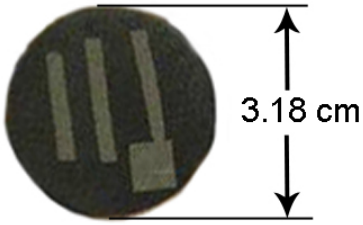


Figure 2.33: the 3-bead leg of the 4 second dwell component in its mount

The samples were polished on a polishing wheel rather than using an autopolisher. They were ground using 120 grit silicon carbide paper until they were uncovered. Next, they were polished using 240 grit, 320 grit, 400 grit then 600 grit silicon carbide sandpaper. The samples were washed with soap and water between grinding stages. Scratches were observed the same way as described in the metallographic procedure for the single layer pad, thin wall and multi-layer pad samples.

After the coarse grinding was completed, the samples were polished on gold cloth polishing cloth with 9µm water-based diamond slurry along with a solution of 20% hydrogen peroxide with colloidal silica and a drop of dish soap.

The sample was washed with soap and water, dried with a hot hand drier, squirted with isopropyl alcohol and blasted with compressed air. The scratches were observed under an optical microscope and once it was determined that they were of uniform size and direction, the sample went on to the next step.

Next the samples were polished on a Texmet C polishing cloth with a 3 µm water-based diamond slurry, a solution of 10% hydrogen peroxide with colloidal silica and a drop of dish soap. The sample was washed with soap and water, dried with a hot hand drier, squirted with isopropyl alcohol and blasted with compressed air. The scratches were observed under an optical microscope and once it was determined that they were of uniform size and direction, the sample went on to the next step.

The sample was then polished on a microcloth polishing cloth along with 1 μm water-based diamond slurry, a solution of 10% hydrogen peroxide with colloidal silica and a drop of dish soap. The sample was washed with soap and water, dried with a hot hand drier, squirted with isopropyl alcohol then blasted with compressed air.

The sample was put into a Vibromet™ vibratory polisher with 0.05 μm diamond slurry, and a solution of 10% hydrogen peroxide with colloidal silica overnight. Unlike the single layer pad, thin wall and multi-layer pad samples, the structural component samples did not need to undergo polishing in a Vibromet™ with 1μm diamond slurry. This is because the 1μm polishing stage for the structural component samples was completed by hand.

After the samples were polished in the Vibromet™ polisher, they were cleaned with soap and water. To clean the samples, they were put sideways (so not metal side up or metal side down) into a 100 mL beaker with distilled water and a 2% micro-organic soap solution. The beaker was put into a vibrating cleaner for 10 minutes. After that, the sample was removed using a clean pair of tongs. It was then rinsed with a squirt bottle of distilled water, and dried using compressed air.

Next, the samples were cleaned using isopropyl alcohol. The samples were placed one at a time into a 100 mL beaker. The sample was then covered with either high purity ethanol or isopropanol. The beaker was put into a vibrating cleaner for at least 5 minutes. After that, the sample was removed and squirted with alcohol from a squirt bottle. The samples were dried with compressed air, then sample caps were put on them.

After polishing was complete, the samples were examined using a Sirion XL30 scanning electron microscope. The samples were not etched before being placed in the SEM. The microscope has an electron backscatter diffraction (EBSD) detector which was also used.

Images were taken at six different locations on the samples. Figure 2.34 shows the locations at which SEM images and EBSD data were collected. The pictured sample is the 4 second dwell sample. The middle column of the figure shows SEM and EBSD images. The black and white images are SEM and the color images are EBSD. The right column shows binary images that were produced using MIPAR.™

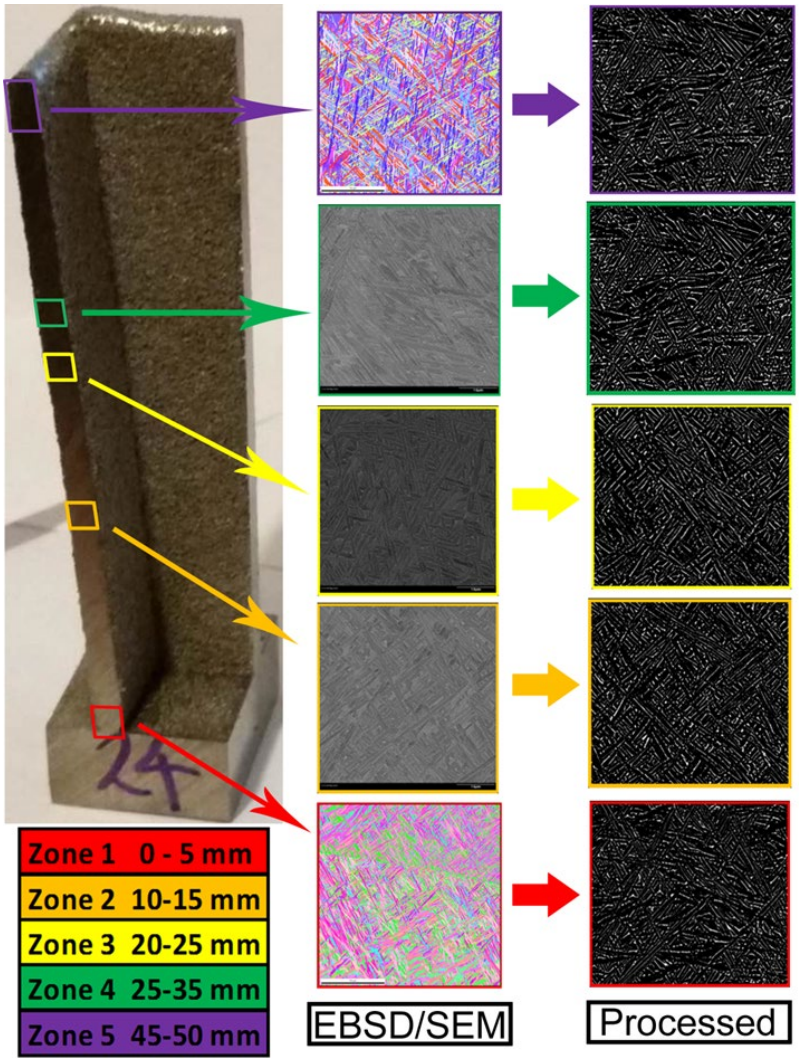


Figure 2.34: Heights at which measurements were taken for the structural component samples [104]

MIPAR™ stands for Materials Image Processing and Automated Reconstruction [48]. It is a MATLAB™ based program for material analysis. When using MIPAR™, a "recipe" of steps

can be developed to transform a greyscale image into a binary image. A batch processor allows the same recipe to be quickly applied to many images.

The collection of α-lath data is detailed by Loughnane [104]. That work developed uncertainty quantification by comparing probability distribution functions for mean linear intercepts and compared α-lath widths to thermal data collected by Kriczky et al [101]. This work compares the α-lath widths and thermal data to Vickers hardness data.

### 2.5 Hardness measurements and hardness maps

This section discusses the procedure used to test the hardness of the structural component samples. This work utilized the Vickers microhardness test. Two of the samples were tested on automated hardness equipment at The Ohio State University. Those samples were the 3-bead leg sections of the components. The 1-bead leg sections of the components were tested manually at the Air Force Research Laboratory.

The spacing used for the automatic hardness measurements was 500 μm. The hardness tests in this work did not all utilize the same load. As discussed in the first chapter of this thesis, different loads can be used for Vickers microhardness testing. The size of the indent relative to the applied load is what matters, not the load itself. The 3-bead leg of the 0 second dwell sample was tested with a load of 100 gf. Approximately 550 data points were collected for that sample. The 3-bead leg of the 4 second dwell sample was tested with a load of 300 gf. Approximately 500 data points were collected for that sample.

Data was collected for the top, bottom, and middle portions of the sample then stitched together. Figure 2.35 shows the hardness maps for the portions of the sample and a complete map for the 3-bead leg of the 4 second dwell sample.

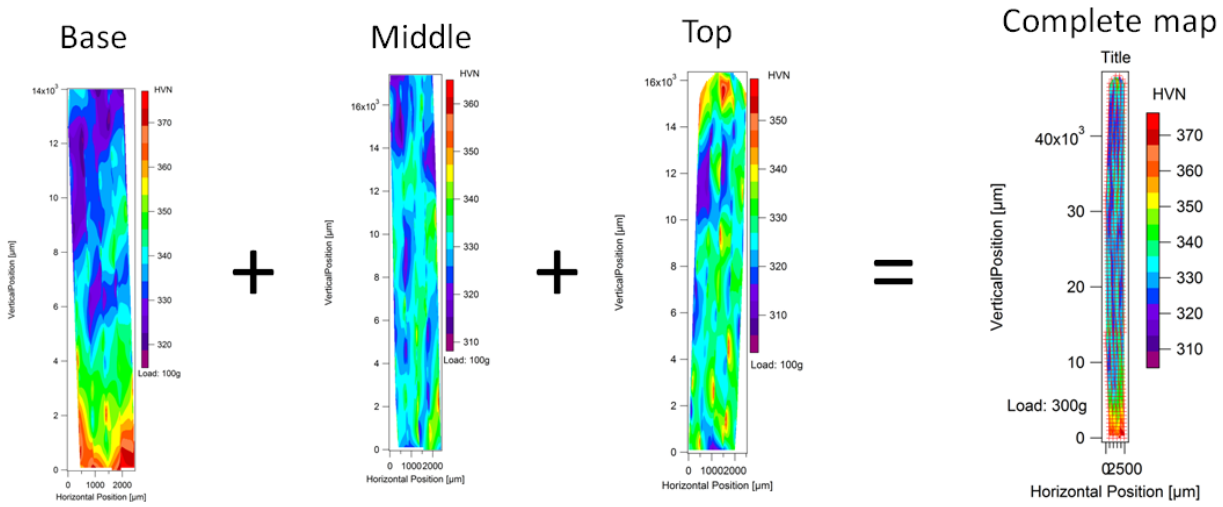


**Figure 2.35: Portions of the sample and a complete hardness map for the 3-bead leg of the 4 second dwell sample**

The maps were made in portions because the structural components were too large to fit into a metallographic mounting press.

# 3 Results and Discussion

## 3.1 β Analysis Results

### 3.1.1 Single Layer Pads

Table 3.1 shows data collected from the single layer pads. The power, velocity, and feed rate were given process variables. The incident energy was calculated by dividing the power by the velocity.

| Incident Energy (kJ/m) | Power (Watts) | Velocity (inches per minute) | Feed (grams per minute) | Grain Size (microns) |
|---|---|---|---|---|
| 24 | 250 | 25 | 3 | 69 |
| 24 | 250 | 25 | 3 | 78 |
| 110 | 350 | 7.5 | 0 | 183 |
| 110 | 350 | 7.5 | 0 | 160 |
| 110 | 350 | 7.5 | 3 | 248 |
| 50 | 350 | 16.4 | 2 | 125 |
| 50 | 350 | 16.4 | 2 | 125 |
| 65 | 400 | 16.4 | 0 | 116 |
| 65 | 400 | 16.4 | 2 | 176 |
| 65 | 400 | 16.4 | 3 | 143 |
| 142 | 450 | 7.5 | 0 | 225 |
| 142 | 450 | 7.5 | 0.9 | 242 |
| 142 | 450 | 7.5 | 3 | 405 |
| 43 | 450 | 25 | 0 | 91 |
| 43 | 450 | 25 | 3 | 172 |
| 43 | 450 | 25 | 3 | 119 |

**Table 3.1: Incident energy, power, velocity, feed rate and β grain size for single layer pad samples**

Figure 3.1 shows the β grain width vs. the beam power for sets of single layer pads that were made using the same velocity and feed rate. Linear regressions were calculated and the trend lines are shown on the chart.

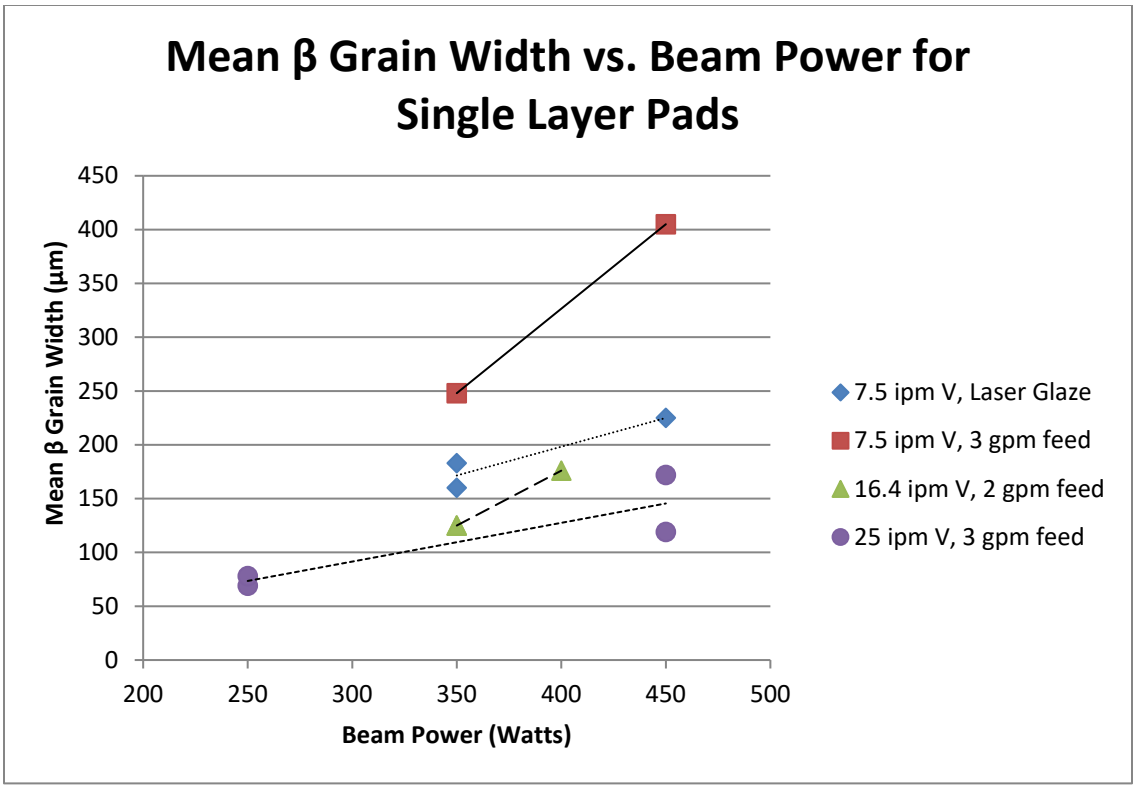


Figure 3.1: Mean β grain width vs. beam power for single layer pads

When power and feed rate are held constant, increasing velocity was found to decrease β grain widths. Figure 3.2 shows the β grain width vs. the beam velocity for sets of single layer pads that were made using the same power and feed rate. The pads manufactured with a beam power of 450 W were chosen because that set had the most samples with different velocities. Linear regressions were calculated and the trend lines are shown on the chart. When velocity and feed rate are held constant, increasing power was found to increase β grain widths.

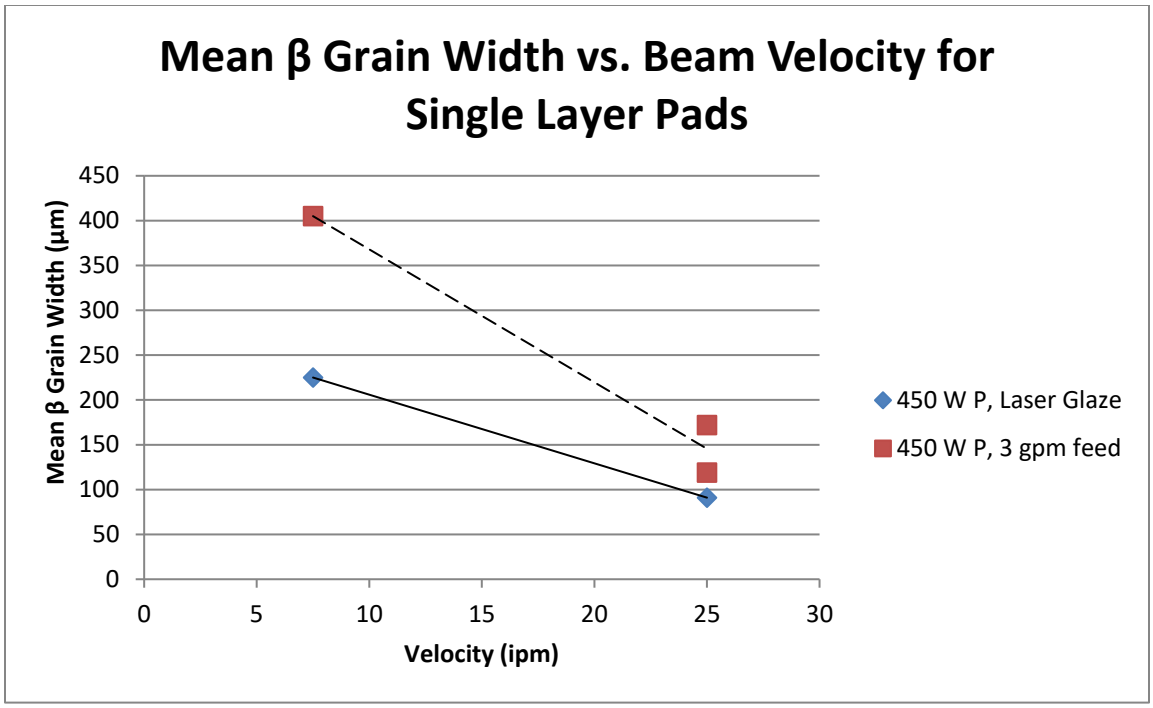


Figure 3.2: Mean β grain width vs. beam velocity for single layer pads

The incident energy was compared to the average β grain width for single layer pads. The comparison was made looking at pads that had the same feed rate in order to not introduce an additional variable. Figure 3.3 shows the average β grain width vs. incident energy for single layer pads.

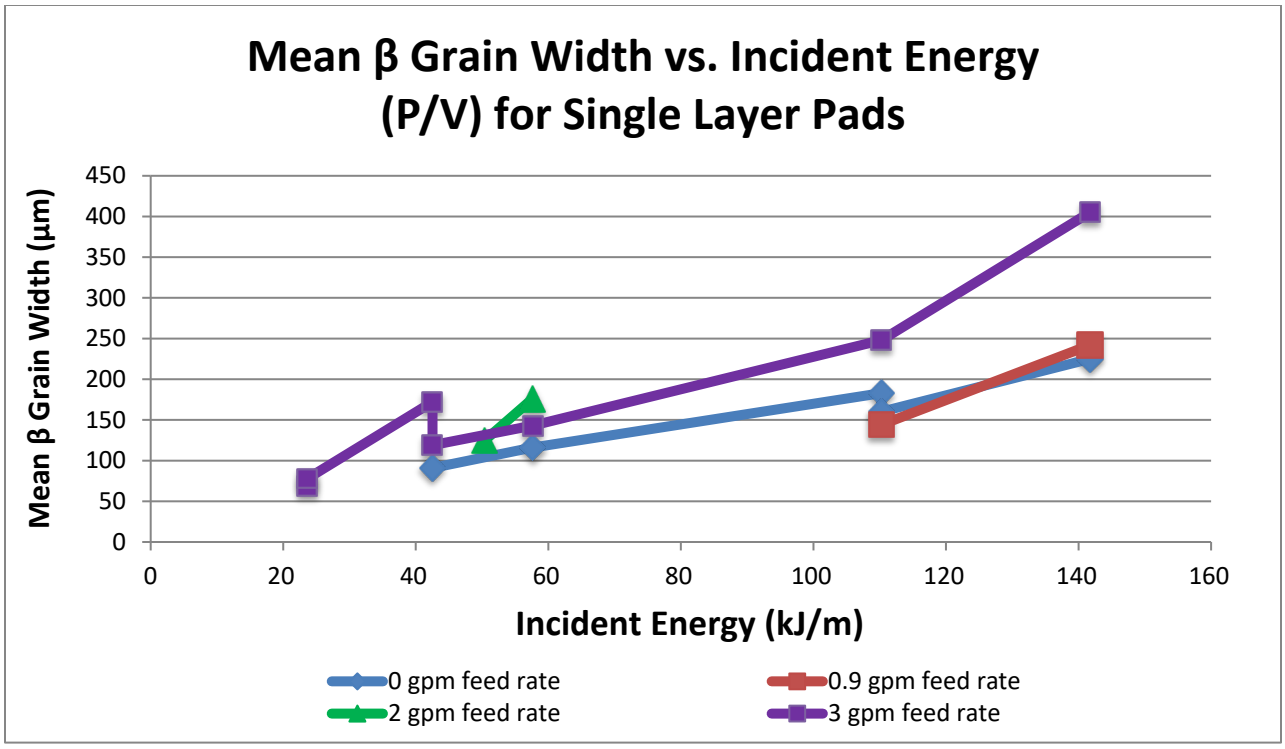


Figure 3.3: Mean β grain width vs. incident energy (P/V) for single layer pads

It was found that for constant feed rate, increasing incident energy increases β grain width in single layer pads. The more energy that is put into a part, the longer it takes to cool. This allows the β grains to grow wider.

For the same incident energy, samples with a larger feed rate appear to have larger β grain widths. This could be because more material means more time needed to heat it up and cool it down. In 2015, Bagheri, et al performed an experiment to determine the effects of powder feed rate on parts made from LENS$^{TM}$ deposited Ti-6Al-4V [105]. It was found that increasing feed rate while keeping power and velocity constant increases grain size at the bottom of the part. The effect of feed rate on grain size in the middle and top of the part was found to be "negligible".

As incident energy increases, melt pool size also increases. In 2010, Soylemez, et al observed single beads of electron beam deposited Ti-6Al-4V [106]. Experimental results showed that decreasing beam velocity increases the cross-sectional area of the melt pool. Modeling results

showed that while generally increasing $\frac{P}{V}$ increases melt pool dimensions, the relationship is not perfectly linear, and it would be unwise to assume a "rule of thumb" that keeping incident energy constant keeps melt pool cross sectional area constant.

In 2016, Kusuma observed single beads of Ti-6Al-4V produced by selective laser melting [107]. Rather than "incident energy", "linear laser energy density" was the terminology used to refer to energy put into the current deposition layer. Linear laser energy density shares similar units to incident energy (J/mm instead of kJ/m) and is also calculated by dividing the beam power by the scanning speed. It was found that melt pool width increases as linear laser energy density increases. Melt pool width can be related to the cross-sectional area of the melt pool, and controlling melt pool cross sectional area allows for the maintenance of a constant beta grain size in additively manufactured Ti-6Al-4V [33].

Research conducted by Gockel suggested that as melt pool areas increase, β grain sizes increase as well [33]. In fact, in a set of single beads manufactured with different power and velocity settings that changed the melt pool cross-sectional area, the number of β grains across the melt pool stayed relatively constant. For the single layer pads in this work, an increase in melt pool cross-sectional area as incident energy increases could offer another explanation as to why beta grain widths increased with incident energy.

### 3.1.2 Thin Walls

Table 3.2 shows the β grain data for the bottom third of the thin walled structures.

| Incident Energy (kJ/m) | Power (Watts) | Velocity (inches per minute) | Feed Rate (grams per minute) | Number of Grains | Mean Width (microns) | Standard Deviation (microns) | 95% Confidence Interval (microns) |
|---|---|---|---|---|---|---|---|
| 110 | 350 | 7.5 | 0.9 | 6 | 387 | 235 | ± 188 |
| 110 | 350 | 7.5 | 0.9 | 4 | 648 | 371 | ± 363 |
| 110 | 350 | 7.5 | 3 | 6 | 428 | 316 | ± 253 |
| 65 | 400 | 16.4 | 2 | 9 | 257 | 160 | ± 105 |
| 65 | 400 | 16.4 | 3 | 9 | 253 | 144 | ± 94 |
| 43 | 450 | 25 | 3 | 7 | 308 | 155 | ± 115 |
| 43 | 450 | 25 | 3 | 10 | 216 | 90 | ± 56 |
| 43 | 450 | 25 | 3 | 5 | 401 | 414 | ± 363 |
| Average | | | | 7 | 362 | 236 | ± 192 |

**Table 3.2: Incident energy, power, velocity, feed rate and β grain size for the bottom third of the thin wall samples**

Figure 3.4 shows the mean β grain width versus the incident beam energy for the bottom portion of the thin walled structures. Increasing β grain with increasing incident energy makes sense. More energy means longer for the grain to cool and longer for it to grow.

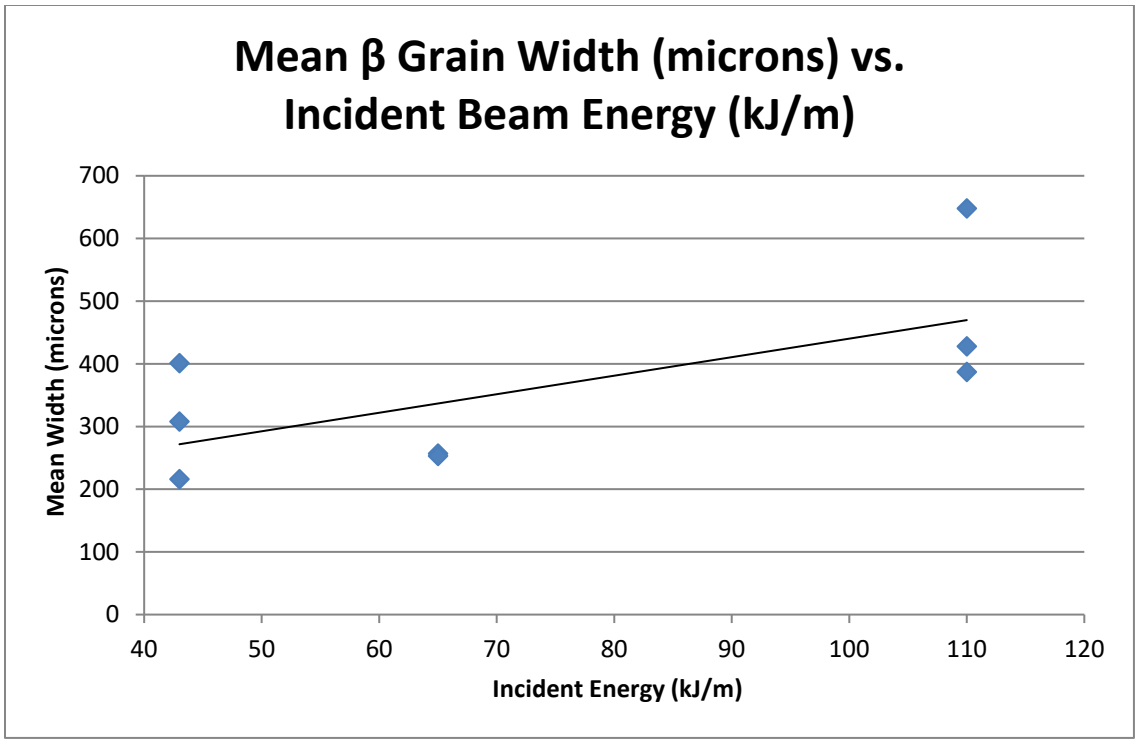


**Figure 3.4: Mean β grain width vs. incident beam energy for the bottom portion of the thin walled structures**

While β grain size was found to increase with incident energy, there was high variability. Part of this could be due to the small sample size; all of the thin wall samples had ten β grains or less across the width. It is difficult to draw any conclusions about the effect of feed rate for this set of samples, also possible because the small number of grains across each thin wall.

Standard deviation can be defined as "a quantity that measures the degree of spread in a sample" [96]. Standard deviation is calculated as

$$S_x = \sqrt{\frac{\sum |x - \bar{x}|^2}{(n-1)}}; \tag{3}$$

where $S_x$ is the standard deviation, $x$ is the width of a β grain, $\bar{x}$ is the mean, and $n$ is the sample size. A smaller sample size will always yield a larger standard deviation, if all else is equal. It is important to note that the above formula is for the sample standard deviation rather than the true standard deviation because the measured prior β grains are part of a finite data set [108].

This thesis discusses the variability of β grains, which is a qualitative observation. It is not to be confused with variance, which is a quantitative measure calculated by taking the square of the standard deviation. Sample standard deviations can also be reported as percentages of the mean, and they can be used to calculate confidence intervals [84]. Standard deviation is often used to report sample spread instead of variance because it uses the same units as the raw data.

Confidence intervals are used in order to estimate the true mean of a finite sample of measurements [96]. A 95% confidence level means that 95% of possible confidence intervals contain the true mean of the sample. In other words, if a population is sampled repeatedly and confidence intervals are calculated for each sample, 95% of them will contain the true mean. For microstructural characterization applications, a 95 percent confidence interval is useful [84]. The 95% confidence level is calculated as

$$95\%\ CL = \frac{ts}{(N-1)^{\frac{1}{2}}}; \tag{4}$$

Where $N$ is the sample size, $s$ is the sample standard deviation and $t$ varies with the sample size. The value of $t$ can be taken from the student's $t$ table.

According to Vander Voort, sometimes rather than varying $t$ with sample size, a value of 2 or 1.96 will be used as a standard value instead [84]. In this research, Microsoft Excel 2010 was used to calculate the 95% confidence intervals, and the software uses a standard value of 1.96 for $t$ rather than varying it with sample size [109]. Like the standard deviation, it is also possible to report confidence intervals as a percentage of the mean. When it is reported that way, it is called "percent relative accuracy" [84].

Some of the β grains also appeared to be pinched or squished at the free edge. Figure 3.5 shows an example of a thin wall with the prior β grains traced.

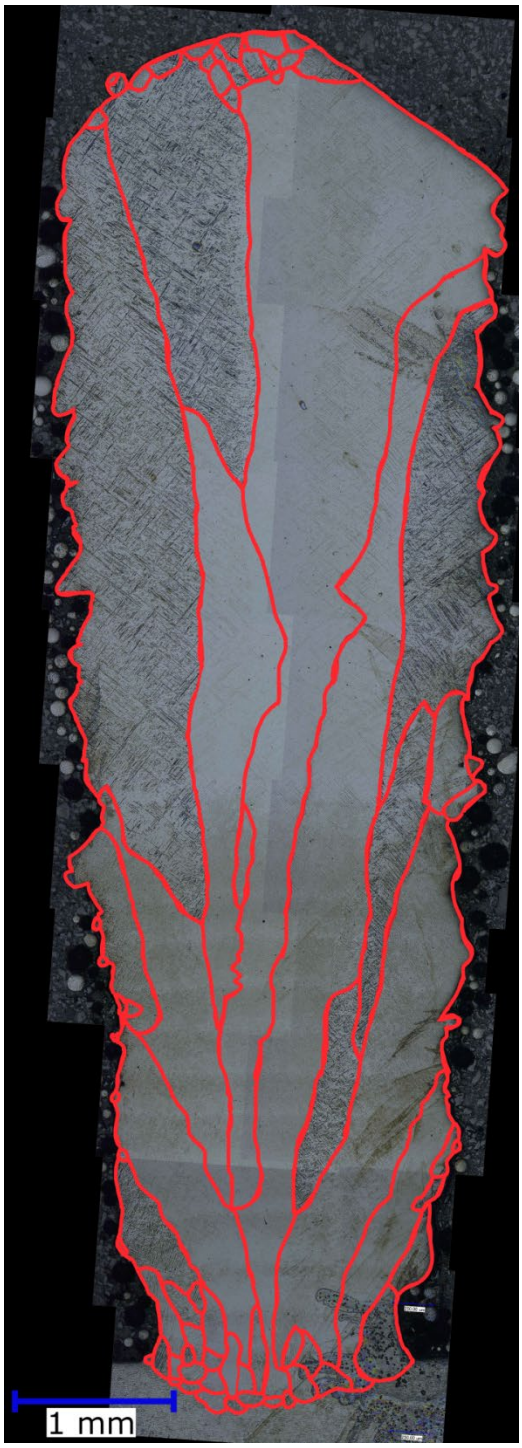


Figure 3.5: A thin wall sample with the β grains traced

Table 3.3 shows the β grain data for the middle portion of the thin walled structures. The middle zone had even greater variability than the bottom zone.

| Incident Energy (kJ/m) | Power (Watts) | Velocity (inches per minute) | Feed Rate (grams per minute) | Number of Grains | Mean Width (microns) | Standard Deviation (microns) | 95% Confidence Interval (microns) |
|---|---|---|---|---|---|---|---|
| 110 | 350 | 7.5 | 0.9 | 8 | 369 | 262 | ± 182 |
| 110 | 350 | 7.5 | 0.9 | 5 | 588 | 523 | ± 459 |
| 110 | 350 | 7.5 | 3 | 6 | 564 | 421 | ± 337 |
| 65 | 400 | 16.4 | 2 | 2 | 1275 | 660 | ± 915 |
| 65 | 400 | 16.4 | 3 | 8 | 353 | 239 | ± 166 |
| 43 | 450 | 25 | 3 | 5 | 497 | 303 | ± 265 |
| 43 | 450 | 25 | 3 | 6 | 421 | 225 | ± 180 |
| 43 | 450 | 25 | 3 | 4 | 695 | 478 | ± 469 |
| Average | | | | 5.5 | 595 | 389 | ± 371 |

**Table 3.3: Incident energy, power, velocity, feed rate and β grain size for the middle zone of the thin wall samples**

The mean number of β grains at the middle height for the thin wall samples was 5.5, whereas the mean number of β grains for the bottom was 7. Because the middle height level had fewer grains, the effects of small sample sizes on standard deviations and confidence intervals are even more pronounced.

Cooling rates are higher towards the bottom of the sample because the substrate acts as a heat sink. If the steady state Rosenthal solution for a moving point heat source on an infinite half-space is assumed to be valid, then heat must be conducted out in order to satisfy the constant temperature boundary condition as the melt pool approaches the bottom surface [110]. Because β grain size is determined by cooling rate at the liquidus temperature, higher cooling rates will result in smaller β grains [33]. The mean β grain width at the bottom of these thin wall samples is smaller than at the middle and top (362 µm vs. 595 µm and 606 µm respectively).

In 2009, Kuchi developed thermal finite element models for thin wall laser deposited Ti-6Al-4V [110]. It was found that decreased sample height resulted in increased dimensionless

cooling rate and increased thermal gradient. This could serve as an explanation for the "blooming" prior β grains seen in the thin wall samples in this work.

It has been reported that partially remelted equiaxed grains towards the bottom of a multi-layer sample can act as nuclei for columnar grains, possibly encouraging the blooming microstructure seen here. But later research found that process parameters changed grain morphology development [111].

In 2010, Davis found that as a free-edge is approached in the LENS$^{TM}$ process, large columnar grains are expected. Solidification rates and thermal gradients decrease near free-edges, which results in larger grains [31].

Figure 3.6 shows the mean β grain width versus incident beam energy for the middle portion of the thin walled structures. It is difficult to make conclusions about trends in grain size with incident energy for this region of this part geometry.

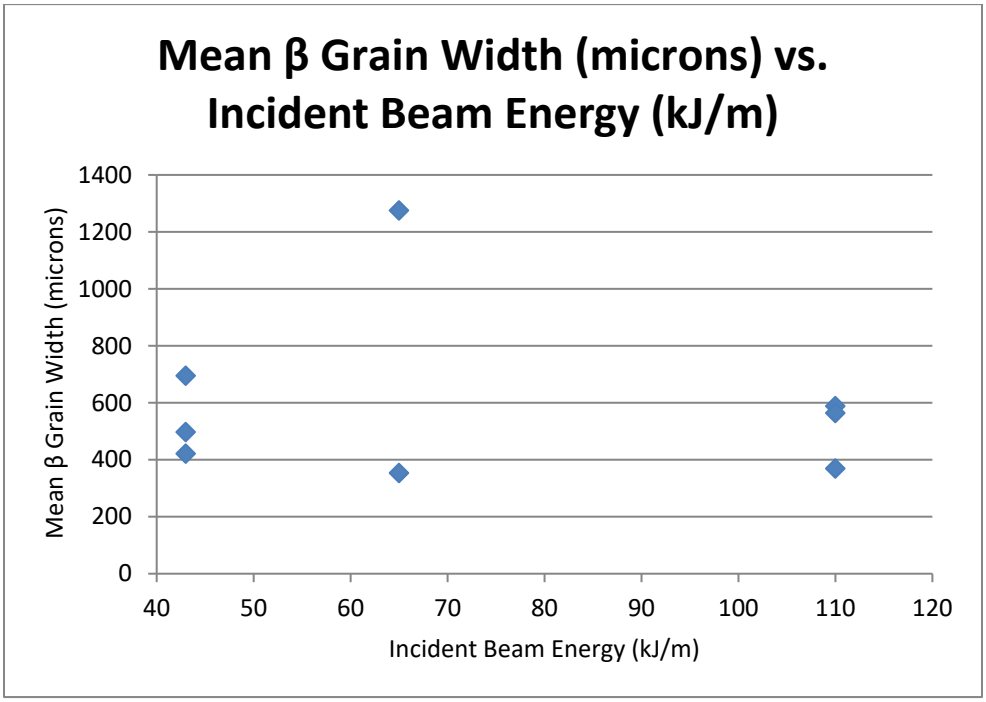


**Figure 3.6: Mean β grain width vs. incident beam energy for the middle portion of the thin walled structures**

Table 3.4 shows the β grain data for the top portion of the thin walled structures.

| Incident Energy (kJ/m) | Power (Watts) | Velocity (inches per minute) | Feed Rate (grams per minute) | Number of Grains | Mean Width (microns) | Standard Deviation (microns) | 95% Confidence Interval (microns) |
|---|---|---|---|---|---|---|---|
| 110 | 350 | 7.5 | 0.9 | 9 | 380 | 277 | ± 181 |
| 110 | 350 | 7.5 | 0.9 | 4 | 778 | 303 | ± 297 |
| 110 | 350 | 7.5 | 3 | 10 | 289 | 156 | ± 289 |
| 65 | 400 | 16.4 | 2 | 4 | 790 | 357 | ± 350 |
| 65 | 400 | 16.4 | 3 | 9 | 348 | 195 | ± 127 |
| 43 | 450 | 25 | 3 | 3 | 884 | 529 | ± 599 |
| 43 | 450 | 25 | 3 | 4 | 686 | 322 | ± 316 |
| 43 | 450 | 25 | 3 | 4 | 695 | 478 | ± 469 |
| Average | | | | 6 | 606 | 327 | ± 304 |

**Table 3.4: Incident energy, power, velocity, feed rate and β grain size for the top portion of the thin wall samples**

The mean β grain width for the top portion is similar to that of the middle. The variability in β grain size at the top of the thin wall samples is similar to that of the middle portion of the thin walled samples.

### 3.1.3 For Multi-layer pads

Table 3.5 shows the data for the bottom third of the multi-layer pads.

| Incident Energy (kJ/m) | Power (Watts) | Velocity (inches per minute) | Feed Rate (grams per minute) | Number of Grains | Mean Width (microns) | Standard Deviation (microns) | 95% Confidence Interval (microns) |
|---|---|---|---|---|---|---|---|
| 110 | 350 | 7.5 | 0.9 | 23 | 213 | 138 | ± 57 |
| 110 | 350 | 7.5 | 0.9 | 12 | 450 | 178 | ± 100 |
| 65 | 400 | 16.4 | 2 | 33 | 145 | 54 | ± 18 |
| 65 | 400 | 16.4 | 2 | 23 | 205 | 96 | ± 39 |
| 43 | 450 | 25 | 3 | 33 | 146 | 85 | ± 29 |
| 43 | 450 | 25 | 3 | 22 | 241 | 159 | ± 66 |
| Average | | | | 24 | 233 | 118 | ± 52 |

**Table 3.5: Incident energy, power, velocity, feed rate and β grain size for the bottom portion of the multi-layer pads**

The bottom of the multilayer pad samples was found to have much less variability than the thin wall samples. This is probably because there are more grains to measure, reducing the issue with sample sizes and standard deviations. Also, the β grains for the multilayer pads were measured in the middle third of the sample, so free-edge effects do not come into play. Again, the bottom samples have the smallest β grain widths. This is probably because the substrate acts as a heat sink, increasing the cooling rate for the bottom layers of the sample. It is difficult to draw conclusions purely based on grain size vs. incident energy for this set of samples because different feed rates were used. Table 3.6 shows the data for the middle zone of the multilayer pad samples.

| Incident Energy (kJ/m) | Power (Watts) | Velocity (inches per minute) | Feed Rate (grams per minute) | Number of Grains | Mean Width (microns) | Standard Deviation (microns) | 95% Confidence Interval (microns) |
|---|---|---|---|---|---|---|---|
| 110 | 350 | 7.5 | 0.9 | 16 | 303 | 159 | ± 78 |
| 110 | 350 | 7.5 | 0.9 | 9 | 641 | 385 | ± 252 |
| 65 | 400 | 16.4 | 2 | 21 | 239 | 170 | ± 73 |
| 65 | 400 | 16.4 | 2 | 15 | 323 | 227 | ± 115 |
| 43 | 450 | 25 | 3 | 17 | 285 | 205 | ± 98 |
| 43 | 450 | 25 | 3 | 12 | 424 | 273 | ± 155 |
| Average | | | | 15 | 367 | 236 | ± 128 |

**Table 3.6: Incident energy, power, velocity, feed rate and β grain size for the middle portion of the multilayer pad samples**

The middle zone had higher variability in β grain widths than the bottom of the sample. The average standard deviation was double that of the bottom portion of the multilayer pad samples. The average 95% confidence interval was more than double that of the bottom section. The bottom section of the multilayer pads has an average of 24 β grains per sample measured and the middle section has an average of 15 β grains per sample measured. This difference in sample size

could contribute to some of the difference in standard deviations and confidence intervals. Table 3.7 shows the data for the top zone of the multilayer pads.

| Incident Energy (kJ/m) | Power (Watts) | Velocity (inches per minute) | Feed Rate (grams per minute) | Number of grains | Mean Width (microns) | Standard Deviation (microns) | 95% Confidence Interval (microns) |
|---|---|---|---|---|---|---|---|
| 110 | 350 | 7.5 | 0.9 | 11 | 428 | 224 | ± 133 |
| 110 | 350 | 7.5 | 0.9 | 13 | 421 | 283 | ± 154 |
| 65 | 400 | 16.4 | 2 | 16 | 330 | 223 | ± 109 |
| 65 | 400 | 16.4 | 2 | 17 | 300 | 289 | ± 138 |
| 43 | 450 | 25 | 3 | 17 | 305 | 206 | ± 98 |
| 43 | 450 | 25 | 3 | 20 | 246 | 163 | ± 71 |
| Average | | | | 16 | 338 | 231 | ± 117 |

**Table 3.7: Incident energy, power, velocity, feed rate and β grain size for the top zone of the multilayer pads**

In general, β grain widths increase as height up the sample increases. Variability in β grain size is lowest in the bottom portion of the samples. Multilayer pads have lower variability in β grain structure than thin walls. This is probably in part because they have more β grains at each height.

### 3.1.4 Comparison of β Grain Widths across Geometries

Mean β grain widths were compared across single layer pad, thin wall and multi-layer pad geometries for two sets of process parameters. The comparison is shown in Figure 3.7. The sets of process parameters were a power of 400 W with a velocity of 16.4 ipm and a feed rate of 2 gpm, and a power of 450 W with a velocity of 25 ipm and a feed rate of 3 gpm. Those sets of parameters were chosen because they were the sets that had the most samples to compare across geometries; single layer pads, thin walls and multi-layer pads were characterized for both sets.

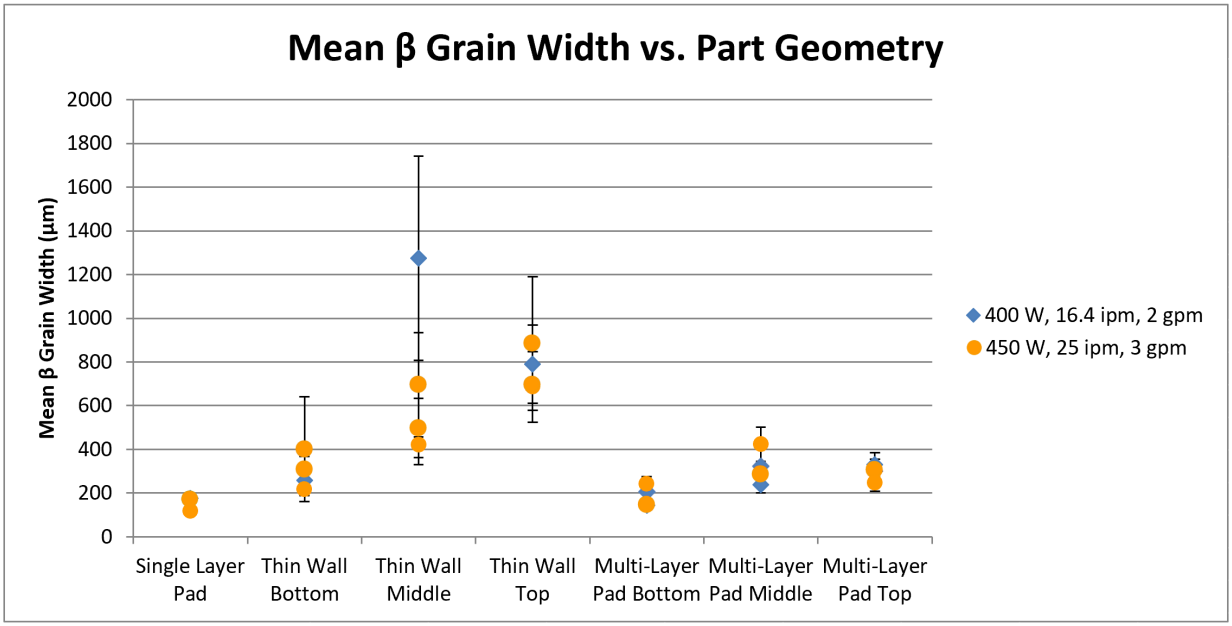


**Figure 3.7: Mean β grain width vs. part geometry for two sets of process parameters**

There are no error bars for the single layer pad samples. This is because there were not enough measurements taken for the calculation of error bars. For both sets of samples, thin walls had the largest mean β grain widths. This could be because of the decrease in cooling rates and thermal gradients as a free edge is approached [31]. Those factors cause larger β grains to form. The measurements for the single and multilayer pads were made in the middle third of the samples, so the effect of approaching an edge would not have played any part in those β grain measurements. For the 450 W power, 25 ipm velocity and 3 gpm feed rate case, mean β grain widths are highest at the top of the thin wall sample. This is in line with Kuchi's models [110].

## 3.2 α-Lath Results for Single Layer Pads

α-lath measurements for single layer pads were taken using scanning electron microscopy with backscatter detection and FoveaPro. Table shows the α-lath measurements for the single layer pads.

| Incident Energy (kJ/m) | Power (watts) | Velocity (ipm) | Lath Thickness (microns) | Feed Rate (gpm) |
|---|---|---|---|---|
| 24 | 250 | 25 | 0.623 | Scaled Feed |
| 24 | 250 | 25 | 0.614 | Scaled Feed |
| 110 | 350 | 7.5 | 0.621 | 0 (Laser Glaze) |
| 110 | 350 | 7.5 | 0.609 | 3 |
| 142 | 450 | 7.5 | 0.600 | Scaled Feed |

**Table 3.8: Incident energy, power, velocity, α-lath thickness and feed rate for the single layer pads**

A "scaled feed" rate means that the powder feed rate was scaled with the anticipated melt rate. Similar α-lath thicknesses were measured across powers and velocities. It was found that increasing β width does not necessarily increase α thickness, at least for single layer pads.

## 3.3 Structural components

### 3.3.1 α results for structural components

α-lath measurements for structural component geometries were taken [49]. Images were taken using scanning electron microscopy with backscatter detection, and electron back scatter detection. The images were analyzed using MIPAR$^{TM}$ software. Table 3.9 shows the α-lath widths and 95% confidence intervals. Figure 3.8 shows the zone designations.

| | Zone | α-Lath Width (microns) | 95% Confidence Interval | # Images |
|---|---|---|---|---|
| **0s Dwell 1-Bead Leg** | 1 | 0.55 | n/a | 1 |
| | 2 | 0.58 | 0.14 | 5 |
| | 3 | 0.69 | 0.03 | 5 |
| | 4 | 0.67 | 0.26 | 2 |
| | 5 | 0.59 | n/a | 1 |
| **0s Dwell 3-Bead Leg** | 1 | 0.54 | n/a | 1 |
| | 2 | 0.94 | 0.10 | 5 |
| | 3 | 0.92 | 0.06 | 5 |
| | 4 | 1.00 | 0.14 | 5 |
| | 5 | 0.58 | n/a | 1 |
| **4s Dwell 1-Bead Leg** | 1 | 0.32 | n/a | 1 |
| | 2 | 0.35 | 0.07 | 4 |
| | 3 | 0.41 | 0.06 | 5 |
| | 4 | 0.30 | 0.02 | 5 |
| | 5 | 0.53 | n/a | 1 |
| **4s Dwell 3-Bead Leg** | 1 | 0.50 | n/a | 1 |
| | 2 | 0.68 | 0.12 | 5 |
| | 3 | 0.66 | 0.16 | 5 |
| | 4 | 0.77 | 0.13 | 5 |
| | 5 | 0.58 | n/a | 1 |

Table 3.9: α-lath widths and confidence intervals for the structural component samples [49]

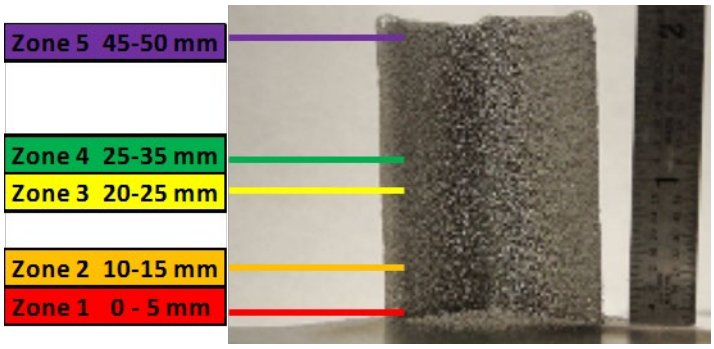


Figure 3.8: Zone designations for the structural component geometries [49]

### 3.3.2 Hardness measurements and hardness maps

Vickers hardness testing was performed on the samples. The 3-bead leg samples were tested using automatic hardness testing equipment. Spacing for the automatic hardness tests was 500 microns. Maps were made for the top, bottom, and middle portions of the samples, then stitched together. The 1-bead leg samples were tested manually. The 1-bead samples had smaller horizontal spacing than the automatically tested samples, but larger vertical (z-height) spacing. Figure 3.9 shows a comparison of the hardness maps. It was made using IgorPro software [112]. Table 3.10 shows the Vickers hardness across the structural component samples. It also shows maximum hardness, minimum hardness, mean hardness and standard deviation for the samples.

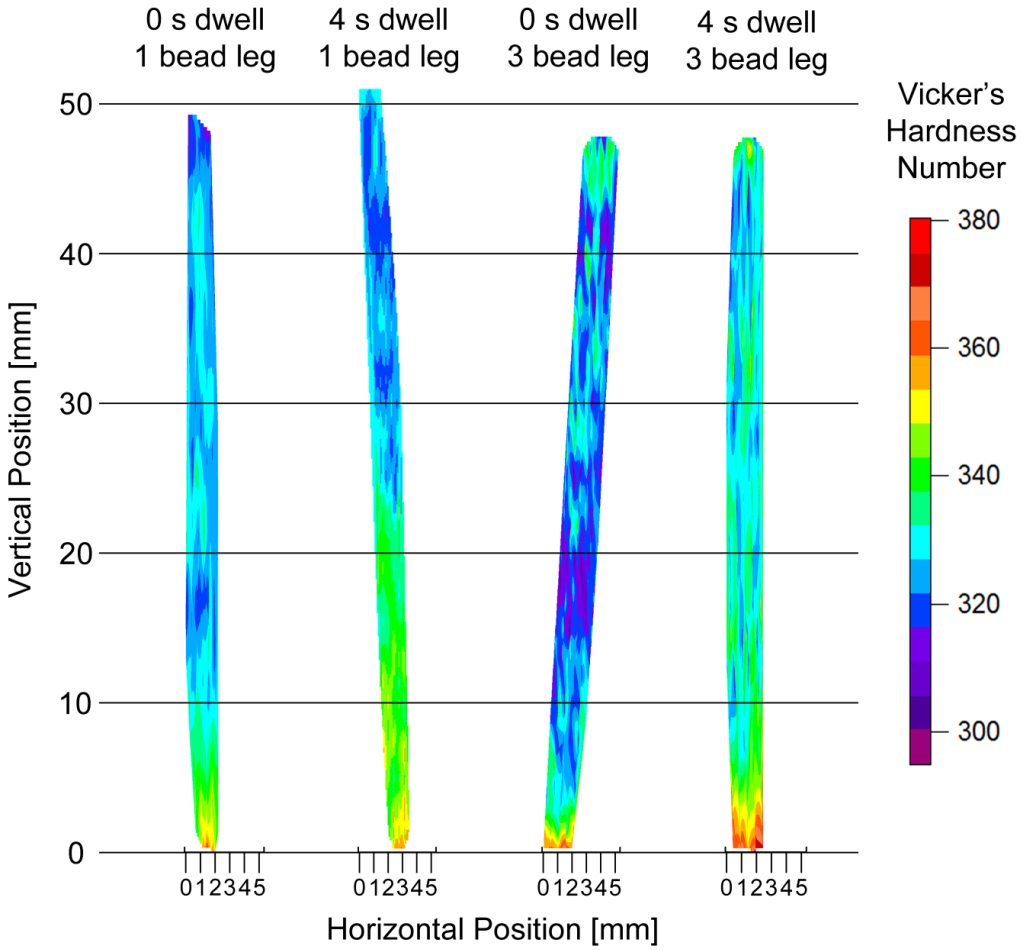


Figure 3.9: Comparison of Vickers hardness maps

| Number of Beads per Layer | Dwell Time [s] | Maximum Hardness [HV] | Minimum Hardness [HV] | Mean Hardness [HV] | Standard Deviation [HV] |
|---|---|---|---|---|---|
| 1 | 0 | 369 | 308 | 330 | 11.4 |
| 1 | 4 | 364 | 307 | 332 | 11.8 |
| 3 | 0 | 374 | 296 | 343 | 13.4 |
| 3 | 4 | 378 | 296 | 333 | 13.5 |

**Table 3.10: Vickers hardness measurements across structural component samples**

Approximately 200 hardness measurements were taken for the 0 second dwell 1-bead sample. The minimum hardness was found approximately 95% of the way up the sample. The 4 second dwell, 1-bead sample also had approximately 200 hardness measurements taken. The minimum hardness was found approximately 90% of the way up the sample.

Approximately 550 hardness measurements were taken for the 0 second dwell, 3-bead leg sample. The minimum hardness was found approximately 80% of the way up the sample. For the 4 second dwell, 3-bead leg sample, approximately 500 hardness measurements were taken. The minimum hardness was found approximately 95% of the way up the sample. The maximum hardness measurements for all four samples were found near the bottom.

Overall, the 1-bead leg samples had smaller standard deviations for their hardness measurements. The 3-bead leg samples had higher average hardness values, but also had lower minimum hardness values than the 1-bead leg samples. The hardness maps indicate that hardness vs. height is periodic at steady state.

Hardness depends heavily on α morphology [105]. Figure 3.10 shows a plot of Vickers hardness values vs. α-lath widths for the structural component samples. Linear regressions were calculated and the trendlines are shown on the plot. It can be seen that Vickers hardness decreases as α-lath width increases. This is as expected, because the α effect dictates that larger α-lath widths are associated with lower hardness values.

The Hall-Petch equation for yield strength was discussed in the first chapter of this thesis. It is worth mentioning that the relationship between grain size and Vickers hardness can be expressed in a similar form

$$H = H_0 + k_h d^{-\frac{1}{2}}; \tag{4}$$

Where $H$ is the Vickers hardness, $d$ is grain size, $H_0$ is the hardness intercept at $d^{-1/2} = 0$, and $k_h$ is the Hall-Petch slope [113]. Figure 3.11 shows a Hall-Petch hardness plot for the structural component samples. To make a Hall-Petch plot, the inverse of the square root of the grain size is plotted on the x-axis and either yield strength or hardness is plotted on the y-axis.

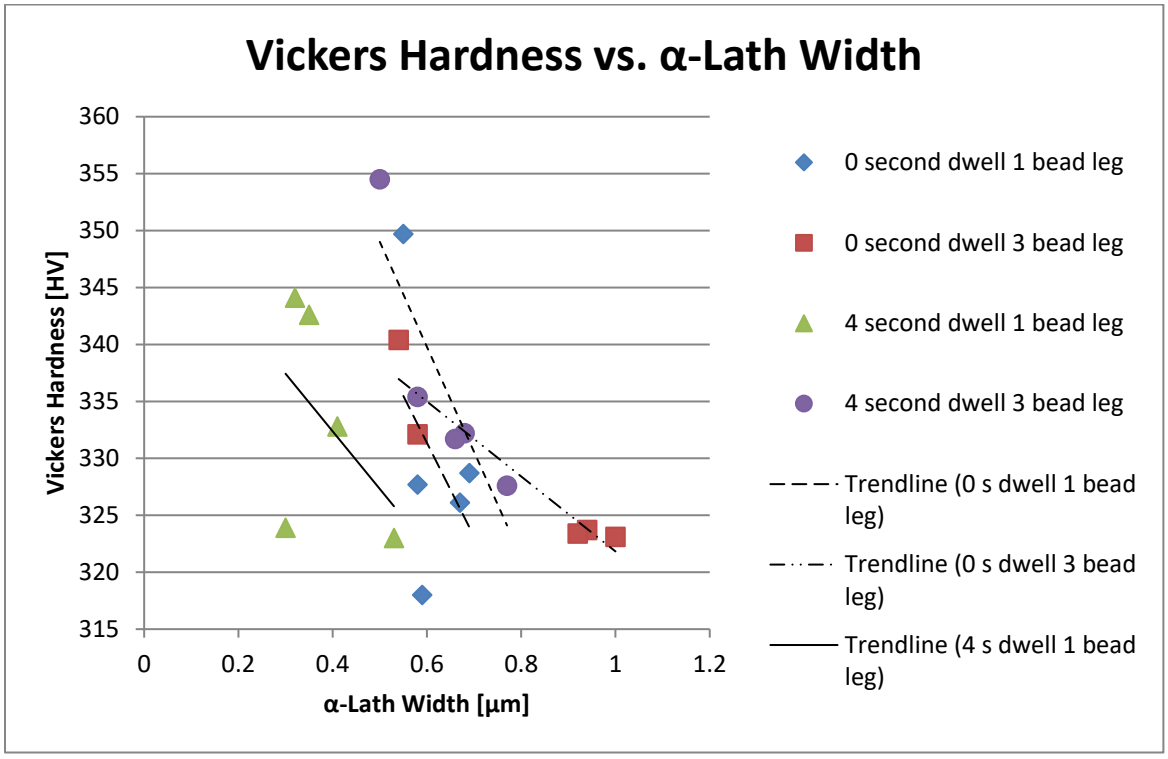


Figure 3.10: Vickers hardness vs. α-lath widths for the structural component samples

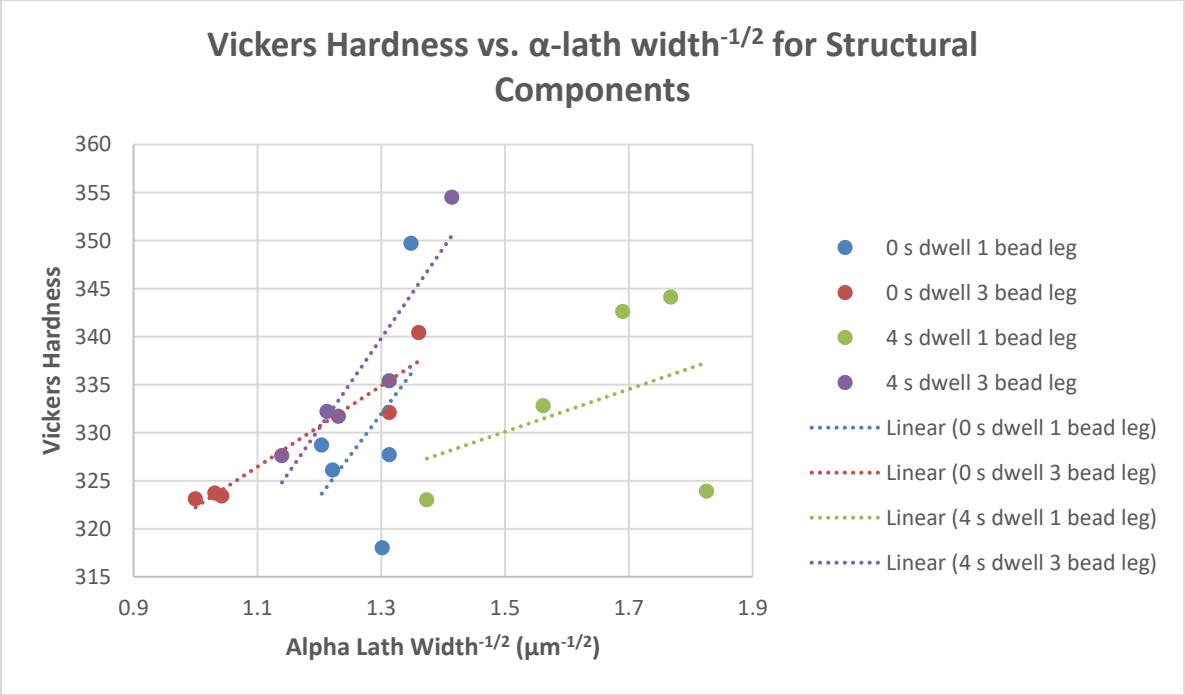


**Figure 3.11: A Hall-Petch hardness plot for the structural component samples**

Mean thermal data collected during the build was compared to Vickers hardness measurements for the 0 second dwell sample as shown in Table 3.11.

| | Thermal Gradient (K/cm) | | | Vickers Hardness (units) | | |
|---|---|---|---|---|---|---|
| Build Location | Mean | Standard Deviation | Sample Size | Mean | Standard Deviation | Sample Size |
| Lower 10% of 1-bead leg | 6047 | 1101 | 99 | 349.7 | 9.3 | 29 |
| Upper 90% of 1-bead leg | 5112 | 1206 | 853 | 326.8 | 7.9 | 174 |
| Lower 10% of 3-bead leg | 6177 | 2999 | 576 | 340.4 | 15.6 | 50 |
| Upper 90% of 3-bead leg | 6469 | 3653 | 4686 | 323.0 | 12.0 | 491 |
| 1-bead leg (100% average) | 5209 | 1229 | 952 | 330.1 | 11.4 | 203 |
| 3-bead leg (100% average) | 6437 | 3588 | 5262 | 324.6 | 13.4 | 541 |

**Table 3.11: Thermal data compared to Vickers hardness for the 0 second dwell structural component sample [101]**

A higher thermal gradient was associated with a higher mean Vickers Hardness for the 1-bead leg of the part but a higher thermal gradient was association with a lower Vickers Hardness for the 3-bead leg of the part.

Cooling rates are not the only thing that comes into play when determining microstructures and hardnesses. High $G/R$ yields columnar grains and low $G/R$ yields equiaxed/mixed grains, where $R$ is the ratio between cooling rate and gradient of temperature and $G$ is the thermal gradient at the interface solidus-liquidus [23] [111]. The Hall-Petch effect dictates that larger grains have lower hardnesses, so anything that makes the grains bigger will have that effect.

Mean thermal gradient for the entirety of the 1-bead leg was found to be lower than the mean thermal gradient for the 3-bead leg. Mean Vickers hardness was found to be higher for the 1-bead leg of the 0 second dwell sample than for the 3-bead leg. Mean thermal data was compared to mean hardness data for the 4 second dwell sample as shown in Table 3.12.

| | Thermal Gradient (K/cm) | | | Vickers Hardness (units) | | |
|---|---|---|---|---|---|---|
| Build Location | Mean | Standard Deviation | Sample Size | Mean | Standard Deviation | Sample Size |
| Lower 10% of 1-bead leg | 7061 | 2643 | 113 | 346.8 | 10.5 | 21 |
| Upper 90% of 1-bead leg | 6630 | 2931 | 664 | 330.1 | 10.7 | 181 |
| Lower 10% of 3-bead leg | 6925 | 2205 | 497 | 354.5 | 12.6 | 50 |
| Upper 90% of 3-bead leg | 6893 | 2394 | 3110 | 330.2 | 11.2 | 441 |
| 1-bead leg (100% average) | 6692 | 2893 | 777 | 331.9 | 11.8 | 202 |
| 3-bead leg (100% average) | 6897 | 2369 | 3607 | 332.7 | 13.5 | 491 |

**Table 3.12: Thermal data compared to Vickers hardness for the 4 second dwell structural component sample [101]**

A higher mean thermal gradient was associated with a higher mean Vickers hardness for the 1-bead leg sample. A higher mean thermal gradient was also associated with a higher mean Vickers hardness for the 3-bead leg of the 4 second dwell sample.

Mean thermal gradient for the entirety of the 1-bead leg was found to be lower than the mean thermal gradient for the 3-bead leg. Mean Vickers Hardness for the 1-bead leg of the 4 second dwell sample was found to be slightly lower than the Vickers Hardness of the 3-bead leg.

## 3.4 Discussion of layering effect

The samples were polished then etched using Kroll's reagent. Dark and light bands were seen when the samples were observed using polarized light microscopy. Figure 3.12 shows the banding at three different heights on the 4 second dwell 1-bead leg sample.

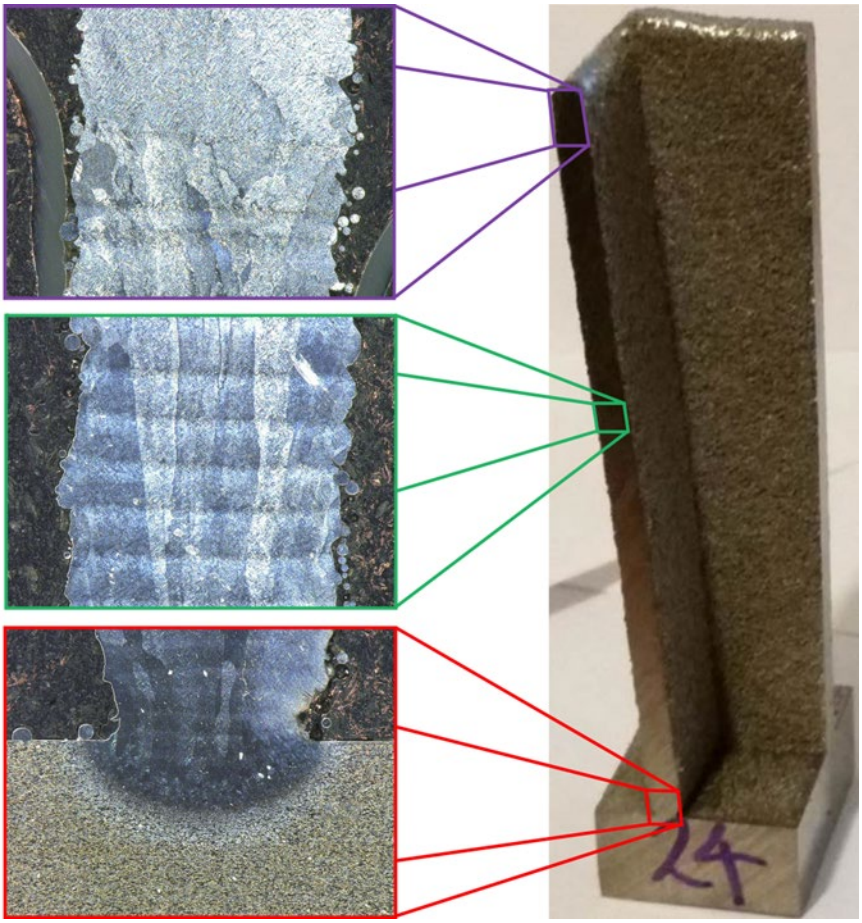


Figure 3.12: The layering effect

The bands were not visible at the top of the sample. They were also not visible under scanning electron microscopy using either secondary electron detection (SE) or backscatter electron detection (BSE). The dark and light bands could not be seen with electron backscatter diffraction (EBSD).

Curved light and dark banding was also seen towards the edges of the multi-layer pad samples, as shown in Figure 3.13. The sample shown was made using a beam power of 350 W, a velocity of 7.5 ipm and a feed rate of 0.9 gpm.

**Figure 3.13: Light and dark banding in a multi-layer pad sample**

The author refers to one cycle of a light band combined with a dark band as a "Heat Affected Layer" (HAL), because it is possible that they are a product of the thermal cycling involved in additive manufacturing.

Leicht and Wennberg noted a similar dark and light banding effect in SLM and EBM Ti-6Al-4V samples in 2015 [50]. It was postulated that a change in the melt path of the beam between layer depositions could cause layers to etch differently. It was reported that the bands were more visible in SLM samples than EBM samples.

This work focused on the HALs in the 1-bead legs of the structural component samples. The thickness of the HALs was measured using ImageJ. Figure 3.14 shows the HALs being measured in ImageJ. Five measurements were taken per band. The mean thickness for a single dark or light band was found to be 180.8 µm. This is similar to the reported deposition layer thickness of 180 µm.

The HAL thickness was compared to the height above the substrate. The height for each layer was measured from the bottom of the substrate up to the layer in question rather than taking the sum of the thicknesses of the layers, in order to reduce error propagation.

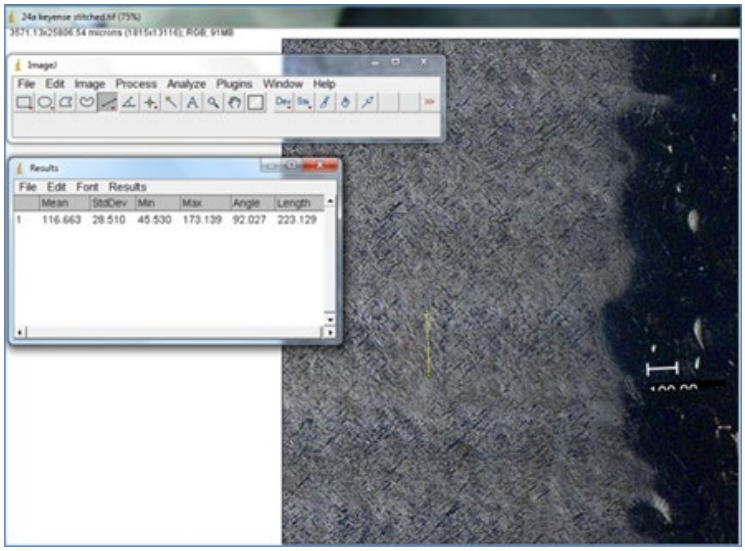


**Figure 3.14: Measuring heat affected layers in ImageJ**

Figure 3.15 shows the HAL thickness vs. the height above the substrate for the 0 second dwell 1-bead leg sample. The thinnest layers were found towards the bottom.

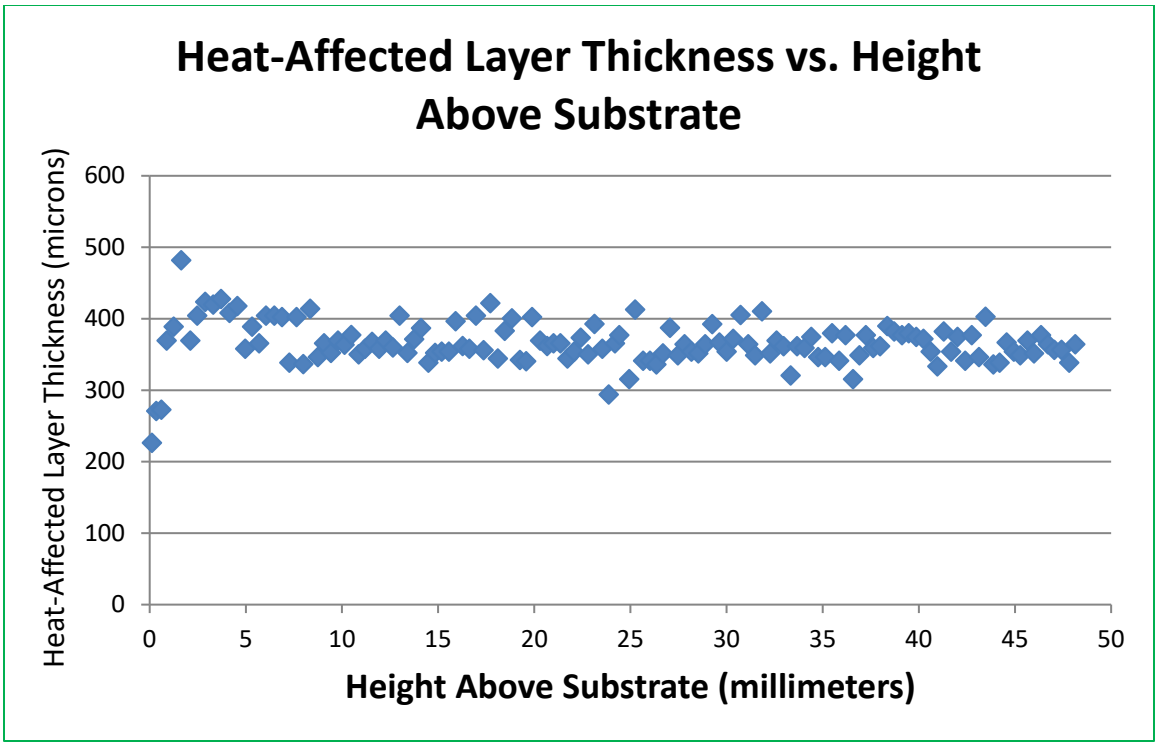


**Figure 3.15: Heat-Affected Layer Thickness vs. height above substrate for the 0s dwell 1-bead leg sample**

Regressions were calculated for the HAL thickness vs. the height above the substrate. No regression with a suitably low r-squared value was able to be calculated. This means that the data did not follow a trend that is linear, or periodic. The measurements of HAL thickness in the chart are for the thickness of a dark and light layer combined. The values staying close to 360 µm is what would be expected for two deposition layers.

Figure 3.16 shows the HAL thickness vs. the height above the substrate for the 4 second dwell 1-bead leg sample.

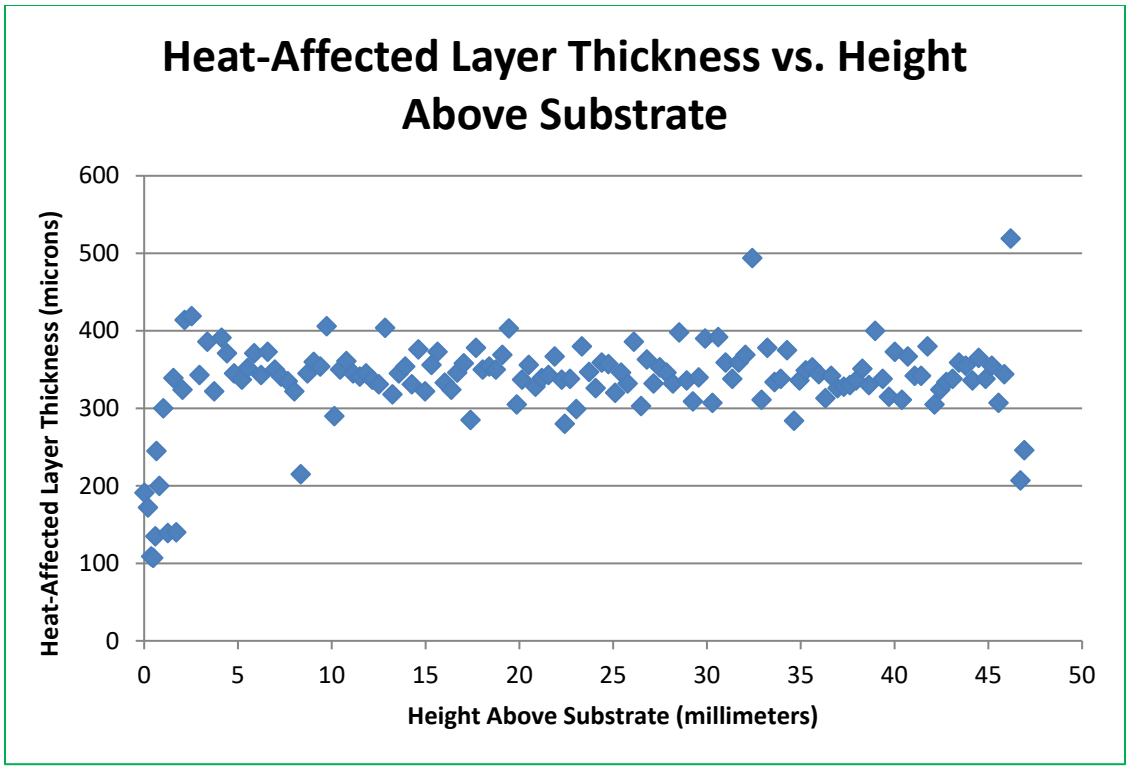


Figure 3.16: Heat affected layer thickness vs. height above the substrate for the 1-bead leg of the 4s dwell sample

Regression analysis was conducted and like the data for the 0 second dwell 1-bead leg sample, no suitable regression could be found. Reported HAL thickness is for a dark and light layer combined.

Mean Vickers hardness was compared to HAL thickness for the 0 second dwell 1-bead leg sample, as shown in Figure 3.17. There appears to be no correlation between Vickers hardness and HAL thickness for the sample.

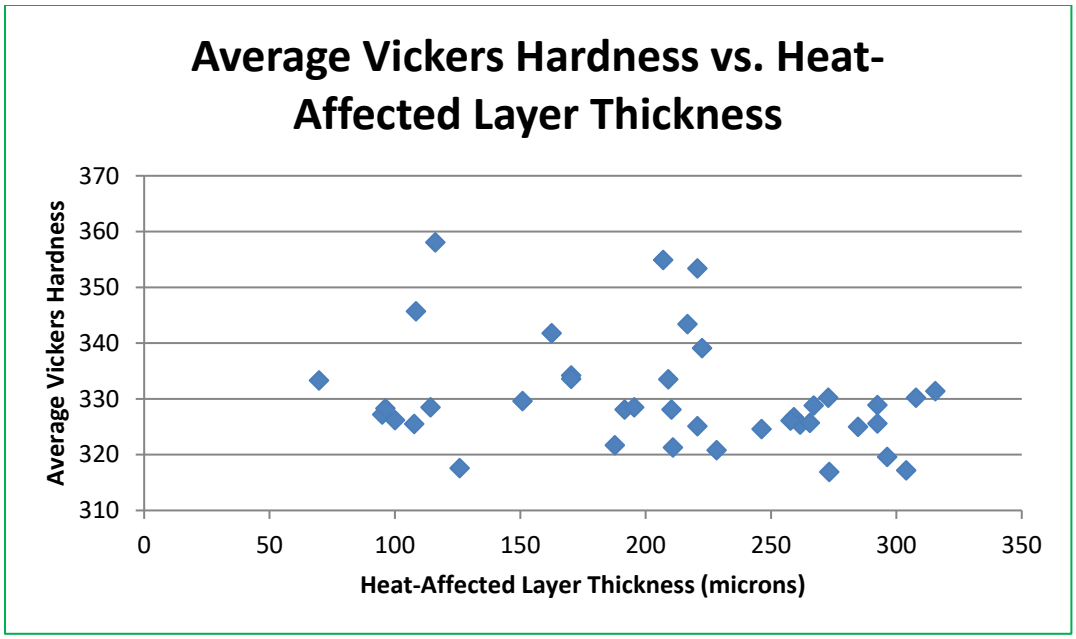


Figure 3.17: Vickers hardness vs. heat affected layer thickness for the 1-bead leg of the 0 second dwell sample

Average Vickers hardness was compared to HAL thickness for the 4 second dwell 1-bead leg sample as shown in Figure 3.18. There appears to be no correlation between Vickers hardness and HAL thickness for the sample.

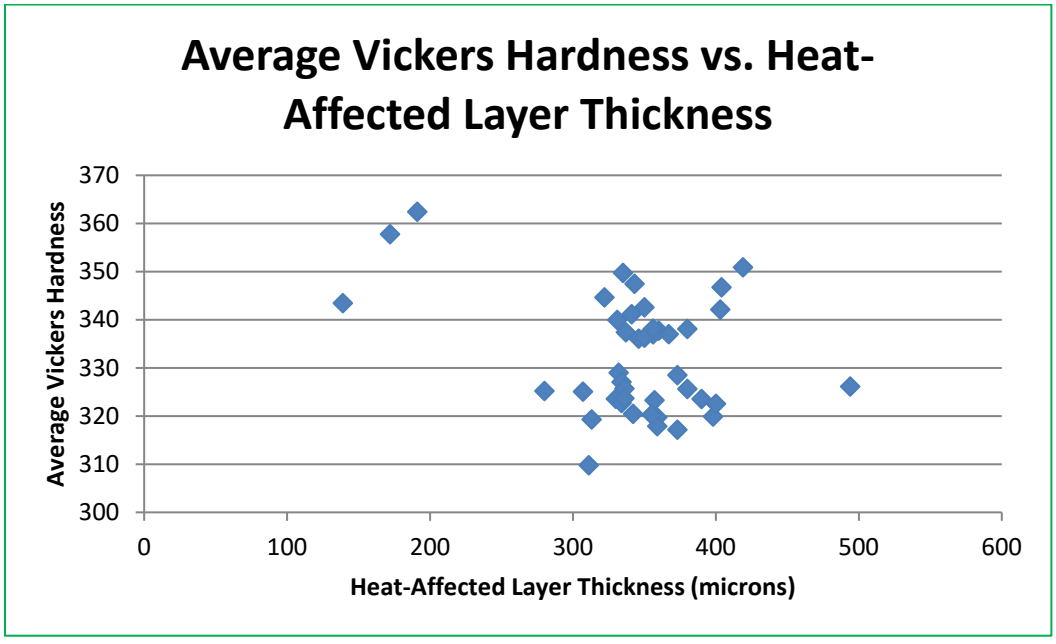


Figure 3.18: Vickers hardness vs heat affected layer thickness for the 1-bead leg of the 4 second dwell sample

No connection was found between Vickers hardness and HAL thickness for either sample.

Hardness measurements were taken in the dark and light bands for the 0 second dwell 1-bead leg sample. Figure 3.19 illustrates where the hardness indents were made relative to the banding [114]. Table 3.13 summarizes the results of the hardness measurements.

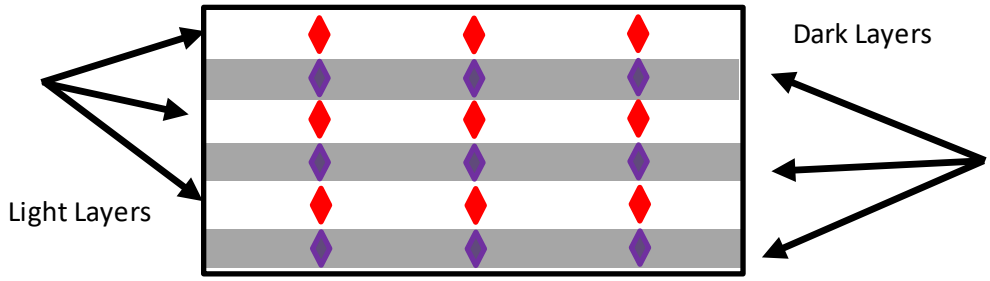


**Figure 3.19: The placement of hardness indents with respect to dark and light bands for the 0 second dwell 1-bead leg sample**

| | Left (HV) | Middle (HV) | Right (HV) | Average (HV) | Std Dev (HV) |
|---|---|---|---|---|---|
| Light | 300.2 | 298.2 | 301.5 | 299.97 | 1.66 |
| Dark | 293 | 297 | 297.7 | 295.90 | 2.54 |
| Light | 307 | 303.1 | 309.3 | 306.47 | 3.13 |
| Dark | 299.7 | 294.6 | 291.3 | 295.20 | 4.23 |
| Light | 305 | 305.6 | 306.5 | 305.70 | 0.75 |
| Dark | 299.4 | 304 | 292.2 | 298.53 | 5.95 |

**Table 3.13: Vickers hardness across heat-affected layers**

A one-way analysis of variance (ANOVA) between data sets was conducted to compare the effect of band color on Vickers hardness in the light-colored bands and dark colored bands in the 0 second dwell 1-bead leg sample. There was a statistically significant effect of band color on Vickers hardness at the $p < 0.05$ level for the two conditions [$F(1,16)=16.9$, $p=0.0008$]. In other words, the probability of the difference in hardness between data sets being due to random chance is less than 0.1%. This suggests that whatever mechanism causes the observed coloration bands may also affect Vickers hardness.

However, it should be noted that all of the standard deviations reported are less than 2% of the Vickers hardness measurement. Vickers hardness measurements are subject to error of approximately 1-2% [115]. Barbato and Desogus examined ISO and ASTM standards for Vickers microhardness equipment and found that the strictest standards for measuring hardness indents require an accuracy limit of 0.5 μm for the stage micrometer [116]. They stress that most Vickers hardness measurements have more error than that.

The type of microscope used to observe the indents can also introduce error [116]. The hardness indents measured in this work had diagonals between 50 and 60 μm. Error in measuring the indents on the order of 0.5 μm could introduce a difference of ±1% in the measurements. A stereoscopic microscope was used to observe the hardness indents for the 1-bead leg samples in this work. Boundary lines for hardness indents are not always readily visible, and optical microscopy can produce a "shadow" that distorts the view of the hardness indent edges [116]. Using a lower load when performing microhardness testing allows for smaller indents that fit within individual dark or light bands. Experimental research on the Rockwell Hardness test, which also uses a diamond pyramid indenter, found that the tradeoff is that percent error for manually measured hardness indents increases as the size of the indent decreases [117].

There is a possibility that more oxygen precipitates into the lighter bands [118]. The LENS™ setup in which the sample was manufactured had most of the air purged and replaced with Argon, but the oxygen content was "less than 10 ppm", not zero. [101]

Energy dispersive spectroscopy (EDS) was used to check the chemical composition up the length of the sample. Zinin provides an overview of EDS and Wavelength Dispersive Spectroscopy (WDS) for electron microscopy and it is summarized here [119]. EDS works by energizing atoms on the surface of a sample using an electron beam. The valence electrons in the

atoms jump up an energy level, then fall back down and release energy in the form of photons, typically X-rays.

A detector attached to an SEM can use that information to determine the chemical composition of a sample. When an EDS scan is performed, a plot can be made showing the number of "counts" of detected X-rays vs. their energy. Figure 3.20 shows an example of such a plot that was made when measuring the chemical composition of the substrate of the 1-bead leg of the 0 second dwell sample.

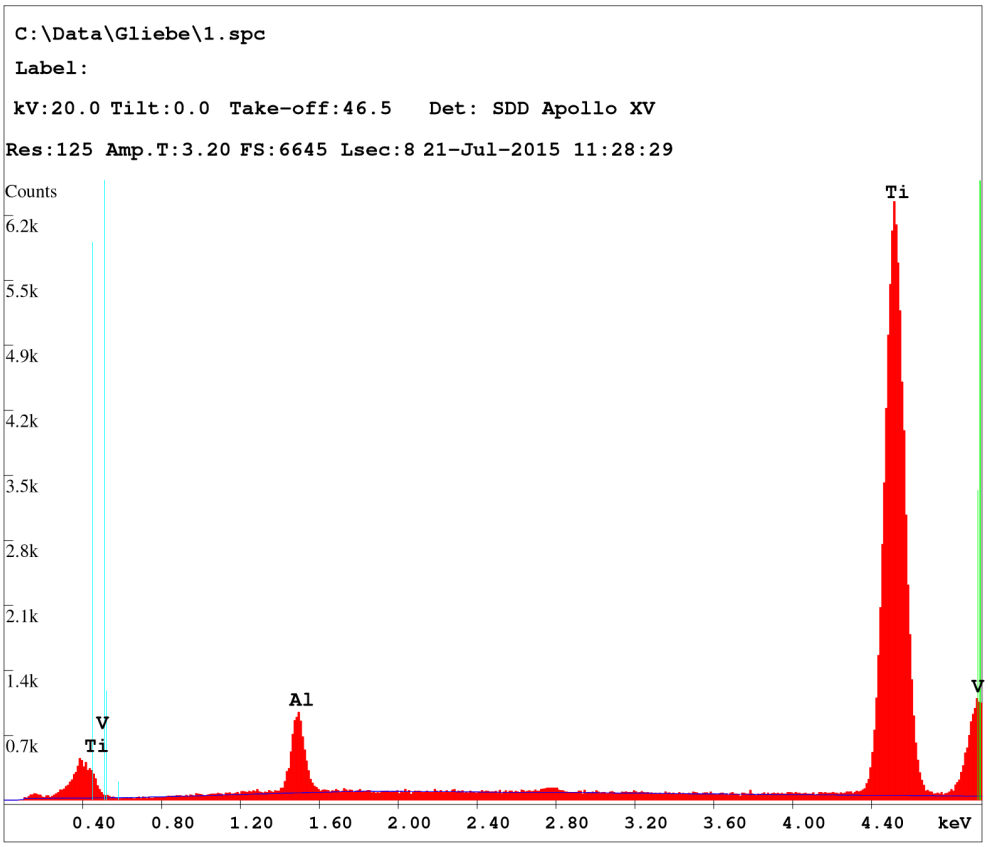


**Figure 3.20: EDS data for the substrate of the 1-bead leg of the 0 second dwell sample**

A line scan was performed. There were slight variations in aluminum and vanadium concentrations, but they could not be correlated to the layering effect. Figure 3.21 shows the weight percent of titanium, aluminum and vanadium in the 1-bead leg of the 0 second dwell sample vs. the height above the substrate. Weight percent was chosen rather than atomic percent

because the reported composition of Ti-6Al-4V is given as a weight percent. Data points that have a negative value for height were measurements of the substrate taken for comparison.

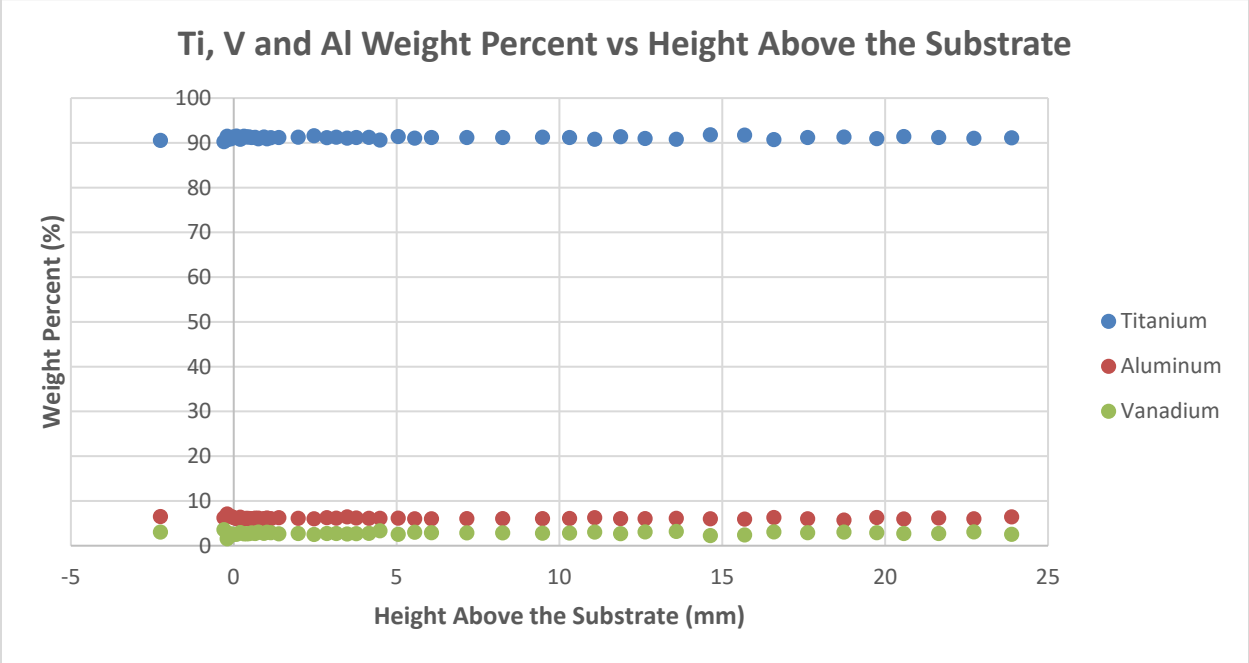


**Figure 3.2: Ti, V, and Al Weight Percent vs. Height Above the Substrate of the 1-bead leg of the 0 s dwell sample**

It is probable that the variations seen were due to the EDS scanner picking up small differences in the chemical composition of α and β. The β phase of Ti-6Al-4V tends to have higher vanadium concentrations than the α phase [120].

EDS determines the chemical composition of a sample based on the energy of the released X-rays whereas WDS determines the chemical composition based on the wavelength of the released X-rays. A WDS detector can only measure one element at a time. Most systems have multiple detectors to get around that. WDS however has higher resolution, which makes it easier to search for trace elements like oxygen in a LENS$^{TM}$ sample [119].

# 4 Summary and Conclusions

Microstructural characterization of LENS$^{TM}$ additive manufactured Ti-6Al-4V samples has been conducted. Samples manufactured using different process parameters were observed in order to facilitate process mapping.

A method for measuring β grain widths that allows for statistical calculations was outlined. The method was used to compare variability of β grain widths across part geometries. It was found that thin wall parts have the highest β width variability and that the width of the β grains varies more towards the top of multi-layered samples than towards the bottom. Mean grain widths were also compared across part geometries. Single layer pad geometries were found to have the smallest β grain widths, multi-layer pads had larger β grain widths, and thin wall samples had the largest β grain widths.

Vickers microhardness testing was conducted and hardness maps were created for tall thin walled structural component samples. Hardness values were compared to α-lath widths and thermal gradients at different heights on the sample. Optical microscopy was used to observe a layering effect in structural component samples. It was found that light and dark bands had different Vickers microhardness values.

Next steps for research in this area would include observing β grain widths using different techniques such as EBSD in addition to optical microscopy. Grains could be measured at their maximum widths rather than across a line. Grain aspect ratios could also be measured and reported in order to quantify whether a microstructure is equiaxed, columnar or mixed.

Vickers microhardness testing could be conducted across deposition geometries. Hardness values could be compared to mean β grain widths and variability in hardness could be tested

compared to the height of the sample. Making the same number of measurements up the height of the sample would ensure that sample size does not skew standard deviations or confidence intervals. An exploration of the connection between Vickers microhardness and band coloration could also be conducted using smaller loads. This would ensure that the resulting hardness indents are small enough that they are not close to the edges of the bands.

Wavelength Dispersive Spectroscopy analysis could be conducted to check for oxygen or other interstitial impurities in the different colored layer bands. Since layer banding has also been observed by other researchers in SLM and EBM Ti-6Al-4V samples, if impurities are found, differences could be compared across manufacturing processes. Multiple EDS line scans could be performed to see if there is a difference in aluminum and vanadium concentrations between light and dark bands.

The collection of α-lath data up the length of a tall thin wall geometry could be conducted. Image analysis could be achieved using the batch processing capabilities of a software like MIPAR$^{TM}$. That α-lath data could then be compared to Vickers microhardness data acquired using automated hardness testing equipment. This would allow for more information than what can be obtained by simply looking at a handful of measurement zones up the length of the sample. The α-lath data could also be compared to in-situ thermal monitoring data like that which was collected for the samples in this work.

# Works Cited


[1] W. D. Callister, Materials Science and Engineering: An Introduction, 8th ed ed., John Wiley & Sons, Inc., 2010.

[2] "3D Printing: Facts & Forecasts," Siemens, [Online]. Available: http://www.siemens.com/innovation/en/home/pictures-of-the-future/industry-and-automation/Additive-manufacturing-facts-and-forecasts.html. [Accessed 17 December 2015].

[3] Z. Doubrovski, J. C. Verlinden and J. M. Geraedts, "Optimal Design for Additive Manufacturing: Opportunities and Challenges," in *Proceedings of the ASME 2011 International Design Engineering Technical Conferences & Computers and Information in Engineering Conference*, Washington D.C., 2011.

[4] W. Carter, D. Erno, D. Abbott, C. Bruck, G. Wilson, J. Wolfe, D. Finkhousen, A. Tepper and R. Stevens, "The GE Aircraft Engine Bracket Challenge: An Experiment in Crowdsourcing for Mechanical Design Concepts," in *SFF Conference Proceedings*, Austin, 2014.

[5] Y. Luo, Z. Ji, M. C. Leu and R. Caudill, "Environmental Performance Analysis of Solid Freeform Fabrication Processes," in *Proceedings of the 1999 IEEE International Symposium on Electronics and the Environment*, Danvers, Massachusetts, 1999.

[6] S. Nimbalkar, D. Cox, K. Visconti and J. Cresko, "Life Cycle Energy Assessment Methodology and Additive Manufacturing Energy Impacts Assessment Tool," in *Proceedings from the LCA XIV International Conference*, San Francisco, 2014.

[7] Sciaky, Inc., *Electron Beam Additive Manufacturing.* Chicago, Illinois, 2017.

[8] EOS, "Additive Manufacturing, Laser-Sintering and industrial 3D printing - Benefits and Functional Principle," [Online]. Available: https://www.eos.info/additive_manufacturing/for_technology_interested.

[9] ARCAM, "EBM in Aerospace - Additive Manufacturing taken to unseen heights," [Online]. Available: http://www.arcam.com/solutions/aerospace-ebm/. [Accessed 9 March 2017].

[10] Optomec, Inc., 2017. [Online]. Available: https://www.optomec.com/. [Accessed 24 October 2018].

[11] "Electron Beam Additive Manufacturing (EBAM(R))," Sciaky Inc., 2017. [Online]. Available: http://www.sciaky.com/additive-manufacturing/electron-beam-additive-manufacturing-technology. [Accessed 2017].

[12] W. E. Frazier, "Metal Additive Manufacturing: A Review," *Journal of Materials Engineering and Performance,* pp. 1917-1928, 2014.

[13] "EBM(R) Electron Beam Melting - in the forefront of Additive Manufacturing," [Online]. Available: http://www.arcam.com/technology/electron-beam-melting/.[Accessed 2017].

[14] M. Griffith, D. Keicher, C. Atwood, J. Romero, J. Smugeresky, L. Harwell and D. Greene, "Freeform Fabrication of Metallic Components Using Laser Engineered Net Shaping (LENS TM)," in *SFF Conference Proceedings*, Austin, 1996.

[15] H. Lee, C. H. J. Lim, M. J. Low, N. Tham, V. M. Murukeshan and Y. J. Kim, "Lasers in Additive Manufacuring: A Review," *International Journal of Precision Engineering and Manufacturing- Green Technology,* pp. 307-322, July 2017.

[16] H. Canady, "Optomec Improves Additive Repair Technique," 21 October 2016. [Online]. Available: https://www.optomec.com/optomec-improves-additive-repair-technique/. [Accessed 22 October 2018].

[17] W. Hofmeister, M. Wert, J. Smugeresky, J. A. Philiber, M. Griffith and M. Ensz, "Investigating Solidification with the Laser-Engineered Net Shaping (LENSTM) Process," TMS, July 1999. [Online]. Available: http://tms.org/pubs/journals/jom/9907/hofmeister/hofmeister-9907.html. [Accessed 15 December 2015].

[18] H. N. Doak, *Effect of Process Variables on Sub-Melt Thermal Behavior and Solid-State Phase Transformations in Beam-Based Additive Manufacturing of Ti-6Al-4V,* Wright State University, 2013.

[19] J. Beuth, J. Fox, J. Gockel, C. Montgomery, R. Yang, H. Qiao, E. Soylemez, P. Reeseewatt, A. Anvari, S. Narra and N. Klingbeil, "Process Mapping for Qualification Across Multiple Direct Metal Additive Manufacturing Processes," in *SFF Conference Proceedings*, Austin, 2013.

[20] A. Vasinonta, J. L. Beuth and M. Griffith, "Process Maps for Laser Deposition of Thin-Walled Structures," in *Solid Freeform Fabrication Proceedings*, Austin, 1999.

[21] A. Vasinonta, J. L. Beuth and M. Griffith, "Process Maps for Controlling Residual Stress and Melt Pool Size in Laser-Based SFF Processes," in *Solid Freeform Fabrication Proceedings*, Austin, 2000.

[22] N. W. Klingbeil, C. J. Brown, S. Bontha, P. A. Kobryn, and H. L. Fraser "Prediction of Microstructure in Laser Deposition of Titanium Alloys," in *Solid Freeform Fabrication Proceedings*, 2002.

[23] P. Kobryn and S. L. Semiatin, "Microstructure and texture evolution during solidification processing of Ti-6Al-4V," *Journal of Materials Processing Technology,* vol. 135, no. 2-3, pp. 330-339, April 2003.

[24] S. Bontha and N. Klingbeil, "Thermal Process Maps for Controlling Microstructure in Laser-Based Solid Freeform Fabrication," in *Solid Freeform Fabrication Proceedings*, Austin, 2003.

[25] N. Klingbeil, S. Bontha, C. Brown, D. Gaddam, P. Kobryn, H. Fraser and J. Sears, "Effects of Process Variables and Size Scale on Solification Microstructure in Laser-Based Solid Freeform Fabrication of Ti-6Al-4V," in *Solid Freeform Fabrication Proceedings*, Austin, 2004.

[26] S. Bontha, *The Effect of Process Variables on Microstructure in Laser-Deposited Materials,* Wright State University, 2006.

[27] S. Bontha, N. Klingbeil, P. Kobryn and H. Fraser, "Thermal Process Maps for Predicting Solidification Microstructure in Laser Fabrication of Thin Wall Structures," *Journal of Materials Processing Technology,* vol. 178, pp. 135-142, 2006.

[28] S. Bontha, N. W. Klingbeil, P. A. Kobryn and H. L. Fraser, "Effects of process variables and size-scale on solidification microstructure in beam-based fabrication of bulky 3D structures," *Materials Science and Engineering A,* pp. 311-318, 2009.

[29] J. Davis, N. Klingbeil and S. Bontha, "Effect of Free-Edges on Melt Pool Geometry and Solidification in Beam-Based Fabrication of Thin-Wall Structures," in *Solid Freeform Fabrication Proceedings*, Austin, 2009.

[30] J. Davis, N. Klingbeil and S. Bontha, "Effect of Free-Edges on Melt Pool Geometry and Solidification Microstructure in Beam-Based Fabrication of Bulky 3-D

Structures," in *Solid Freeform Fabrication Proceedings*, Austin, 2010.

[31] J. Davis, *Effect of Free-Edges on Melt Pool Geometry and Solidification Microstructure in Beam-Based Fabrication Methods,* Wright State University, 2010.

[32] J. Gockel and J. Beuth, "Understanding Ti-6Al-4V Microstructure Control in Additive Manufacturing via Process Maps," in *Solid Freeform Fabrication Proceedings*, Austin, 2013.

[33] J. Gockel, *Integrated Control of Solidification Microstructure and Melt Pool Dimensions in Additive Manufacturing of Ti-6Al-4V,* Carnegie Mellon University, 2014.

[34] C. Montgomery, J. Beuth, L. Sheridan and N. Klingbeil, "Process Mapping of Inconel 625 in Laser Powder Bed Additive Manufacturing," in *Solid Freeform Fabrication Proceedings*, Austin, 2015.

[35] S. Kuntz, *Feasibility of Attaining Fully Equiaxed Microstructure through Process Variable Control for Additive Manufacturing of Ti-6Al-4V,* Dayton, Ohio, 2016.

[36] L. Sheridan, *An Adapted Approach to Process Mapping Across Alloy Systems and Additive Manufacturing Processes,* Dayton, Ohio, 2016.

[37] Z. Francis, *The Effects of Laser and Electron Beam Spot Size in Additive Manufacturing Processes,* Pittsburgh, Pennsylvania, 2017.

[38] M. J. Donachie, Titanium: A Technical Guide, 2nd ed., Materials Park, Ohio: ASM International, 2000.

[39] D. R. Askeland, The Science and Engineering of Materials, 5th ed., Toronto: Thomson, 2006.

[40] W. F. Smith, Foundations of Materials Science and Engineering, 4th ed., Boston: McGraw-Hill, 2006.

[41] C. Leyens and M. Peters, Eds., Titanium and Titanium Alloys: Fundamentals and Applications, Wiley, 2003.

[42] C. R. Brooks, Heat Treatment, Structure, and Properties of Nonferrous Alloys, Metals Park, Ohio: American Society for Metals, 1982.

[43] D. M. Stefanescu and R. Ruxanda, "Solidification Structures of Titanium Alloys," in *ASM Handbook, Volume 9: Metallography and Microstructures*, G. Vander Voort, Ed., Materials Park, Ohio: ASM International, 2004, pp. 116-126.

[44] P. C. Collins, P. Welk, T. Searles, J. Tiley, J. Russ and H. Fraser, "Development of methods for the quantification of microstructural features in α + β-processed α/β titanium alloys," *Materials Science and Engineering: A,* vol. 508, no. 1-2, pp. 174-182, May 2009.

[45] J. D. Destefani, "Introduction to Titanium and Titanium Alloys," in *ASM Handbook, Volume 2: Properties and Selection: Nonferrous Alloys and Special-Purpose Materials*, Materials Park, Ohio: ASM International, 1990, pp. 586-591.

[46] J. Tiley, T. Searles, E. Lee, S. Kar, R. Banerjee, J. Russ and H. Fraser, "Quantification of Microstructural Features in α/β Titanium Alloys," *Materials Science & Engineering A,* no. 372, pp. 191-198, 2004.

[47] T. Searles, J. Tiley, A. Tanner, R. Williams, B. Rollins, E. Lee, S. Kar, R. Banerjee and H. Fraser, "Rapid Characterization of Titanium Microstructural Features for Specific Modelling of Mechanical Properties," *Measurement Science and Technology,* no. 16, pp. 60-69, 2004.

[48] J. M. Sosa, D. E. Huber, B. Welk and H. L. Fraser, "Development and Application of MIPAR: a novel software package for two- and three-dimensional microstructural characterization," *Integrating Materials and Manufacturing Innovation,* 2014.

[49] G. T. Loughnane, S. L. Kuntz, N. Klingbeil, J. M. Sosa, J. Irwin, A. R. Nassar and E. W. Reutzel, "Application of a microstructural characterization uncertainty quantification framework to Widmanstätten α-laths in additive manufactured Ti-6Al-4V," in *Solid Freeform Fabrication Proceedings*, Austin, 2015.

[50] A. Leicht and E.O. Wennberg, *Analyzing the Mechanical Behavior of Additive Manufactured Ti-6Al-4V Using Digital Image Correlation,* Gothenburg, 2015.

[51] J. M. (. Holt, "Uniaxial Tension Testing," in *ASM Handbook, Volume 8: Mechanical Testing and Evaluation*, H. a. M. D. Kuhn, Ed., Materials Park, Ohio: ASM International, 2000, pp. 124-142.

[52] L. H. Van Vlack, Elements of Materials Science: An Introductory Text for Engineering Students, 2nd ed., Reading, Massachusetts: Addison-Wesley

Publishing Company, Inc., 1964.

[53] R. W. Hertzberg, Deformation and Fracture Mechanics of Engineering Materials, 4th ed., Danvers, Massachusetts: John Wiley & Sons, Inc., 1996.

[54] J. Sieniawski, W. Ziaja, K. Kubiak and M. Motyka, "Microstructure and Mechanical Properties of High Strength Two-Phase Titanium Alloys," in *Titanium Alloys*, IntechOpen, 2013.

[55] M. Simonelli, C. J. Tuck, and Y. Tse, "Effect of the building orientation on the mechanical properties and fracture modes of SLM Ti-6Al-4V," *Materials Science & Engineering A,* vol. 616, pp. 1-11, 2014.

[56] P. Kobryn and S. Semiatin, "Mechanical Properties of laser-deposited Ti-6Al-4V," in *Proceedings of the 12th Solid Freeform Fabrication Symposium*, Austin, 2001.

[57] B. E. Carroll, T. A. Palmer and A. M. Beese, "Anisotropic tensile behavior of Ti-6Al-4V components fabricated with directed energy deposition additive manufacturing," *Acta Materialia,* vol. 87, pp. 309-320, 2015.

[58] T. Osman, and J. Rigney, "Introduction to the Mechanical Behavior of Metals," in *ASM Handbook, Volume 8: Mechanical Testing and Evaluation*, H. a. M. D. Kuhn, Ed., Materials Park, Ohio: ASM International, 2000, pp. 3-12.

[59] Z. Zhang, S. Qu and A. Feng, and J. Shen, "Achieving grain refinement and enhanced mechanical properties in Ti-6Al-4V alloy produced by multidirectional isothermal forging," *Materials Science and Engineering A,* vol. 692, pp. 127-138, March 2017.

[60] B. J. Hayes, B. W. Martin, B. Welk, S. J. Kuhr, T. K. Ales, D. A. Brice, I. Ghamarian, A. H. Baker, C. V. Haden, D. G. Harlow, H. L. Fraser and P. C. Collins, "Predicting tensile properties of Ti-6Al-4V produced via directed energy deposition," *Acta Materialia,* vol. 133, pp. 120-133, July 2017.

[61] E. P. DeGarmo, Materials and Processes in Manufacturing, 4th ed., New York: MacMillan Publishing Co., Inc., 1974.

[62] R. Hibbeler, Statics and Mechanics of Materials, 3rd ed., Boston: Prentice Hall, 2011.

[63] G. Revankar and D. &. Company, "Introduction to Hardness Testing," in *ASM Handbook, Volume 8: Mechanical Testing and Evaluation*, Materials Park, Ohio: ASM International, 2000, pp. 197-202.

[64] Struers, Inc., "Hardness Testing," 2018. [Online]. Available: https://www.struers.com/en/Knowledge/Hardness-testing#application-specialists. [Accessed 20 October 2018].

[65] A. Fee, "Selection and Industrial Applications of Hardness Tests," in *ASM Handbook, Volume 8: Mechanical Testing and Evaluation*, Materials Park, Ohio: ASM International, 2000, pp. 260-277.

[66] "Rockwell Hardness Measurement of Metallic Materials," U.S. Government Printing Office, Washington DC, 2001.

[67] G. F. Vander Voort, "Microindentation Hardness Testing," in *ASM Handbook, Volume 8: Mechanical Testing and Evaluation*, Materials Park, Ohio: ASM International, 2000, pp. 221-231.

[68] E. L. Tobolski and A. Fee, "Macroindentation Hardness Testing," in *ASM Handbook, Volume 8: Mechanical Testing and Evaluation*, Materials Park, Ohio: ASM International, 2000, pp. 203-220.

[69] ASTM International, "Standard Test Method for Microindentation Hardness of Materials," 2017. [Online]. Available: https://www.astm.org/Standards/E384.htm. [Accessed 20 October 2018].

[70] A. C. Fischer-Cripps, Nanoindentation, New York: Springer, 2011.

[71] A. Thompson and B. Taylor, "NIST Guide to the SI, Chapter 5: Units Outside the SI," U.S. Department of Commerce, 2 July 2009. [Online]. Available: https://www.nist.gov/pml/special-publication-811/nist-guide-si-chapter-5-units-outside-si. [Accessed 21 November 2018].

[72] L. Murr, E. Esquivel, S. Quinones, S. Gaytan, M. Lopez, E. Martinez, F. Medina, D. Hernandez, E. Martinez, J. Martinez, S. Stafford, D. Brown, T. Hoppe, W. Meyers, U. Lindhe and R. Wicker, "Microstructures and mechanical properties of electron beam-rapid manufactured Ti-6Al-4V biomedical prototypes compared to wrought Ti-6Al-4V," *Materials Characterization,* no. 60, pp. 96-105, 2009.

[73] P. Kobryn and S. Semiatin, "Laser Forming of Ti-6Al-4V: Research Overview," in *Proceedings of the 12th Solid Freeform Fabrication Symposium*, Austin, 2001.

[74] R. P. Mudge and N. R. Wald, "Laser Engineered Net Shaping Advances Additive Manufacturing and Repair," *Welding Journal,* pp. 44-48, 2007.

[75] M. Das, V. K. Balla, T. S. Kumar and I. Manna, "Fabrication of Biomedical Implants using Laser Engineered Net Shaping (LENS TM)," *Transactions of the Indian Ceramic Society,* vol. 72, no. 3, pp. 169-174, 08 April 2013.

[76] Y. W. Zhai and D. A. Lados, "Novel Forming of Ti-6Al-4V by Laser Engineered Net Shaping," *Materials Science Forum,* vol. 765, pp. 393-397, 31 July 2013.

[77] A. Sterling, N. Shamsaei, B. Torries and S. M. Thompson, "Fatigue Behavior of Additively Manufactured Ti-6Al-4V," in *Procedia Engineering*, 2015.

[78] W. Harun, N. Manam, M. Kamariah, S. Sharif, A. Zulkifly, I. Ahmad and H. Miura, "A review of powdered additive manufacturing techniques for Ti-6Al-4V biomedical applications," *Powder Technology,* no. 331, pp. 74-97, 2018.

[79] Optomec, "LENS MR-7 Systems," July 2017. [Online]. Available: https://www.optomec.com/wp-content/uploads/2017/07/LENS_MR-7_WEB0719.pdf. [Accessed 20 October 2018].

[80] J. E. Fuller, "Electrical Discharge Machining," in *ASM Handbook, Volume 16: Machining*, Materials Park, Ohio: ASM International, 1989, pp. 557-564.

[81] Struers Inc., "How to Hot Mount," 2018. [Online]. Available: https://www.struers.com/Knowledge/Mounting/Hot-mounting. [Accessed 20 October 2018].

[82] Kemet International Ltd, "Metallographic Polishing and Grinding," 2018. [Online]. Available: https://www.kemet.co.uk/blog/metallography/metallographic-polishing-and-grinding. [Accessed 20 October 2018].

[83] Buehler, "EcoMet 250/AutoMet 250, Membrane Keypad," 2016. [Online]. Available: https://shop.buehler.com/ecomet250automet250-wmembrne. [Accessed 20 October 2018].

[84] G. F. Vander Voort, Metallography, Principles and Practice, New York: McGraw-Hill, Inc., 1984, pp. 410-414; 423-431.

[85] R. Lewis, *Conversation about metallographic procedures for titanium alloys,* Dayton, Ohio, 2014.

[86] Lapmaseter Wolters, *Lapmaster Wolters Metallographic Equipment & Supplies Catalog,* Mount Prospect, Illinois, 2016, p. 66.

[87] G. Vander Voort, "Metallographic Preparation of Titanium and Its Alloys," 9 July 2014. [Online]. Available: https://vacaero.com/information-resources/metallography-with-george-vander-voort/1397-metallographic-preparation-of-titanium-and-its-alloys.html. [Accessed 7 June 2018].

[88] Buehler, "TexMet C, PSA, 2.875 in," 2016. [Online]. Available: https://shop.buehler.com/texmet-c-2-78inch73mm-20pk. [Accessed 13 November 2018].

[89] "VibroMet™ 2 Vibratory Polisher," Buehler, 2018. [Online]. Available: https://www.buehler.com/vibromet-2-vibratory-polisher.php. [Accessed 13 June 2018].

[90] Struers, Inc., *Metallographic Preparation of Titanium.*

[91] Buehler, "MicroCloth, PSA, 8 in," 2016. [Online]. Available: https://shop.buehler.com/microcloth-for-8-in-wheel-psa. [Accessed 18 November 2018].

[92] G. Vander Voort, Ed., "Contrast Enhancement and Etching," in *ASM Handbook Volume 9: Metallography and Microstructures*, Materials Park, Ohio: ASM International, 2004, pp. 294-312.

[93] G. F. Vander Voort, Metallography, Principles and Practice, Materials Park, Ohio: ASM International, 1999.

[94] Z. Francis, *Email chain about using ImageJ to characterize single layer pads,* 2015.

[95] T. J. Collins, "ImageJ for Microscopy," *BioTechniques,* vol. 43, 16 May 2018.

[96] W. Navidi, Statistics for Engineers and Scientists, 3rd ed., New York: McGraw-Hill, 2011, pp. 322-368.

[97] D. Diez, "Metallography - an Introduction. How to Reveal Microstructural Features of Metals and Alloys," 18 October 2013. [Online]. Available: https://www.leica-microsystems.com/science-lab/metallography-an-introduction/. [Accessed 17 October 2018].

[98] L. Sheridan, *Conversation about SEM imaging of single layer pad samples,* Dayton, Ohio, 2015.

[99] "Fovea Pro Tutorial," 2011. [Online]. Available: http://www.reindeergraphics.com/foveaprotutorial.html. [Accessed 8 July 2015].

[100] J. C. Russ, The Image Processing and Analysis Cookbook, Asheville, North Carolina: Reindeer Graphics, Inc., 2001.

[101] D. A. Kriczky, J. Irwin, E. W. Reutzel, P. Michaleris, A. R. Nassar and J. Craig, "3D spatial reconstruction of thermal characteristics in directed energy deposition through optical thermal imaging," *Journal of Materials Processing Technology,* pp. 172-186, 2015.

[102] Allied High Tech Products, Inc., "TechCut 5™ Precision High Speed Saw," 2018. [Online]. Available: http://www.alliedhightech.com/Equipment/techcut-5-precision-sectioning-machine. [Accessed 24 October 2018].

[103] Allied High Tech Products, Inc., "TechCut 4™ Precision Low Speed Saw," 2018. [Online]. Available: http://www.alliedhightech.com/Equipment/techcut-4-low-speed-saw. [Accessed 22 October 2018].

[104] G. T. Loughnane, *A Framework for Uncertainty Quantification in Microstructural Characterization with Application to Additive Manufacturing of Ti-6Al-4V,* Dayton, Ohio, 2015.

[105] A. Bagheri, N. Shamsaei and S. Thompson, "Microstructure and Mechanical Properties of Ti-6Al-4V Parts Fabricated by Laser Engineered Net Shaping Fatigue and Cyclic Deformation of Superelastic and Shape Memory Alloys," in *ASME 2015 International Mechanical Engineering Congress and Exposition*, Houston, 2015.

[106] E. Soylemez, J. L. Beuth and K. Taminger, "Controlling Melt Pool Dimensions Over a Wide Range of Material Deposition Rates in Electron Beam Additive Manufacturing," in *Solid Freeform Fabrication Proceedings*, Austin, TX, 2010.

[107] C. Kusuma, *The Effect of Laser Power and Scan Speed on Melt Pool Characteristics of Pure Titanium and Ti-6Al-4V alloy for Selective Laser Melting,* Dayton, Ohio, 2014.

[108] R. S. Figliola and D. E. Beasley, Theory and Design for Mechanical Measurements, 5th ed., John Wiley & Sons, Inc., 2011.

[109] Microsoft, "CONFIDENCE function," 2018. [Online]. Available: https://support.office.com/en-us/article/confidence-function-75ccc007-f77c-4343-

bc14-673642091ad6. [Accessed 14 November 2018].

[110] S. C. Kuchi, *Effect of Finite Geometry on Solidification Microstructure in Beam-Based Fabrication of Thin Wall Structures,* Dayton, Ohio, 2009.

[111] A. Saboori, D. Gallo, S. Biamino, F. Paolo and a. L. Mariangela, "An Overview of Additive Manufacturing of Titanium Components by Directed Energy Deposition: Microstructure and Mechanical Properties," *Applied Sciences,* 2017.

[112] M. Robinaugh, *Conversation about how to use IgorPro,* Dayton, Ohio, 2016.

[113] P. Sathiyamoorthi, J. Basu, S. Kashyap, P. K G and R. S. Kottada, "Thermal stability and grain boundary strengthening in ultrafine-grained CoCrFeNi high entropy alloy composite," *Materials & Design,* no. 134, pp. 426-433, 2017.

[114] N. Levkulich, *Conversation about Vickers microhardness testing for light and dark bands,* Dayton, Ohio, 2016.

[115] R. Srinivasan, *Conversation about Vickers Microhardness Measurements,* Dayton, Ohio, 2018.

[116] G. Barbato and S. Desogus, "Problems in the measurement of Vickers and Brinell indentations," *Measurement,* vol. 4, no. 4, pp. 137-147, 1986.

[117] G. Barbato and F. Petik, "Comparison between the HRC, HRB, and HV30 hardness scales maintained at the Istituto di Metrologia 'G. Colonnetti' (IMGC), Turin, and those of the Országos Mérésugyi Hivatal (OMH), Budapest.," *OIML Bulletin,* no. 82, 1981.

[118] J. Tiley, *Discussion about banding effecting in LENS Ti-6Al-4V structural components,* Dayton, Ohio, 2015.

[119] P. Zinin, *Microanalysis in Electron Microscopy,* Honolulu, Hawaii.

[120] S. T. Oh, K. D. Woo, J. H. Kim and S. M. Kwak, "The Effect of Al and V on Microstructure and Transformation of β Phase during Solution Treatments of Cast Ti-6Al-4V Alloy," *Korean J. Met Mater.,* vol. 55, pp. 150-155, 2016.

# Appendix A Additional Micrographs for Thin Walls

Figure A.1: Thin wall sample produced using 450 W beam power, 25 ipm velocity and 3 gpm powder feed rate

Figure A.2: Thin wall sample produced using 350 W beam power, 7.5 ipm velocity and 0.9 gpm powder feed rate

Figure A.3: Thin wall sample produced using 400 W beam power, 16.4 ipm velocity and a 3 gpm powder feed rate

Figure A.4: Thin wall sample produced with 450 W beam power, 25 ipm velocity and 3 gpm powder feed rate

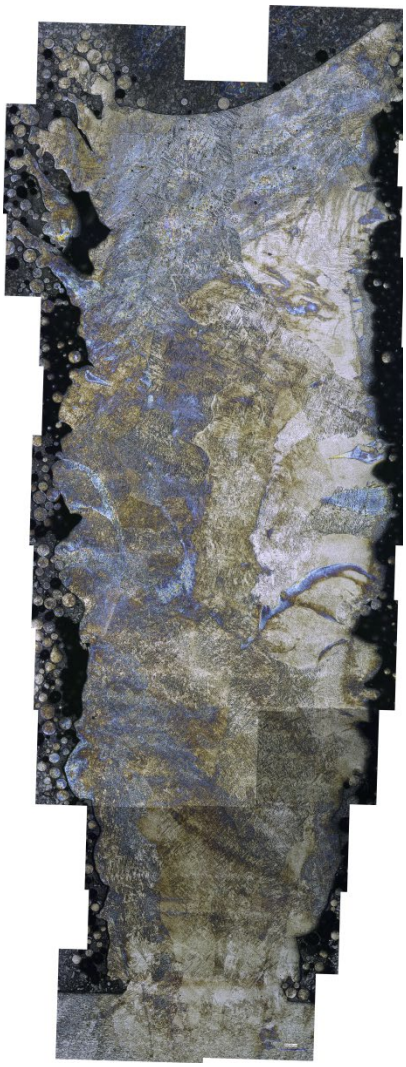

Figure A.5: Thin wall sample produced with 350 W beam power, 7.5 ipm velocity and 3 gpm powder feed rate

Figure A.6: Thin wall sample produced with 350 W beam power, 7.5 ipm velocity and 0.9 gpm powder feed rate

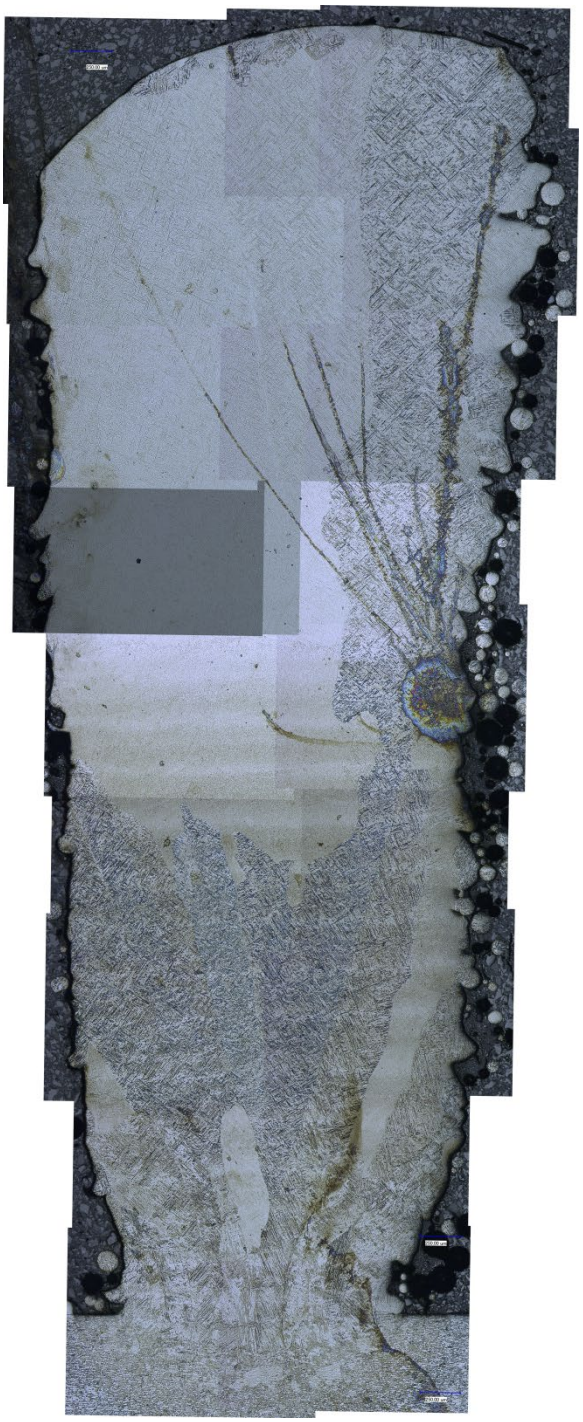

Figure A.7: Thin wall sample produced with a 400 W beam power, 16.4 ipm velocity and a 2 gpm powder feed rate

Figure A.8: Thin wall sample produced with a 450 W beam power, 25 ipm velocity and 3 gpm powder feed rate

# Appendix B Additional Micrographs for Multilayer Pad Samples

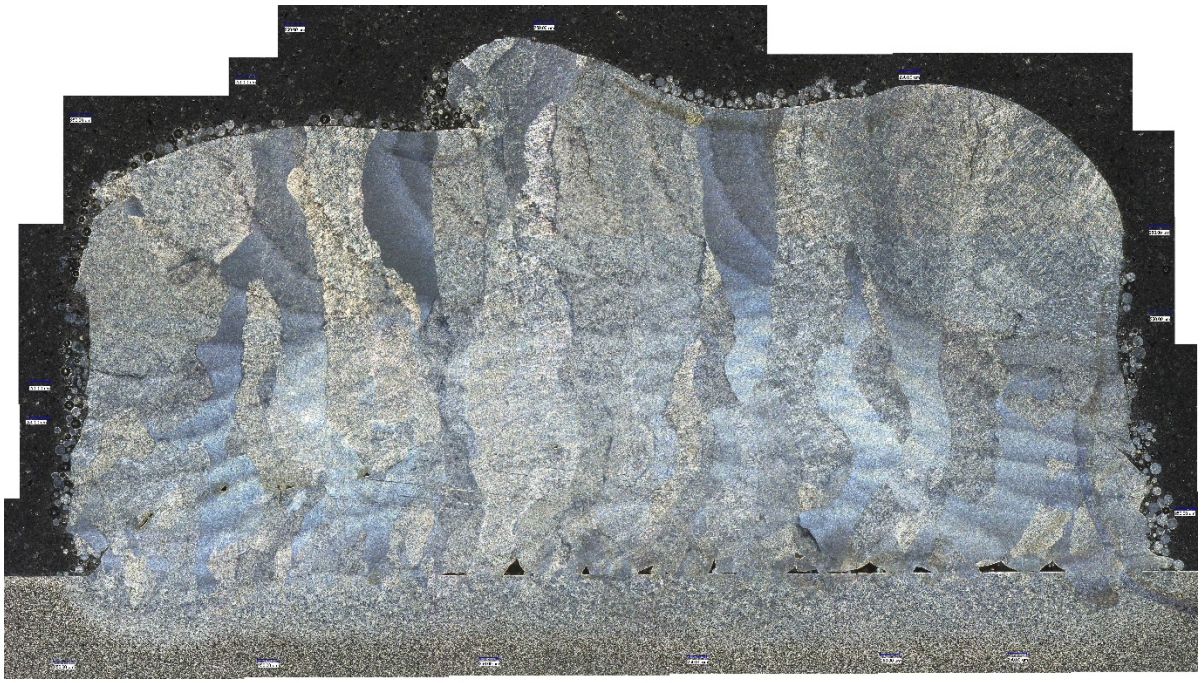

Figure B.1: Sample 5-Feb-05 imaged at 100x magnification

Figure B.1 shows a multilayer pad imaged at 100x magnification under polarized light. The sample was produced with a beam power of 350 W, a velocity of 7.5 ipm and a powder feed rate of 0.9 gpm. It was determined that 100x magnification was not sufficiently high resolution for tracing beta grains. Figure B.2 shows the same multilayer pad imaged at 200x magnification under polarized light. The difference in coloration is due to 2 factors. First, it is darker because when a microscope zooms in further, less light is able to make it into the lens. Second, there is possibly a titanium oxide layer on the surface of the sample because the 200x samples were taken after the 100x samples.

Figure B.2: Sample 5-Feb-05 at 200x magnification

Figure B.3 shows sample 4-May-05 at 100x magnification under polarized light. This sample was also produced with a beam power of 350 W, a velocity of 7.5 ipm, and a powder feed rate of 0.9 gpm. Figure B.4 shows the same sample at 200x magnification under polarized light.

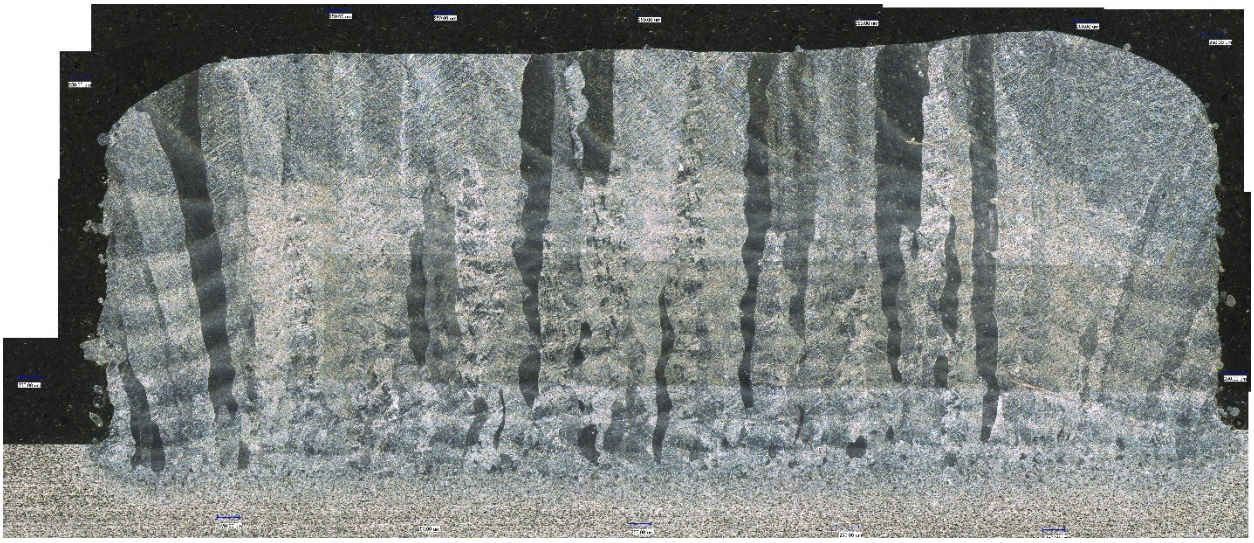

Figure B.3: Sample 4-May-05 at 100x magnification

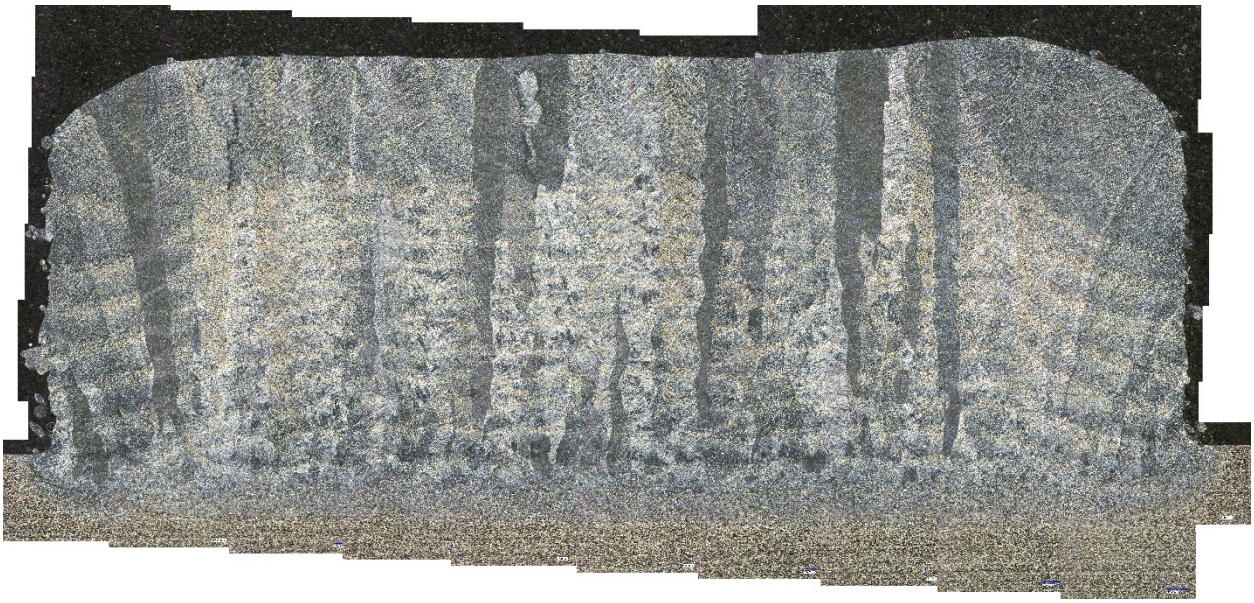

Figure B.4: Sample 4-May-05 at 200x magnification

Figure B.5 shows sample 5-Feb-10 imaged at 100x magnification under polarized light. The sample was produced with a beam power of 400 W, a velocity of 16.4 ipm and a powder feed rate of 2 gpm. Figure B.6 shows the same sample imaged at 200x magnification under polarized light.

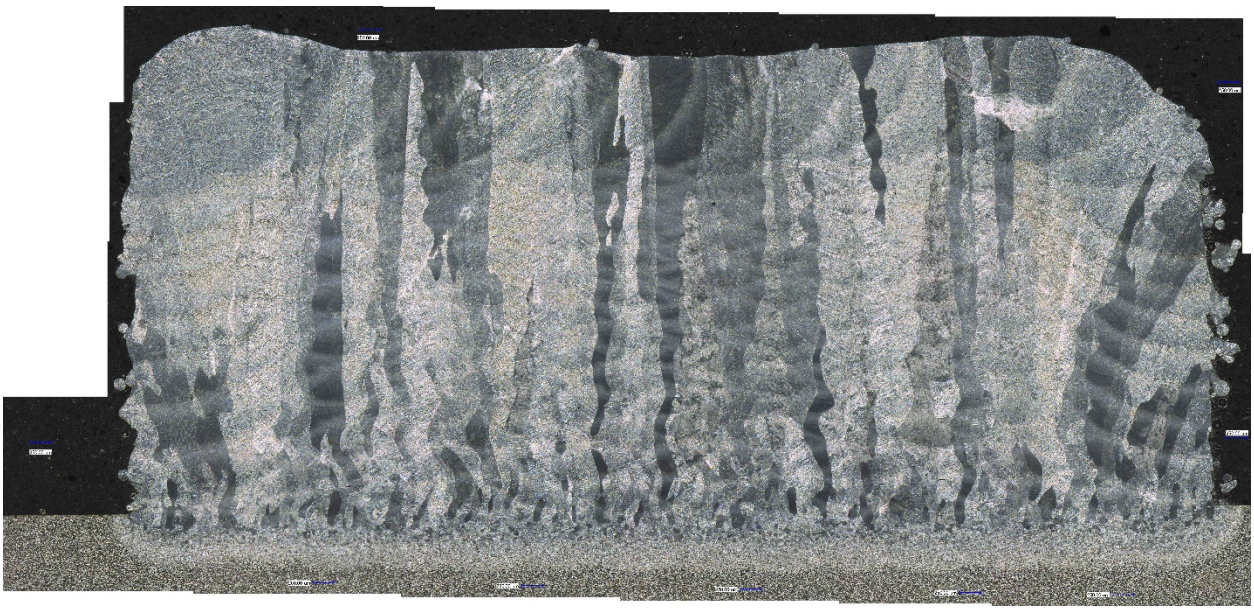

Figure B.5: Sample 5-Feb-10 at 100x magnification

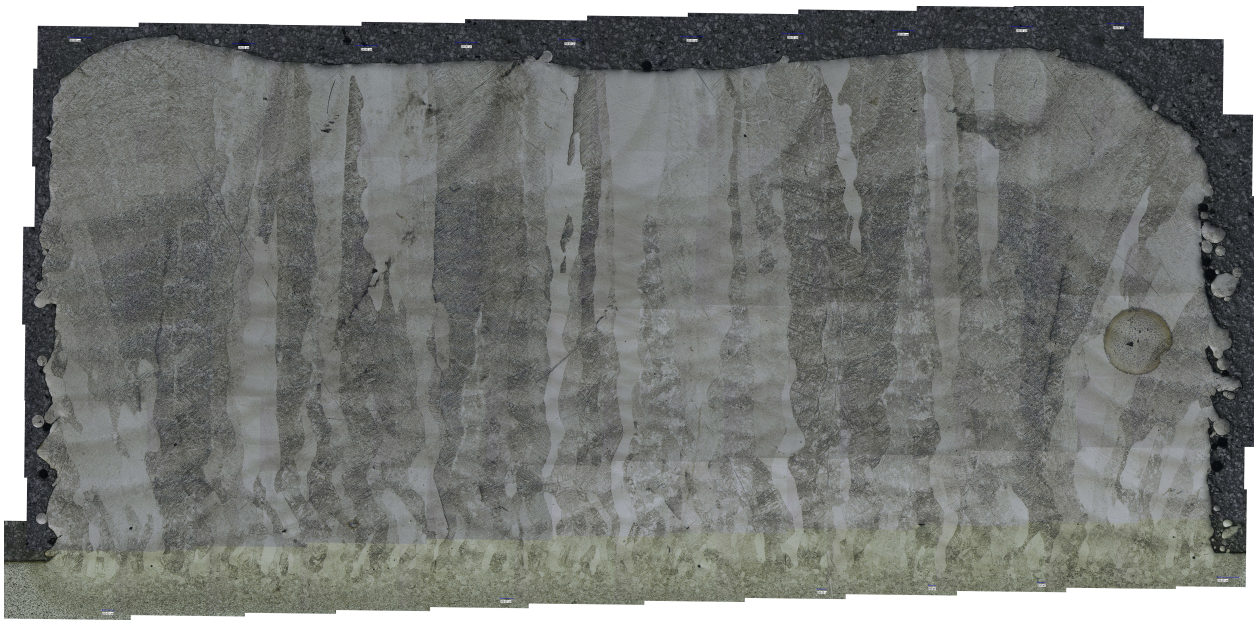

Figure B.6: Sample 5-Feb-10 at 200x magnification

Figure B.7 shows sample 4-May-10 at 100x magnification. This sample was also produced with a beam power of 400 W, a velocity of 16.4 ipm and a powder feed rate of 2 gpm. Figure B.8 shows the same sample at 200x magnification.

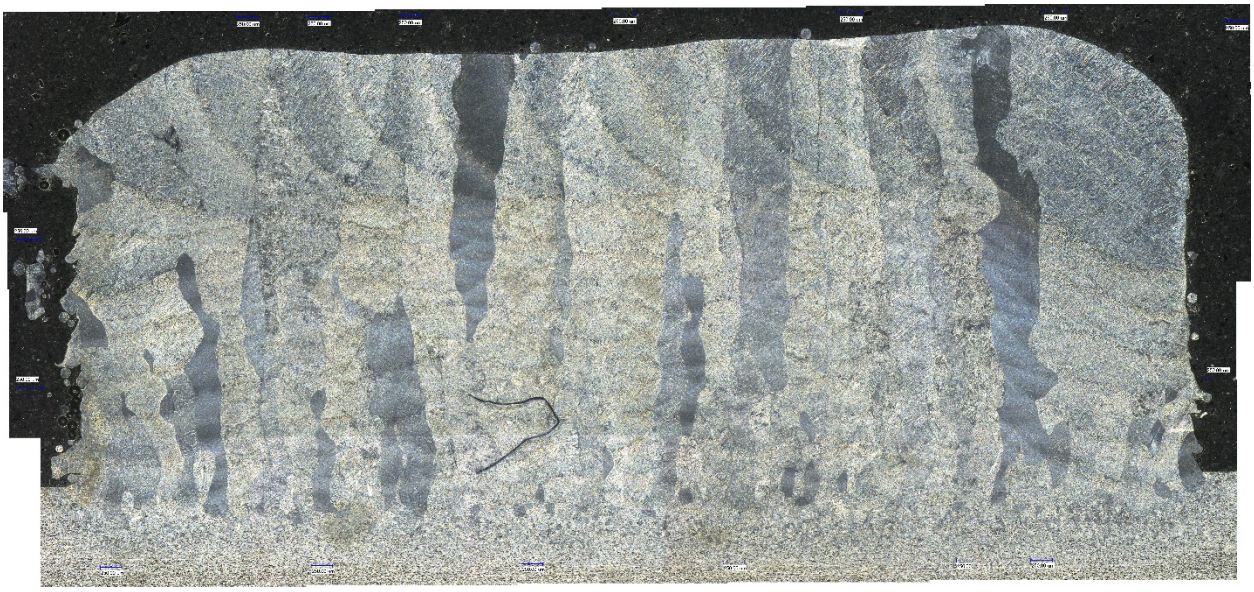

Figure B.7: Sample 4-May-10 at 100x magnification

Figure B.8: Sample 4-May-10 at 200x magnification

Figure B.9 shows sample 5-Feb-15 at 100x magnification. The sample was produced with a beam power of 450 W, a velocity of 25 ipm and a powder feed rate of 3 gpm. Figure B.10 shows the same sample at 200x magnification.

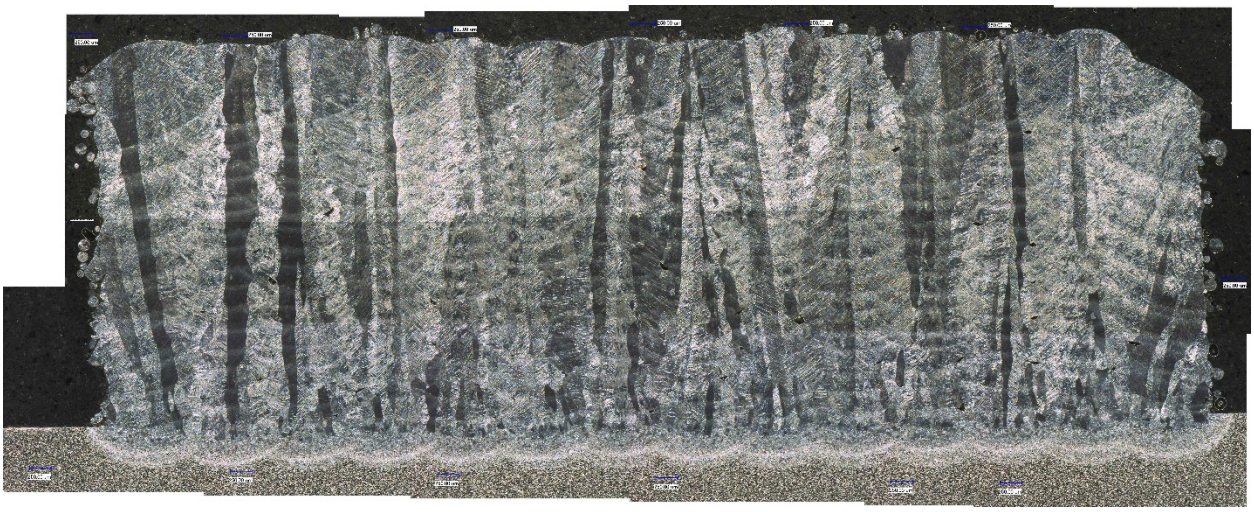

Figure B.9: Sample 5-Feb-15 at 100x magnification

Figure B.10: Sample 5-Feb-15 at 200x magnification

Figure B.11 shows sample 4-May-15 at 100x magnification. The sample was also produced with a beam power of 450 W, a velocity of 25 ipm and a powder feed rate of 3 gpm. Figure B.12 shows the same sample at 200x magnification.

Figure B.11: Sample 4-May-15 at 100x magnification

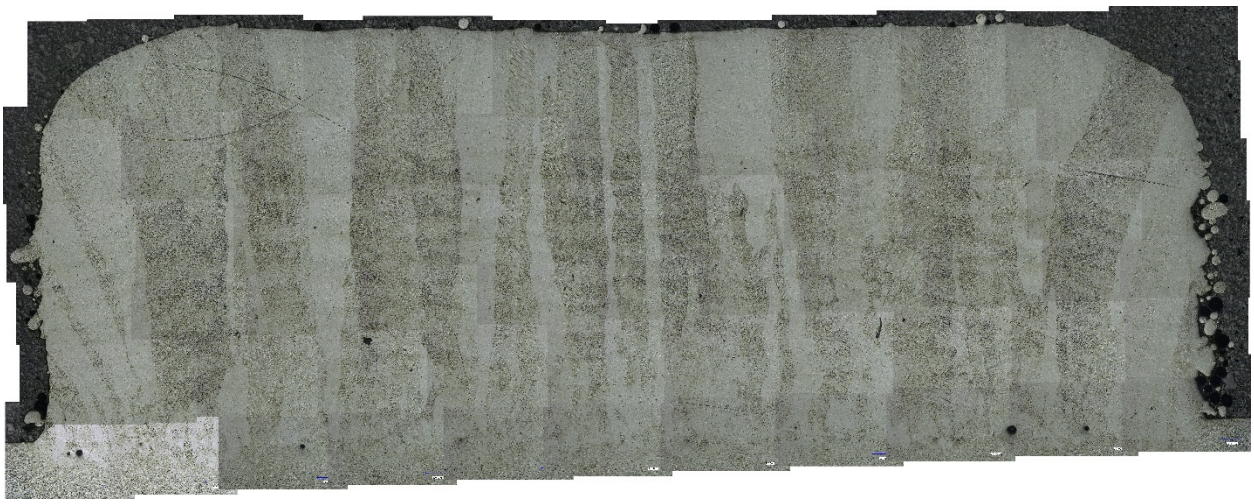

Figure B.12: Sample 4-May-15 at 200x magnification

# Appendix C Additional Micrographs for Single Layer Pads

This appendix contains additional SEM micrographs that were used for the α-lath analysis of the single layer pads. Figure C.1 shows an SEM image taken with backscatter detection at 2000x magnification. The sample, 3-Feb-5, was produced with a beam power of 450 W, a velocity of 7.5 ipm and a scaled powder feed rate. The α-lath width for the sample was determined to be 0.600 µm.

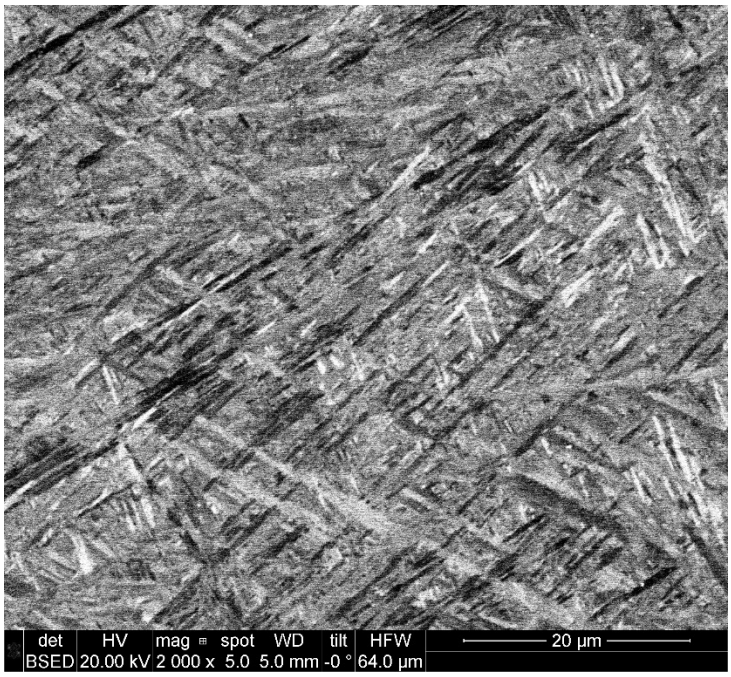


Figure C.1: Sample 3-Feb-5 at 2000x magnification

Figure C.2 shows sample 3-Feb-15 at 2000x magnification. The sample was produced with a beam power of 250 W, a velocity of 25 ipm and a scaled powder feed rate. The α-lath width for the sample was determined to be 0.623 µm.

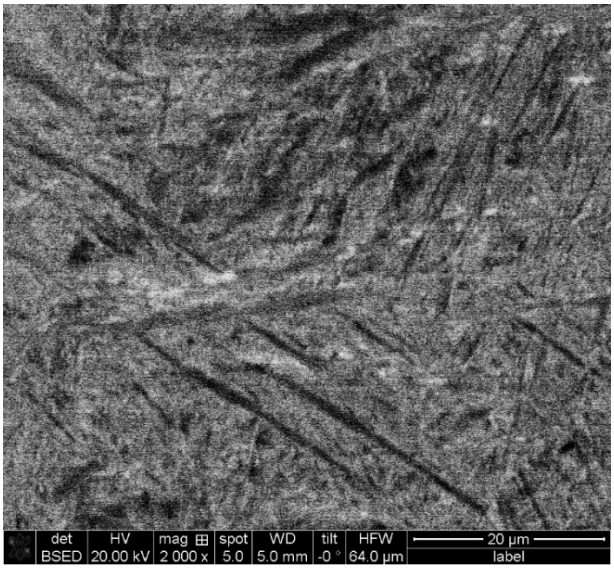


Figure C.2: Sample 3-Feb-15 at 2000x magnification

Figure C.3 shows sample 3-May-5 at 2000x magnification. The sample was produced with a beam power of 350 W, a velocity of 7.5 ipm and it was a laser glaze. In other words, there was no powder added. The α-lath width for the sample was determined to be 0.621 µm. This is the sample that was used to make the demonstration of the image processing steps in Chapter 2 of this thesis.

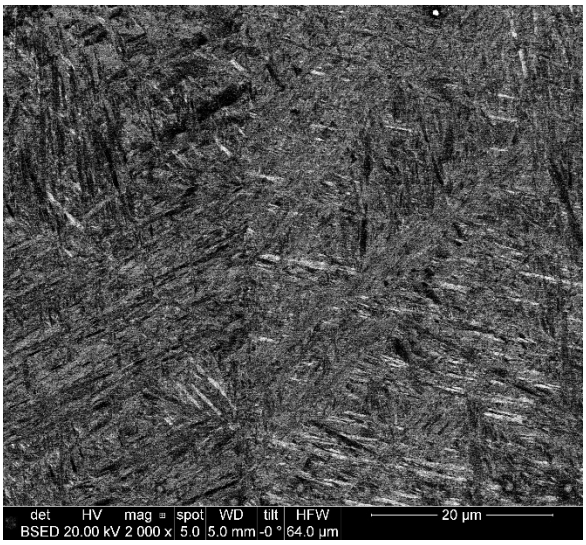


Figure C.3: Sample 3-May-5 at 2000x magnification

Figure C.4 shows sample 4-Feb-15 at 2000x magnification. The sample was produced with a beam power of 250 W, a velocity of 25 ipm and a scaled powder feed rate. The α-lath width for the sample was determined to be 0.614 µm.

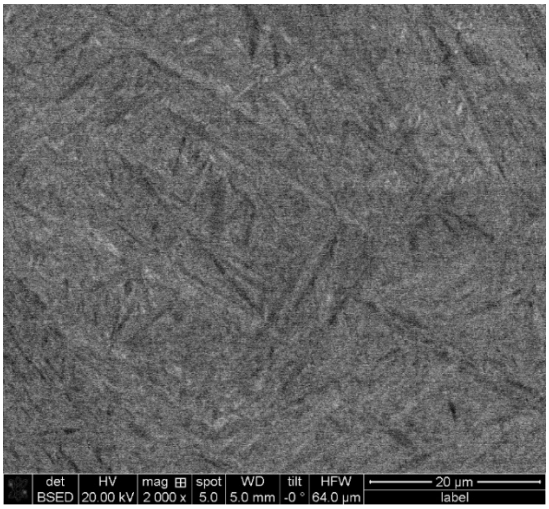


**Figure C.4: Sample 4-Feb-15 at 2000x magnification**

Figure C.5 shows sample 5-Feb-5 at 2000x magnification. The sample was produced with a beam power of 350 W, a velocity of 7.5 ipm and a powder feed rate of 3 gpm. The α-lath width for the sample was determined to be 0.609 µm.

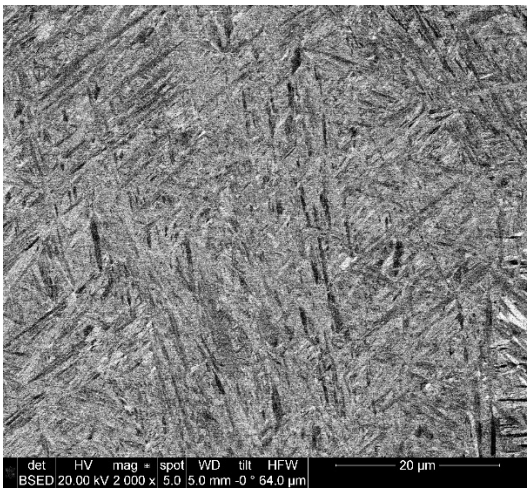


**Figure C.5: Sample 5-Feb-5 at 2000x magnification**